Modeling of Mobile Communication Antennas by Finite-Difference Time-Domain Method and its Applications

(移動体通信用アンテナの FDTD 法による
モデリングとその応用に関する研究)

March 2004

Naobumi Michishita

preface

A highly accurate analysis is required to realize the coupling of −30 dB between each element for vertical and horizontal polarization. The repeater system also requires a coupling of −100 dB, and it is difficult to obtain its value through the measurement. The design of a highly functional antenna requires a modeling of the equivalent circuit for passive and active elements.

The objective of this study is to propose a modeling of mobile communication antennas by the FDTD method and its applications. This dissertation discusses the two main parts: a modeling of an antenna and its immediate environment, and a modeling of an equivalent circuit. In Chapter 2, a modeling of the hybrid polarization diversity antenna with a side reflector is presented. A basic technique for FDTD analysis is discussed to examine the effect of the immediate environment of the antennas. The horizontal beam widths of a dipole antenna and a holed patch antenna are optimized by modeling the side reflector, and the mutual coupling of the hybrid antenna is analyzed. In Chapter 3, a mutual coupling between a transmitting and receiving antenna with a choke is presented. The increase in the front-to-back or side ratio causes the suppression of mutual coupling, and attains a mutual coupling of −100 dB. In Chapter 4, the modeling of a balun to feed a dual frequency antenna is presented. The parameters of a series-connected open stub and a parallel-connected short are examined in detail, and the stub length can help realize the multi-frequency operation. In Chapter 5, the modeling of a GaAsFET for an active integrated antenna is presented. The characteristics of the integrated antenna can be accurately computed by combinations of the FDTD and circuit calculation methods.

Finally, Chapter 6 summarizes and concludes this dissertation.

Acknowledgement

I wish to express my gratitude to my sincerest acknowledgment to my supervisor Professor Hiroyuki Arai for his continuous guidance throughout this work.

I am grateful to Professor Yasuo Kokubun, Professor Ryuji Kohno, Associate Professor Toshihiko Baba, and Associate Professor Koichi Ichige with Yokohama National University for their useful discussions and the critical reading of manuscript. I am most obliged to Dr. Yoshio Ebine of NTT DoCoMo, Inc. for the valuable comments, direction, encouragement and hospitality.

I also express my appreciation to Dr. Koichi Tsunekawa of NTT Corporation, Mr. Masayuki Nakano of KDDI Corporation, and Dr. Masahiro Karikomi of Nihon Dengyo Kosaku Co., Ltd. for their valuable suggestions and encouragement. My deep gratitude is due to Dr. Kazuhiro Fujimori of Okayama University for the valuable comments, advice and encouragement. I am grateful to Dr. Nobuhiro Kuga of Tokyo Polytechnic University, Dr. Kohei Mori of Sony Corporation, Dr. Huiling Jiang of NTT DoCoMo, Inc., and Dr. Yuko Rikuta of Communications Research Laboratory for their useful discussion and encouragement. Thanks are also due to the members of Professor Arai's group, Yokohama National University.

Finally I express the respect to my parents for their mental support.

Contents

Chapter 1

Introduction

1.1 Background

Radio waves contribute to the realization of a life of high quality and comfort. The realization of a ubiquitous network becomes more likely with the construction of a wireless broadband environment. Japan's cellular phone subscriber base touched 80.1 million in January 2004, and a third generation mobile communication system (IMT-2000), which provides high-speed data transmission and image distribution services, has been launched. In recent years, adaptive array antennas, MIMOs, and UWBs have become popular as technologies for the efficient use of radio waves. A product that is in conformity with IEEE 802.11 g and has a maximum transmission speed of 54 Mbps has been released in a wireless LAN. The advancement, development, and introduction of RFID, ITS, and a quasi-zenith satellite communication system are promoted in this ubiquitous network. Further, the software-defined radio technology is an effective response to these mixed systems. Antenna technology assumes an effective role, and the design of antenna systems requires the high-accuracy analysis.

1.2 Survey of Earlier Studies

1.2.1 Antenna Analysis Techniques

The Finite-Difference Time-Domain (FDTD) method was introduced by Yee in 1966 [1] for solving Maxwell's curl equations directly in the time domain on a space grid. FDTD and related methods have been used as analytic techniques in electromagnetics [2]–[5]. The examples of both contemporary and emerging applications of FDTD modeling span many different fields. Examples of such applications include small electric antennas, radars, circuit-board modules for high-speed computers, microwave circuits, the specific absorption rate (SAR) of cellular phones, optical microdisk resonators, and photonic bandgap microcavity lasers.

The most important requirements of FDTD analysis are accuracy and the calculation time. The FDTD method is based on an explicit finite-difference algorithm, and the Courant-Friedrich-Levy (CFL) condition must be satisfied when this method is used. Therefore, the maximum time-step size is limited by a minimum cell size in a computational domain, and a small time-step size creates a significant increase in the calculation time. To eliminate this limitation of the CFL condition, a new algorithm, based on the alternating-direction implicit (ADI) method, was proposed [6]–[10]. However, there seem to be few examples that are applicable to the practical problems in the present condition, which is the stage at which various mathematical characteristics are being examined [11][12]. However, this paper does not concern itself with the ADI-FDTD; rather, it investigates the accuracy and calculation time of the conventional FDTD.

The computational cost of the FDTD analysis scales directly with the number of cells. If an analytic object has a small structure, an uniform cell size must be chosen in accordance with the smallest structure. The number of the division in the substrate increases because a cell size is also decided in accordance with the minimum wavelength of a dielectric in the case of a planar antenna on a dielectric substrate. Three ways, which changes a size and a form of cells, are proposed to lower a computational cost and to analyze with a high degree of accuracy. The non-uniform mesh method is applied a fine grid in important structural features to

deal appropriately with rapid changes of electromagnetics [13]–[15]. The subgridding method is redivided the part of the coarse main grid into the fine local grid, and is effective in that a finer grid is only employed where needed [16]–[18]. The subcell method is used when a conductor crosses a cell obliquely [19][20]. This approach involves an application of Maxwell's equations in integral rather than differential form.

The convergent time of a feed current is long in the case of a miniature antenna and a planar antenna on a dielectric substrate. In particular, a high-accuracy analysis requires a full modeling of the coaxial feed line [22]–[24]. However, the total analytic region increases to comprise a very large number of cells when an analytic object is added not only to a detailed antenna structure but also to a coaxial cable. Therefore, the separate modeling of the antenna and feed line parts was proposed [25]. Under the assumption that the electromagnetic field within the coaxial line is TEM, the coaxial feed line can be replaced by a one-dimensional transmission line model that is simply connected to the antenna at the image plane. This is expected to shorten the calculation time, because the pulse reflected in the connection part with the antenna is absorbed in the Mur's first order absorbing boundary, which is set up under the transmission line. On the other hand, a simple gap feed model can include an internal resistance. The calculation time of the conventional FDTD should be compared with these feed models.

Planar antennas such as probe-fed and microstrip antennas are used in many applications to ensure that they are low-profile, compact, and easy to fabricate. The FDTD method is also used to evaluate the performance of these antennas. The modeling of a feed structure becomes extremely important when the FDTD method is used to analyze antenna characteristics. The calculations of the microstrip patch antenna, which is fed electric field above the ground plane, can be performed by the gap feed model [26]. This model has a stair-stepped transition from the electric field feed to the microstrip line, and it is used to provide a relatively smooth connection [27]. When the antenna size becomes compatible with the feed connector, its coaxial feed structure should be included in the FDTD simulation [19]. The coaxial aperture can be modeled by additional FDTD mesh edges of the perfect conductor, and the

internal resistance of the feed circuit can be considered in this model. However, when the size of the patch antenna is very small, the antenna characteristics are significantly affected by feed structures such as connectors.

When an antenna is installed on a finite-sized ground plane, its size and shape significantly change the characteristics of the antenna [28][29]. Although the treatment of the finite ground plane and analytic region are very important for the FDTD calculation, the details of its parameters have not been clarified. In addition, a taper shape at the feeding point becomes a matching parameter for the printed monopole antenna. This taper shape is approximated by a stair-stepped or a sub-cellular algorithm in the FDTD calculation [30][31]. Its modeling should be carefully chosen to obtain reliable results.

1.2.2 Cellular Base Station Antennas

The unique features of the Japanese cellular system are multi band operation, compact diversity antennas, electrical beam tilting, and indoor booster systems for high capacity systems [32].

Diversity reception systems are used at base stations for mobile communications to reduce the fading in a multipath environment. In this receiving system, several input waves are received. Depending on the antenna setup, the diversity may be of three types: space, pattern, and polarization. Space diversity reception systems, which use spatially separated antennas, and pattern diversity systems receive the waves from different directions. These have been widely used in Japan. In Japan, mobile communication systems were initially developed for automobile use. Thus, base station antennas and vehicular antennas have had vertical polarization as their co-polarization. However, at present, cellular phones radiate horizontal polarization more strongly than vertical polarization, because portable handsets are used at a tilt angle in the talking position. In this case, polarization diversity works effectively and base stations are miniaturized, because sector antennas can be completely installed inside one radome [33]–[36]. A twin-dipole antenna printed on a dielectric substrate was proposed as one of the diversity antennas. The same element can be used for the

vertical and horizontal polarization due to the 90° rotation of the antenna element [35][37]. In the same way, a bent patch antenna on the rooftop shaped ground plane to obtain same beam width between E- and H-plane was also presented [38]. Its base station consists of 3-sector polarization diversity antenna.

In the cellular phone system, the number of sectors in the wireless zone configuration of the base station antenna determines the half-power beam width (HPBW) in the horizontal plane. In a 3-sector configuration, the HPBW in the horizontal plane must be 120°. If a dipole antenna and a reflector are used, it is difficult to arrange a 120° HPBW in the horizontal plane in a horizontal polarization. Hence, a horizontal polarization element using two monopole antennas tilted on a reflector and fed with a phase difference of 180° was proposed [39][40]. On the other hand, for a use of 6-sector radio zone configuration, a 60° beam-width is required in the horizontal plane. A V-type dipole antenna was proposed as a horizontal polarization antenna, which has two sub-reflectors located on both ends of a main-reflector [41]. In addition, the bandwidth of transmission and reception is wide in the frequency band for the IMT2000 at 2GHz. A wide bandwidth horizontal polarization element is necessary to employ the polarization diversity for transmission and reception. A 60° beamwidth horizontal polarization element was proposed [42]. This element is realized about 29% bandwidth by arranging two parasitic elements on the both ends of dipole element. An omni-directional horizontal polarization element was reported [43][44]. A circular dipole element with a parasitic element radiate horizontally polarized waves.

These hybrid antennas often consist of a holed-patch antenna, which can adjust the resonant frequency under the condition of a terminated (open- or short-circuited) hole edge [45]–[47]. In a self-diplexing antenna using a two-layered patch antenna with a hole for satellite communications, the mutual coupling between transmission and reception has been examined in detail [48]. This antenna has a hole in the lower layer patch in order to feed the upper layer patch. It should be clear that the hole size influences the mutual coupling between the composite antennas. Several results have been obtained for the ring microstrip antenna (R-MSA), which is similar into configuration to a holed-patch antenna. For instance, the configuration and radiation characteristics for electromagnetically-coupled R-MSA elements have been reported

[49]. A horizontal polarized wide-beam antenna consisting of a holed rectangular patch element and a monopole element was proposed [50]. The E-plane beam width is broaden to the 110° by the radiation from monopole antenna fed with the phase difference of 90°.

An important characteristic of a base station antenna is low sidelobe level in order to suppress inter-cell interference, and is the sector beam in the horizontal plane [51]–[53]. At the same time, the load of the wind pressure on base station antennas should be minimized. However, it is difficult to be compatible with the short antenna aperture and the light load of the wind pressure. The antenna configuration is employed a cylindrical slender type for reduction of the wind pressure [54][55]. The frequencies assigned for base stations used in mobile communication are 900 MHz and 1.5 GHz for PDC and 2 GHz for IMT-2000 systems. If several frequency bands are assigned to an antenna, the multi-frequency antenna is needed from the points of view of economy, installation, and construction. The multi resonant antenna is obtained by using a parasitic element. The printed dipole antenna with a parasitic element was examined in detail, and the behaviors of parasitic elements to extend the bandwidth were presented [56][57][58]. A method for obtaining dual resonances by feeding several radiating elements with coupled lines has been reported [59]. In connection with these methods, parameters such as element length and element spacing have been studied extensively, and enhanced bandwidth or dual resonance of the antenna has been realized. However, in each method, the space occupied by the antenna increases, and the structure becomes more complicated, because an element that is resonant at a parasitic frequency must be added to the radiating element, which is resonant at the fundamental frequency.

A corner reflector antenna is used for base station antennas consisting of a reflector in addition to a radiating element within a radome. To increase subscriber capacity, the base station antennas are sectored. Hence, the HPBW of the antenna beam in the horizontal plane is an important property. This HPBW can be easily controlled by changing the shape of the reflector in the radome. However, it is difficult to realize equally divided sector beams in the horizontal plane for several resonant frequencies. A set of design guidelines for the HPBW has been reported [60][61]. The effect of

reflector placement on the impedance characteristics has also been reported [62].

A triple band antenna is required to support both the PDC and IMT-2000, and the space of an antenna construction should be reduced [63]. The antenna design becomes more complicated, and the three kinds of antennas in the following were designed.

- 0.9/1.5/2.0 GHz bands antenna of 120° beam [63][64]
- 0.9/1.5 GHz bands antenna of 120° beam and 2.0 GHz band antenna of 60° beam [65][66]
- 0.9/1.5 GHz bands antenna of 120° beam and 2.0 GHz band antenna of dual 60° beams [67][68]

The printed dipole antenna has been widely used as a radiating element, because the dipole antenna has a wide bandwidth of more than 15% for a return loss less than -10 dB. In practice, this antenna can be printed on a substrate so that several antennas can be easily fabricated. Since the dipole antenna consists of a balanced line, a balun is needed to transform the transmission mode if this antenna is fed by an unbalanced transmission line, such as a coaxial cable [69]–[71]. Dipole antennas with a balun consisting of a branching conductor have been reported [72]–[74].

1.2.3 Active Integrated Antennas

In next-generation mobile communications, adaptive antennas will become indispensable for realizing high-speed and wideband radio communications. An adaptive antenna system with a highly functional and compact design is essential for the base station to be of low cost and easy fabricated. An active integrated antenna is composed of the antenna, passive elements, and the active circuit on a substrate. Therefore, the active antenna is effectively miniaturized, and noise and transmission loss are decreased, and the antenna is adopted in digital beam-forming receivers [75]. When a system is composed of modules such as antennas or a circuit, the influence of the connection part (connector, cable) between each module should be considered.

An electromagnetic analysis becomes necessary to study the effect of these interconnections between each element in the case of the integrated antenna. In particular, an examination of the radiation pattern is important, and it should be clear that the cross polarization level of active patch antennas with the amplifier is high. The analysis and design methods of the field effect transistor (FET) for use in amplifiers have been reported. Commercial circuit simulators can directly analyze the FET by the equivalent circuit or the S parameters. The FET can also be evaluated by an electromagnetic analysis. On the other hand, combinations of the FDTD and circuit calculation methods are proposed. Examples of these include the voltage source approach, the current source approach, and the black box of the S parameter [76]–[80]. The method of solving the state equation of the circuit, the combination with SPICE, and the modeling of the measured S parameter have been proposed as circuit calculation techniques [81].

A full-wave analysis of packaged microwave circuits with the FET is presented [76]. The small-signal circuit model of the FET was used, and the gate capacitor and drain current are shown by the Cartice Ettembelg model. This model is a basic equivalent circuit and is characterized by the intrinsic gallium arsenide field-effect transistor (GaAsFET). This cannot be applied to TriQuint's Own Model (TOM), which is a large-signal circuit FET model [82][83][84]. Furthermore, the FET was implemented by TOM for several microwave circuit applications [79]. However, little is known about this antenna problem. The equivalent circuit parameters of TOM are prepared by a device sheet, and the network analyzer performs the parameter extraction function. The FET, as actually used, can be expressed precisely in the analysis. Therefore, an active integrated antenna that is explained by TOM should be evaluated by total modeling, including the coupling between each element. In particular, FDTD can analyze the radiation pattern and electromagnetic distribution. Therefore, in the future, it can be an effective technique for use in analytic methods. For example, it can be used in designing high-frequency circuits and ensuring electromagnetic compatibility.

One of the applications of active antennas using GaAsFET is the self-oscillating

mixer with electromagnetically-coupled antenna elements [86][87]. An active integrated antenna with an oscillator is connected to the GaAsFET and coplanar waveguide, and it determines the oscillating frequency by modulating an applied bias voltage. Since the IF output level is small, the parasitic element is arranged for the receiving antenna, and the shape and position of the parasitic element is examined through the measurement. This antenna structure should be examined by electromagnetic analysis, because an oscillating condition significantly depends on the coupling between the elements.

1.2.4 Repeater Systems

The micro cellular system is used for PDC system, and the covered area is expanding to include tunnels, subway stations, and inside large buildings [88]. The optical transmission booster system is used for long tunnels instead of the leaky coaxial cable system [89][90]. A bi-directional notch antenna for tunnels is a pair of notch antennas excited out of phase, which has wide bandwidth and low-profile [91]. In building antennas are top loaded monopole antennas designed by the FDTD analysis [91][92]. The pager system at 280 MHz band is also included for these system.

Booster systems for pager and cellular system, to be used in open areas, have already been proposed. The uncovered areas such as the shade of mountains and buildings can be eliminated by repeater systems between the base and mobile stations. The gain control function is needed for the booster systems in order to stop the oscillation caused by the interference waves between a transmitting and receiving antenna. A loop canceling booster including adaptive canceling function has been reported [93]–[98]. A CDMA Repeater with echo canceller, which can separate a desired wave and an interference wave from the received signal, was developed [99]. A frequency converting repeater can be also provide an equivalent service area without a wire line between switching center and base station [100]–[102].

A frequency offset booster was proposed to realize the re-radiation system at an open area for cellular and vehicular communications. This system is arranged with back-to-back antennas, one pointing toward the base station and the other toward the

mobile terminal. A mutual coupling between the antennas should be designed such that it is lager than the amplifier gain. Two dipole antenna on dual box reflector can suppress a mutual coupling with small distance between antennas [104]. The transmitting antenna array can improve the coupling between antennas attached to a metal cylinder [105]–[107]. The measurement of a 2.6 GHz choke-loaded patch array antenna has been reported, and the specification of the mutual coupling was less than -80 dB [108]. The quarter-wavelength choke was loaded with the edge of a microstrip patch array antenna, and the side lobe level (SLL) of over 90° were decreased. Repeater systems will also become practical in the IMT-2000 system in order to provide services in locations where radio waves cannot currently reach. The new system requires 80 dB for the amplifier gain, and the mutual coupling between the antennas must be less than -100 dB including a margin. The evaluation of the mutual coupling of -100 dB between the transmitting and receiving antennas requires a highly accurate analysis, and it is difficult to optimize the structure through the measurement.

The space between the antennas is established using a metal block, which accommodates the electronic devices, such as amplifiers, phase shifters, filters, a power supply, etc. If the size of the ground plane increases or the distance between the elements decreases, the mutual coupling between the elements can be restrained using antennas that are arranged back-to-back. However, there is a limitation in terms of the physical size of the pillars supporting the antenna in the repeater installation; therefore, it is important to examine how coupling can be restrained in a compact composition. In addition, a major problem arises when the value of the mutual coupling changes due to the environmental set-up of the repeater, regardless of whether the shape or position of the antenna is optimized.

1.3 Summary of the Remaining Chapters

The objective of this study is to propose a modeling of mobile communication antennas by the FDTD method and its applications. This dissertation discusses the following:

1. Modeling of an antenna and its immediate environment

2. Modeling of an equivalent circuit

Chapter 2 presents a modeling of the hybrid polarization diversity antenna with a side reflector. A highly accurate analysis is required to realize the coupling of -30 dB between each element for vertical and horizontal polarization. The HPBW of base stations, which is determined by the side reflector, is also designed for the various sectors. A basic technique (especially, with respect to achieving accuracy and reducing the calculation time) for FDTD analysis is discussed to examine the effect of the immediate environment of the antennas. The horizontal HPBWs of a dipole antenna and a holed patch antenna are optimized by modeling the side reflector. The mutual coupling of the hybrid antenna, which can be arranged in the same position, is analyzed and compared with the measurement.

Chapter 3 presents a mutual coupling between a transmitting and receiving antenna with a choke. The repeater system requires a coupling of -100 dB, and it is difficult to obtain its value through the measurement. The increase in the front-to-back (FB) or side ratio causes the suppression of mutual coupling in the case of 4-element and 16-element arrays. Optimum choke parameters and SLL, achieved using binomial, Chebyshev and Taylor arrays, attain a mutual coupling of -100 dB. The validity of this structure is confirmed by the measurement.

Chapter 4 presents the modeling of a balun to feed a dual frequency antenna. The operating principle of a dual frequency antenna is proved with the modeling of the equivalent circuit of balun. The parameters of a series-connected open stub and a parallel-connected short are examined in detail. The stub length can help realize the multi-frequency operation.

Chapter 5 presents the modeling of a GaAsFET for an active integrated antenna. The modeling of the equivalent circuit of an active element is described in detail. The characteristics of the integrated antenna can be accurately computed using the modeling of a bias circuit and a finite ground plane. An active integrated antenna with an oscillator, which is used the self-oscillating mixer with electromagnetically-coupled antenna elements, is also examined. The voltage source, which is precisely modeled the actual structure for a coplanar waveguide, and an oscillating condition are presented.

Chapter 6 concludes this study.

Figure 1.1 shows the structure of this dissertation.

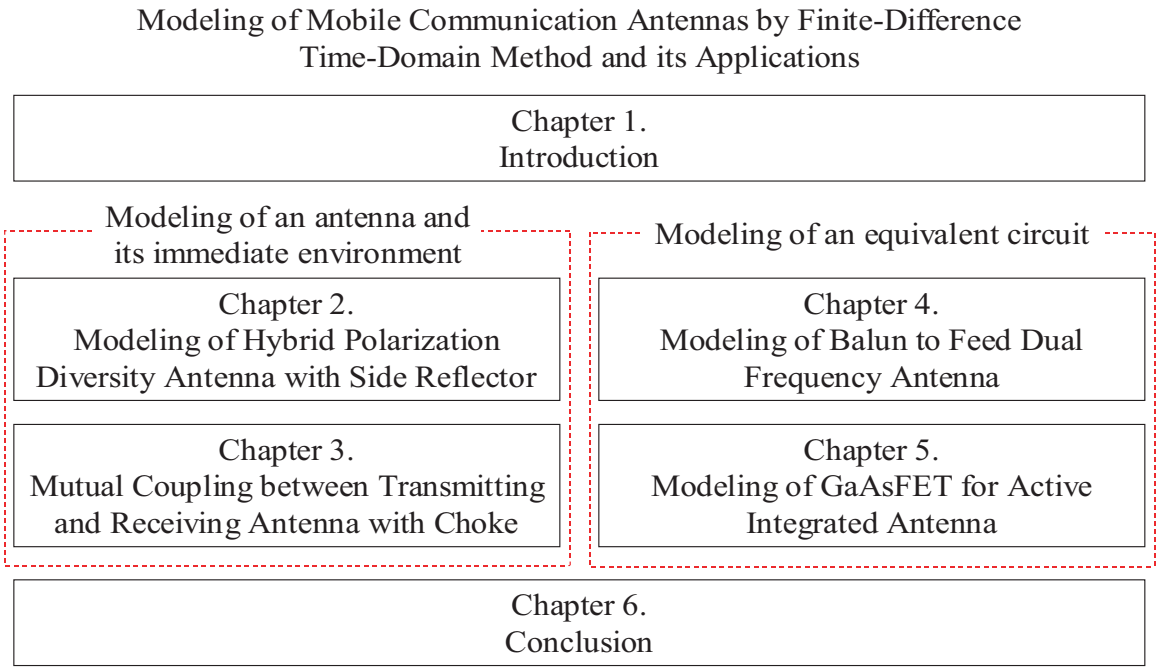

Figure 1.1: Structure of this dissertation

Chapter 2

Modeling of Hybrid Polarization Diversity Antenna with Side Reflector

2.1 Introduction

In this chapter, we presents a modeling of the hybrid polarization diversity antenna with a side reflector. A highly accurate analysis is required to realize the coupling of −30 dB between each element for vertical and horizontal polarization. First, a basic technique (especially, with respect to achieving accuracy and reducing the calculation time) for FDTD analysis is discussed to examine the effect of the immediate environment of the antennas. The iteration for the convergence when using a gap feed model with an internal resistance, is examined in comparison with that obtained the usual gap feed model and the transmission line model. We also investigate the minimum analytic region to accurately include the influence of a finite ground plane. The guidelines obtained through the parameter study are very efficient in reducing the computing resource in an FDTD calculation. We also presents a modeling technique to feed two kinds of antennas. We investigate the contour-path (CP) modeling of the feed and short pins for a planar inverted-F antenna. The impedance of the antenna can be computed precisely by modeling the radius of the pin based on the results

of the detailed examination. We also examined the modeling of the coaxial cable to feed a microstrip patch antenna and compared this result with that obtained using a microstrip feed model.

As an application of the highly accurate antenna analysis, the hybrid polarization diversity antenna with a side reflector is proposed. Due to an increase in the subscriber capacity of the IMT-2000 system, a 6-sector wireless zone configuration has been introduced [63]. Hence, the beam width is 60°. Furthermore, the frequency range used is 1,920–1,980 MHz for the up-link and 2,110–2,170 MHz for the down-link. In the latter part of this chapter, the introduction of this IMT-2000 system is taken into consideration, and the design of a 60° beam polarization diversity antenna is considered. In particular, a small diversity antenna element is proposed, in which a printed dipole is used as a vertical polarization element and a patch antenna with a hole is used as a horizontal polarization element. The basis for using this antenna configuration is described below. When base station antennas are mass produced in practice, a planar structure formed by printing on the same dielectric substrate is suitable. Hence, an analysis that includes the substrate is needed. Additionally, since both the vertical and horizontal elements can be placed at the same location, the installation space can be reduced. Further, the dipole can be easily broad-banded by parasitic elements and can be used for multiple frequencies. The beam width can be controlled by appropriately adjusting the reflector shape. On the other hand, a holed patch antenna, designed as an element for use in combination with the dipole, allows selection of the polarization plane by the feed location. The transmission line for feeding the dipole can pass through the antenna. These are some of the reasons for using this configuration. With regard to the printed dipole, the ground plane parameters that determine the half power beam width (HPBW) in the horizontal plane are optimized. With regard to the holed patch antenna, the resonant frequency affected by the hole shape, the HPBW in the horizontal plane, and mutual coupling in a composite structure are discussed. The characteristics of each antenna element alone are analyzed by the FDTD method and are compared with the experimental data. Finally, the characteristics of the proposed composite polarization diversity antenna are analyzed and compared with the experimental results.

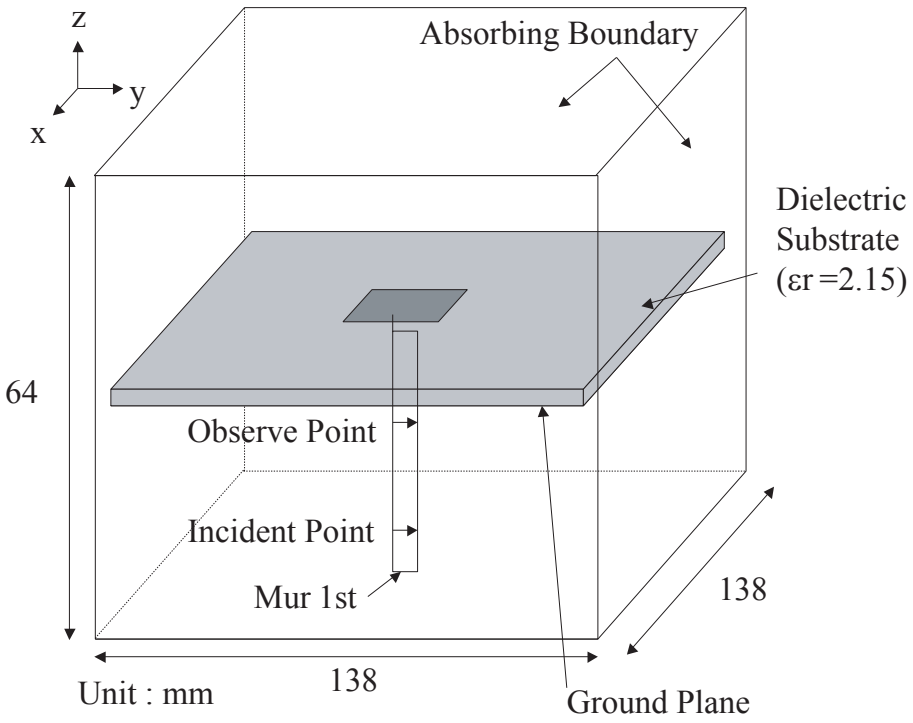

Figure 2.1: Anlytic model for patch antenna using transmission line feed model

2.2 Antenna Analysis Techniques

2.2.1 Antenna Feed Model

When the electric excitation is used as an antenna feed model, the computation time for a patch antenna is generally long, because the feed current is not easily converged. Therefore, a reduction in the calculation time is required. Figure 2.1 shows a probe-fed microstrip antenna which is analyzed by a transmission line feed, and gap feed with an internal resistor. Figure 2.2 shows the detailed parameters of the patch antenna.

Figure 2.1 shows the transmission line feed model which is connected to the coaxial line [25]. The coaxial line can be replaced with a one-dimensional transmission line. The analytic region includes the antenna and this feed line, and each of these is calculated separately. Mur's first order absorbing boundary is set up at the bottom

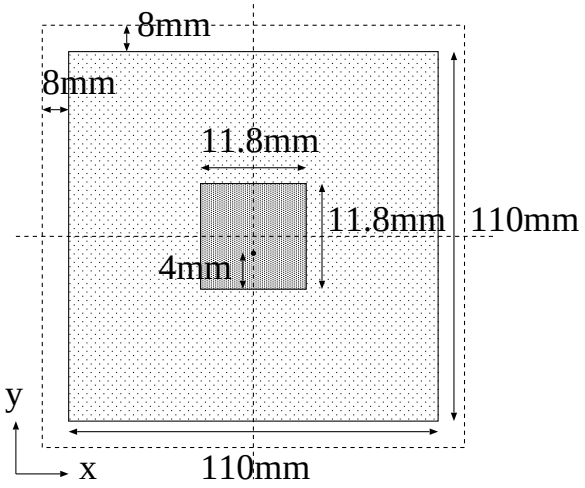

Figure 2.2: Structure parameters of patch antenna

of the transmission line, and the reflection coefficient is calculated by the voltage of the incident point and the observation point, as shown in Fig. 2.1. This feed method shortens the convergent time of the feed current, because the incident voltage is attenuated before reaching an antenna connection part, and a reflection wave from the antenna is absorbed by the absorbing boundary of the transmission line.

The feed current is calculated by the contour integration of the magnetic in-feed point, and the input voltage is given by substituting internal resistance in Ohm's law. Therefore, the iteration can be reduced, because a loss of internal resistance can be added to the FDTD analysis, as shown in Fig. 2.3. Figure 2.4 shows the experimental and analytic results in the case of the transmission line and the gap feed with internal resistance. The analytic result in each feed method is in agreement with the experiment result. Figure 2.5 shows a feed current of a simple gap feed. A feed current of 10^{-2} is confirmed at 550,000 steps, but the value of the convergence value is too small to enable an accurate analysis. The calculation time for 550,000 steps is 154 h on a Dual Xeon 3.2 GHz PC, and the iteration for taking the convergence value of 10^{-4} is expected to be 2.4 million steps. Figure 2.6 shows the feed current of the transmission line feed. A feed current of 10^{-4} is confirmed at 70,000 steps; calculation time is 21 h. Figure 2.7 shows the feed current of the gap feed with an

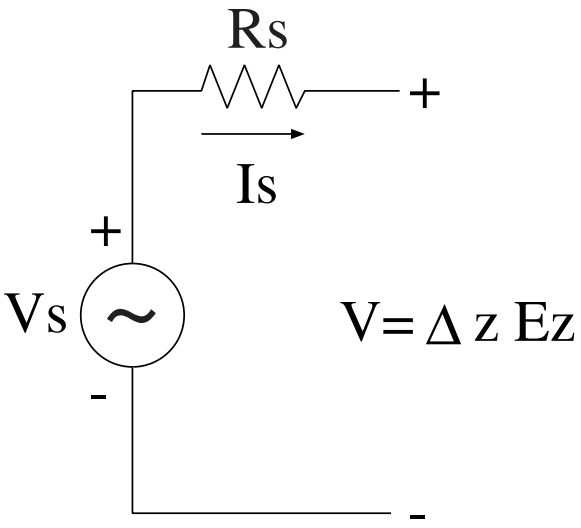

Figure 2.3: Equivalent circuit of feed point

internal resistance of 50 Ω. The feed current of 10^{-4} is confirmed at 8,000 steps, and the calculation time is 2 h. Therefore, the iteration for the convergence when using a gap feed model with an internal resistance, can be decreased to 1/300 in comparison with that obtained the usual gap feed model.

Figure 2.8 shows a microstrip patch antenna connected with the coaxial feed. The length of the coaxial cable model is 19.4 mm, and the diameters of the inner and outer conductors are 0.7 mm and 4.6 mm, respectively. Figure 2.9 shows the antenna feed models of the cross section at the feed point [27]. The connection between the coaxial cable and the microstrip line is achieved by sticking out the inner conductor by 3.8 mm. The coaxial cable is simplified by using the square pillar. The FDTD analytic conditions are as follows: The cell size is $\Delta x = \Delta y = 0.389$ mm and $\Delta z = 0.265$ mm; and the number of time steps is 12,000. The absorbing boundary condition of the perfectly matched layer (PML) is 8 layers, and the space between the antenna structure and the PML is 20 cells.

Figure 2.10 shows the return loss characteristics of a microstrip and coaxial feed model. The error toward the experiment result of a resonant frequency is improved by 0.4% (coaxial feed) from 1.6% (microstrip feed). As a result, the coaxial feed model

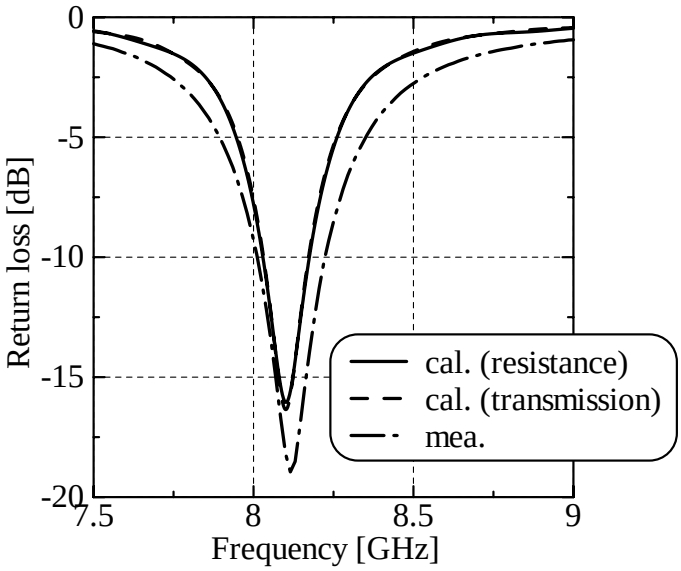

Figure 2.4: Return loss characteristics of two antenna feed types

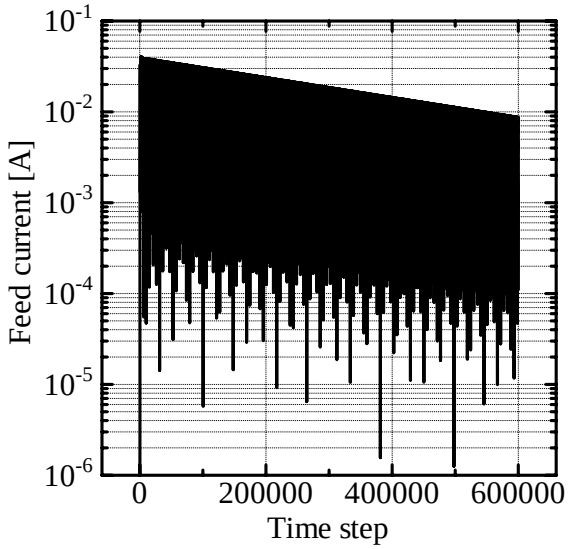

Figure 2.5: Convergent characteristics of feed current (simple gap feed)

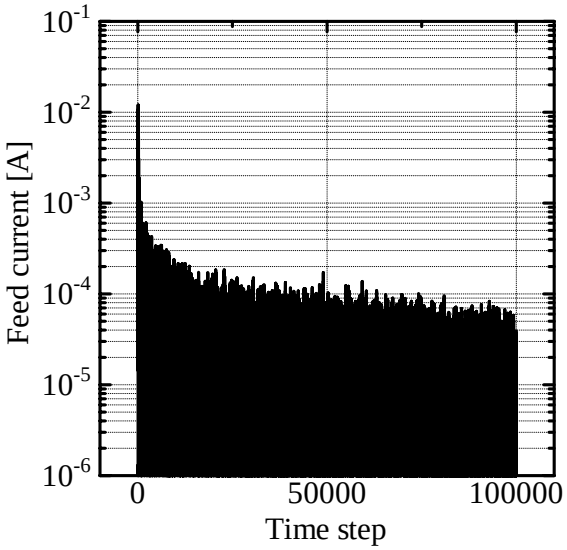

Figure 2.6: Convergent characteristics of feed current (transmission line model)

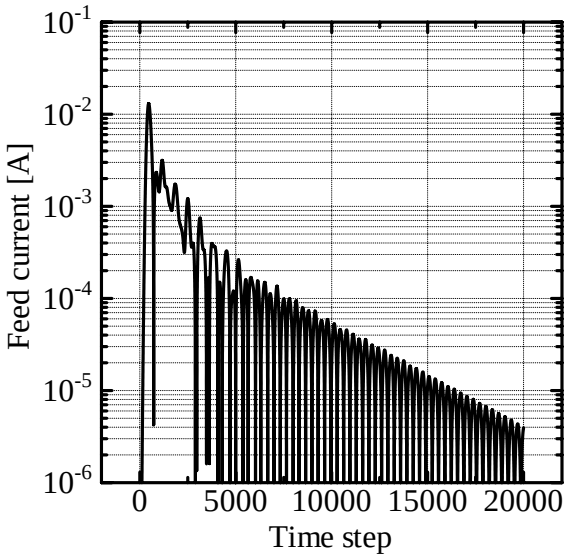

Figure 2.7: Convergent characteristics of feed current (include internal resistance)

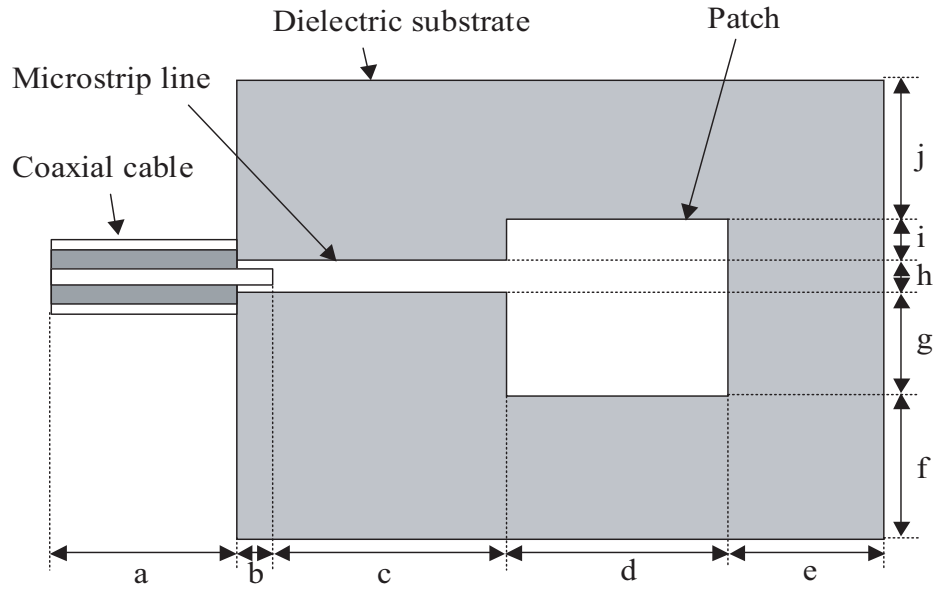

a=19.4, b=3.8, c=15.7, d=15.6, e=11.7, f=9.3, g=7.0, h=2.3, i=2.7, j=9.3 [mm]

Figure 2.8: Structure of microstrip patch antenna.

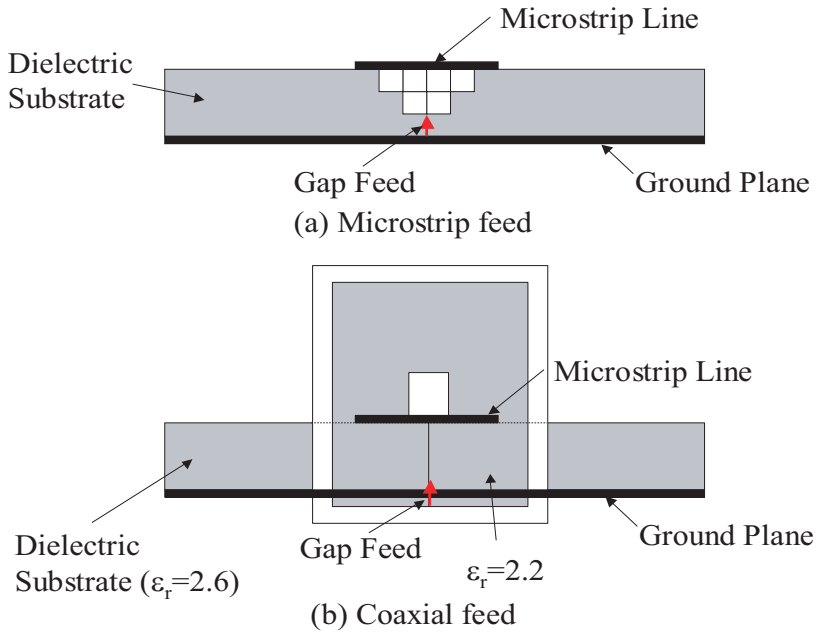

Figure 2.9: Antenna feed model for exciting microstrip patch antenna.

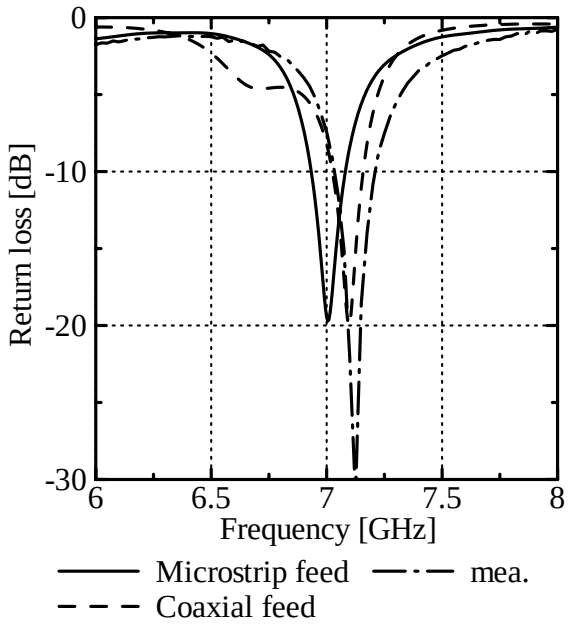

Figure 2.10: Return loss characteristics of microstrip and coaxial feed model.

vibrates at approximately 6.5–7.0 GHz, because the feed current is not converged. The number of time steps for feed current convergence is 6,000 in the case of a microstrip feed model. However, the coaxial feed model is not converged even if it is calculated to 12,000 steps. The convergent time is long because the wave reflected on both ends of the coaxial cable does not vanish for a long time.

2.2.2 Required Analytic Region

We discuss the minimum analytic region to accurately analyze the influence of the finite ground plane. Figure 2.11 shows the analytic model of the printed monopole antenna on a finite ground plane. The size of the square-shaped ground plane is $\lambda/2 \times \lambda/2$, where λ is the wavelength in free space at the resonant frequency of the antenna. Figure 2.12 shows the side view of the analytic region. The parameters in the FDTD analysis are h, s, and d. The length h is the distance between the bottom absorbing boundary and the ground plane, and d is the size of the ground plane. The length s is the distance between the absorbing boundary and the edge of the

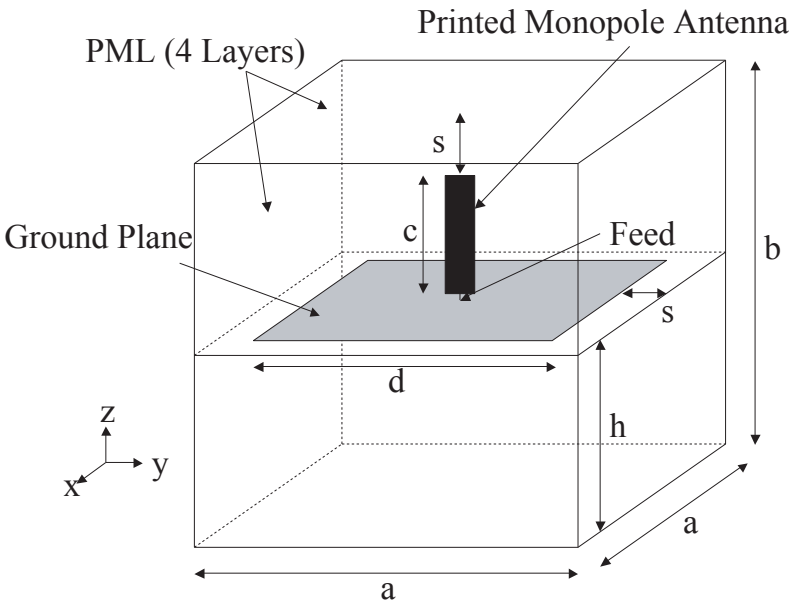

Figure 2.11: Analytic model of printed monopole antenna

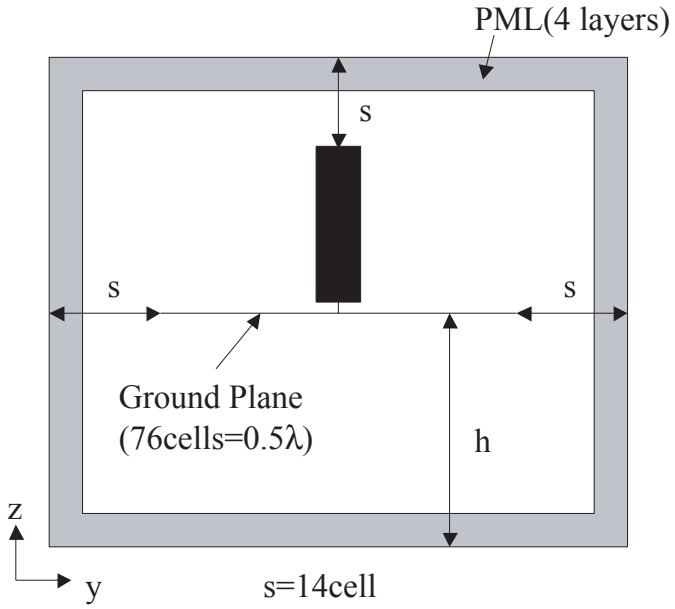

Figure 2.12: Parameters of analytic region for printed monopole antenna

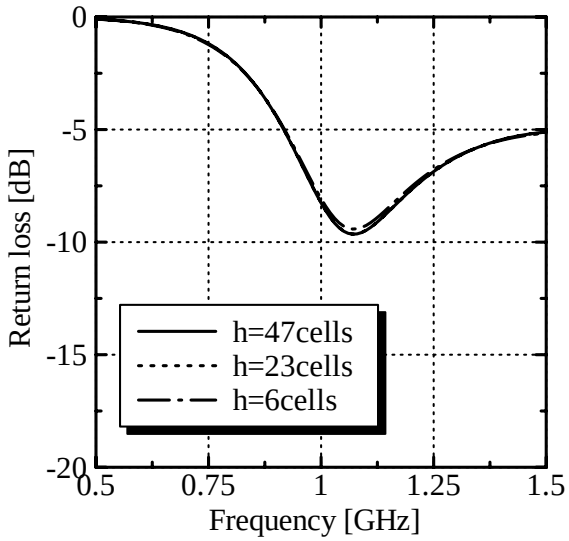

Figure 2.13: Return loss characteristics when parameter h is varied.

ground plane. This parameter refers to the free space outside the edge of the ground plane plus four cells for the PML. The other parameters in the FDTD analysis are as follows: The cell size of the uniform mesh is 0.5 mm, and the feed model includes the source resistance of 50 Ω. A 4-layer PML is adopted as the absorbing boundary condition. Figure 2.13 shows the return loss characteristics when the parameter h is varied. The parameter h does not have an effect on the resonance of the printed monopole antenna. Figures 2.14 and 2.15 show the radiation pattern in the E plane for the various values of h. The radiation pattern is initialized at the parameter $h =$ 47 cells, and each pattern is similar in the case of $h \leq 10$ cells. The error of the gain appears in the case of $h =$ 8cells as shown in Fig. 2.15. The minimum number of cells in this example is 10 for both h and s for any ground plane size of d to obtain the correct radiation pattern. This guideline is very effective in reducing the computing resource in an FDTD calculation.

Based on the above discussion, we investigated the input impedance of the printed monopole antenna on the ground planes of various sizes. Figure 2.16 shows the real and imaginary part of the input impedance when the parameter d is varied. The radiation resistance changes greatly though the resonant frequency doesn't change,

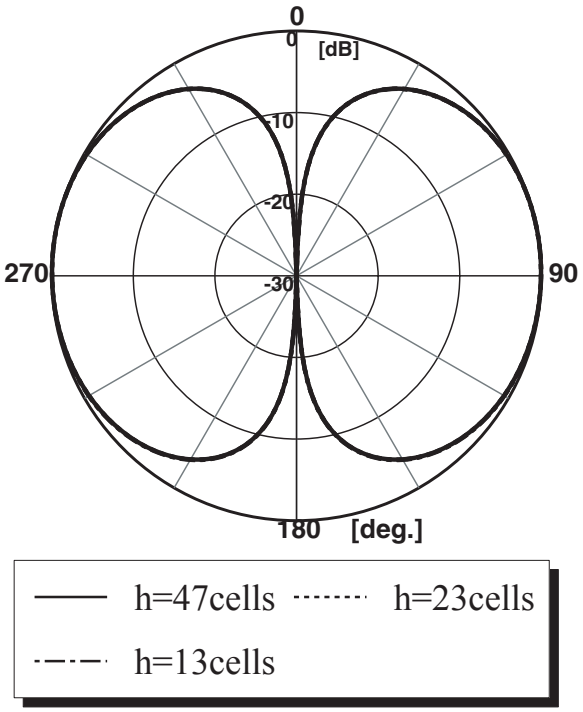

Figure 2.14: Radiation pattern (h≥13cells)

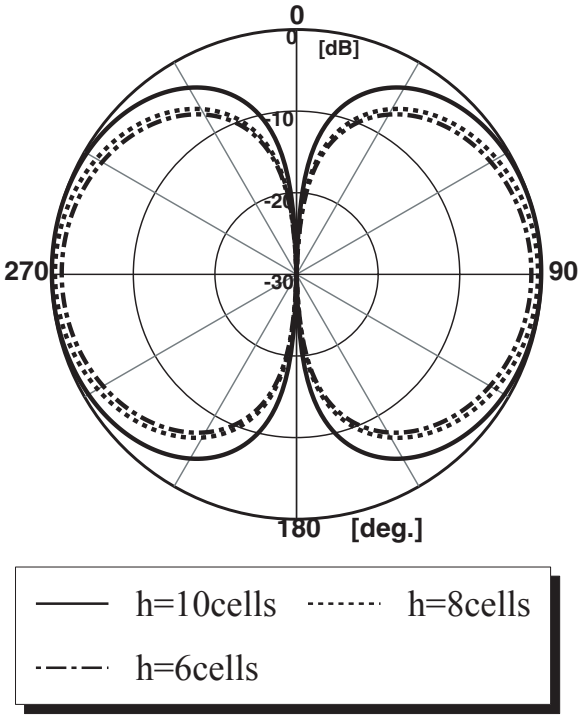

Figure 2.15: Radiation pattern (h≤10cells)

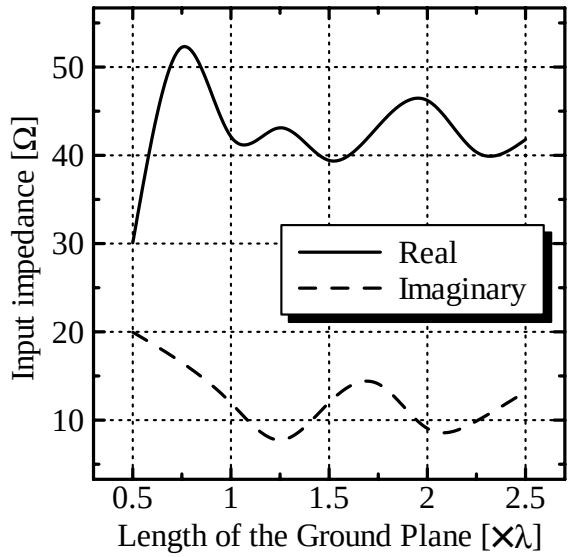

Figure 2.16: Input impedance with various ground plane sizes

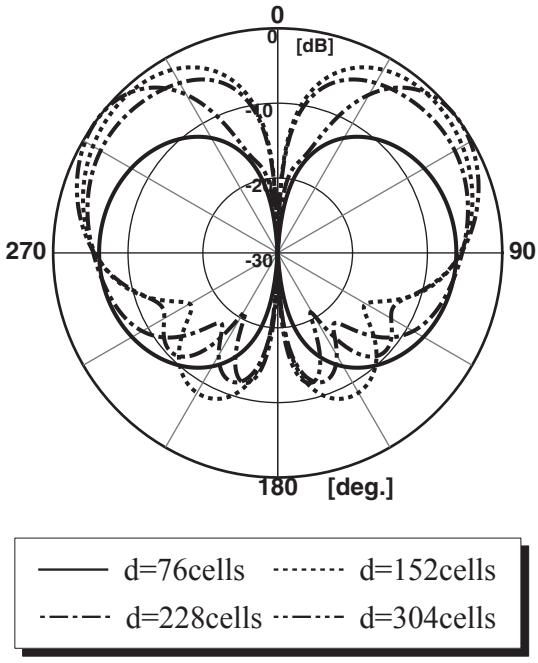

Figure 2.17: Radiation pattern with various ground plane sizes

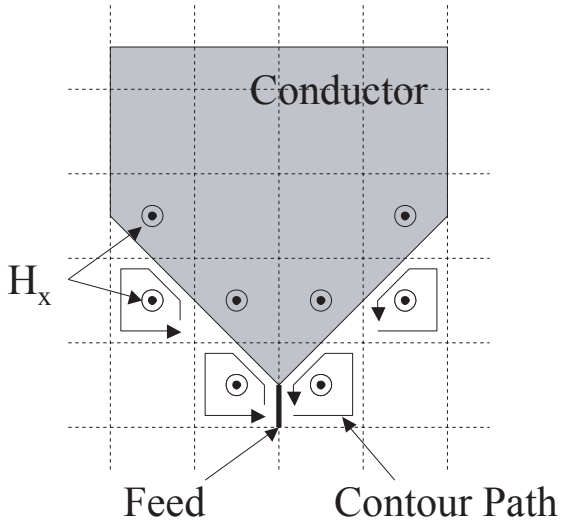

Figure 2.18: Sub-cellular technique for taper shape

and each part of the input impedance converges to a constant, as shown in Fig. 2.16. Figure 2.17 shows the radiation pattern in the E plane with various values of parameter d. The maximum radiation direction is in a tilt angle, and the radiation pattern of the back of the ground plane is minimized. Therefore, the characteristics of the larger ground plane can be regarded as an infinite ground plane.

2.2.3 Contour-Path FDTD Modeling

We discuss the analytic models of taper at the feeding point, and the approximation of this taper shape is shown in Fig. 2.18. The shape of the taper at the feeding point becomes a matching parameter for the printed monopole antenna. In this examination, the monopole antenna is printed on the dielectric substrate ($\varepsilon_r = 4.15$ and thickness = 1 mm), and it is arranged on the infinite ground plane. Figures 2.19 and 2.20 show the return loss characteristics compared with the calculated results and measurements for each cell size. When we used very fine grids (cell size = 1 mm (= 1/375 λ) in this case), no difference in the calculated results of either the sub-cellular technique or the stair-stepped approximation was observed. Moreover, the calculated results were in agreement with the measurements.

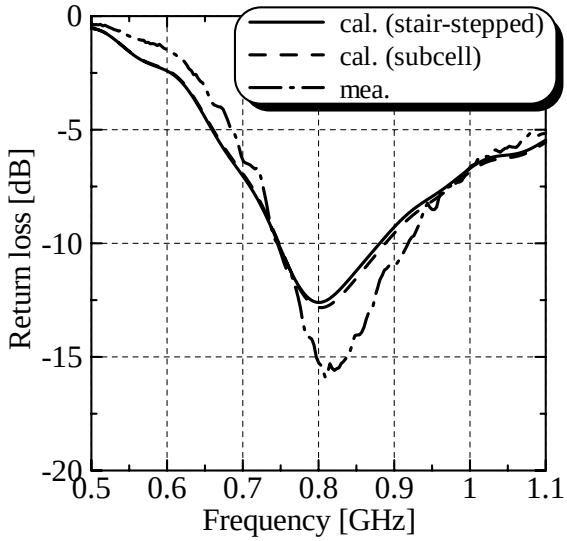

Figure 2.19: Return loss characteristics (cell size 4 mm)

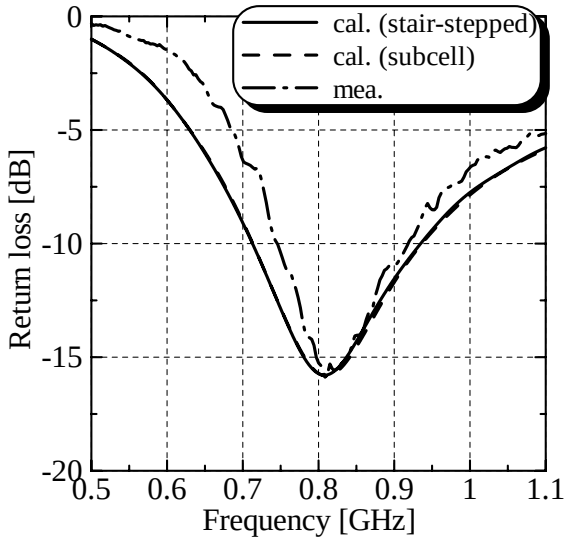

Figure 2.20: Return loss characteristics (cell size 1 mm)

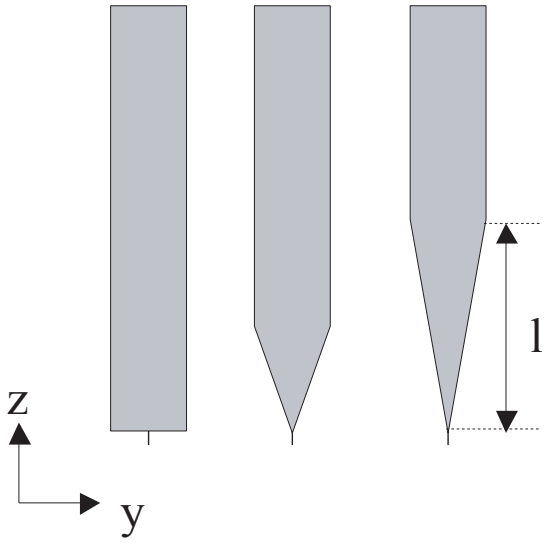

Figure 2.21: Parameter of taper shape

Figure 2.21 shows the various taper shapes of the printed monopole antenna. Taper length l changes the reactance component of the input impedance of the printed monopole antenna. Figures 2.22 and 2.23 show the return loss characteristics when the parameter l is varied. The resonant frequency falls due to the steep inclination of the reactance component, which results from the long length l.

Figure 2.24 shows a planar inverted-F antenna which is fed on the corner of the patch, and impedance matching can be achieved by using two short pins. The position of the short pin, which is close to the feed pin, influences the impedance matching condition, and another short pin influences the resonant frequency in this antenna. The FDTD analytic conditions are as follows: The cell size is $\Delta x = \Delta y = 0.5$ mm and $\Delta z = 0.555$ mm; and the number of time steps is 30,000. The absorbing boundary condition is an 8-layer PML. Figure 2.25 shows the modeling of the feed point and short pins. Perfect electric conductors (patch, ground plane, and pins) are modelled by making the electric field component zero, as shown with the bold line. The feed pin can be modeled by a square pillar of 2 $\times$ 2 cells, because its radius is 0.5 mm. The radiuses of the short pins are 0.15 mm each, and they form a structure that is smaller in size than the cell. This thin wire can be considered by applying Faraday's

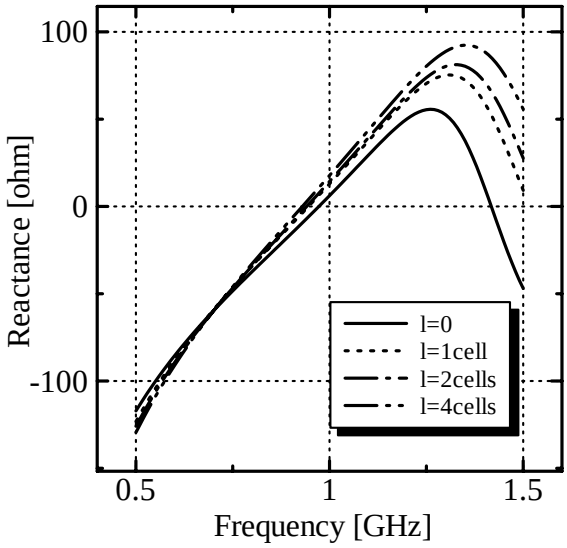

Figure 2.22: Reactance component (l≤4 cells)

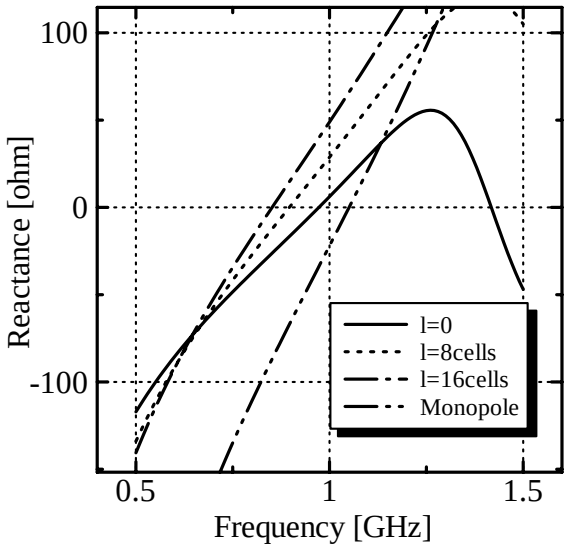

Figure 2.23: Reactance component (l≤16 cells)

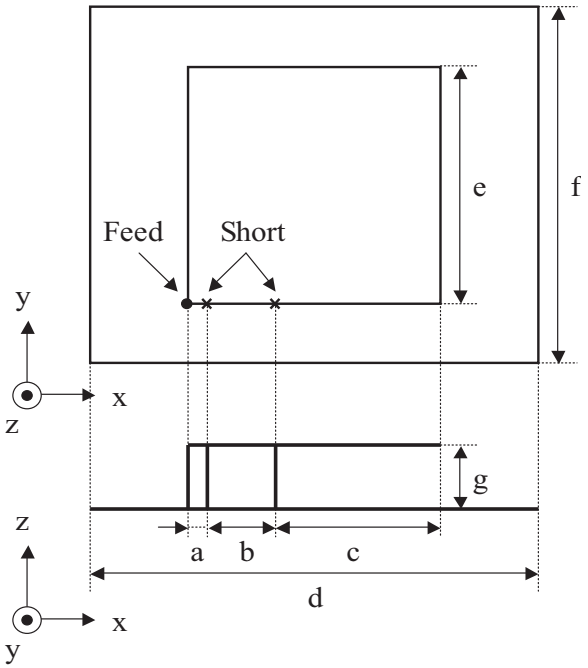

a=2.0, b=12.5, c=26.5, d=70.0, e=41.0, f=60.0, g=11.1 [mm]

Figure 2.24: Structure of planar inverted-F antenna.

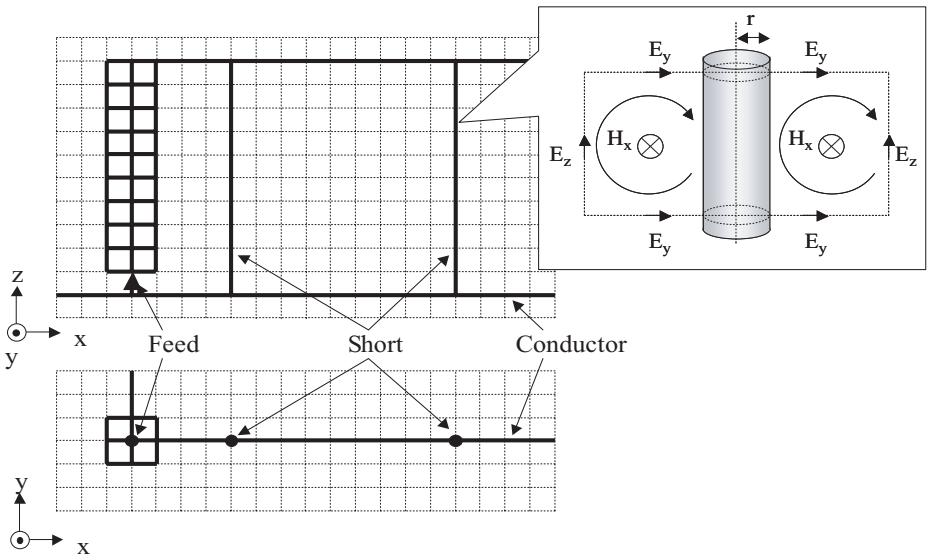

Figure 2.25: Modeling of feed point and short pin.

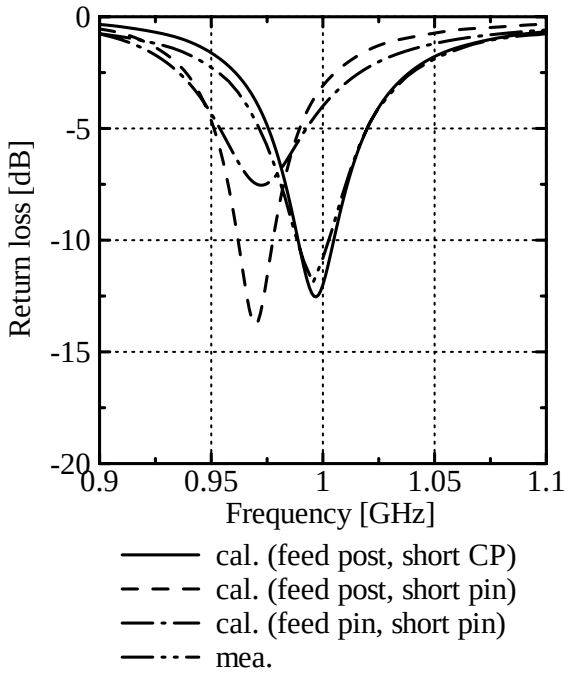

Figure 2.26: Return loss characteristics of various modeling of feed pin and short pin of planar inverted-F antenna.

Law to cells closest to the wire [19].

Figure 2.26 shows the return loss characteristics when the modeling of the feed and short pins is examined. The resonant frequency shifts to the lower side in comparison with the experiment result when The feed and short pins are modeled by the conductor line filament (feed pin, short pins). The resonant frequency does not change though a good impedance matching can be achieved because reactance components change when The feed pin is modeled by a square pillar (feed post, short pins). When the radius of the short pins is considered by CP modeling (feed post, short CP), the impedance-matching condition still changes due to an increase in the reactance component, and the analytic result is in agreement with the experiment result.

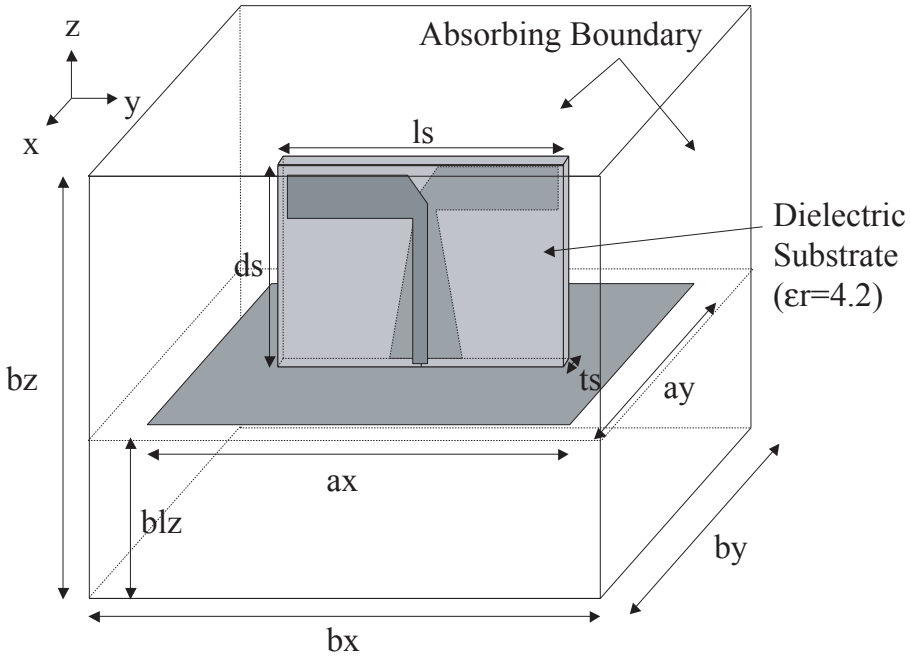

ax=ay=150,bx=by=164,bz=42.5,blx=7,ls=57,ds=28.5.ts=1[mm]

Figure 2.27: Printed dipole antenna on dielectric substrate

2.3 Modeling of Antenna and Reflector

2.3.1 Printed Dipole Antenna

A dipole antenna printed on both sides of a dielectric substrate placed on a reflector is used as a vertical polarization element. Since the dipole antenna is fed by an unbalanced line, a balun is needed when an unbalanced-line coaxial cable is used for feeding. An antenna with an integrated balun has been proposed, and its operation investigate in chapter 4. In this section, a printed dipole antenna fed by a $\lambda/4$ Lecher wire is studied to confirm the basic configuration.

In excitation with a Lecher wire, matching with a 50 Ω line is facilitated if the distance between the dipole and the reflector is set to approximately $\lambda/4$. The antenna height ld is set as 24 mm (0.16 λ). By varying the reflector shape, the beam width in the horizontal plane can easily be controlled. Here, we describe an FDTD analysis

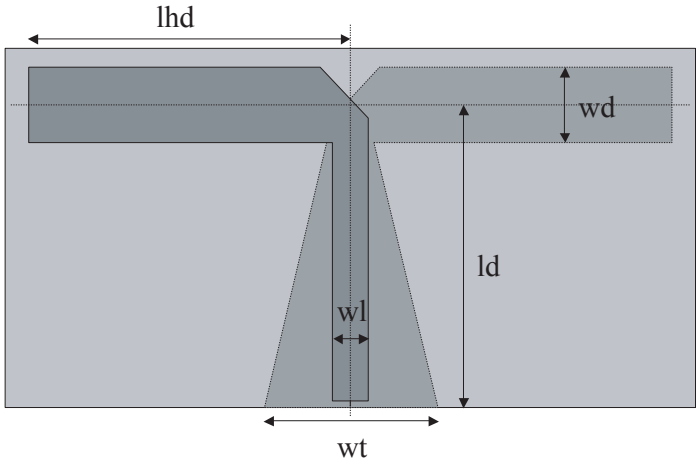

lhd=27,wd=6,wl=3,wt=14,ld=24[mm]

Figure 2.28: Detail of printed dipole antenna

Table 2.1: Common condition for FDTD analysis

Absorbing boundary condition	PML-4 layers
Iteration	6,000
Incident voltage	Gaussian pulse
Feed type	Gap feed with 50Ω

for a printed dipole antenna on a dielectric substrate placed on a finite ground plane, as shown in Fig. 2.27. Figure 2.28 shows the detailed structural specifications of the dipole antenna. The specifications needed for the FDTD analysis are the cell sizes in the x, y, and z directions, all of which are 0.5 mm, in addition to the common parameters listed in Table 2.1. The analysis domain is 328 × 328 × 85 cells.

The return loss characteristics of the FDTD analysis and the experimental results under the above conditions are shown in Fig. 2.29. The radiation patterns are shown in Fig. 2.30. The radiation patterns are normalized to the maximum value of the co-polarization in each plane. Figures 2.29 and 2.30 show that the analytical and experimental results are in agreement. Given this agreement, the HPBW of the radiation pattern in the horizontal plane of the printed dipole placed on a finite

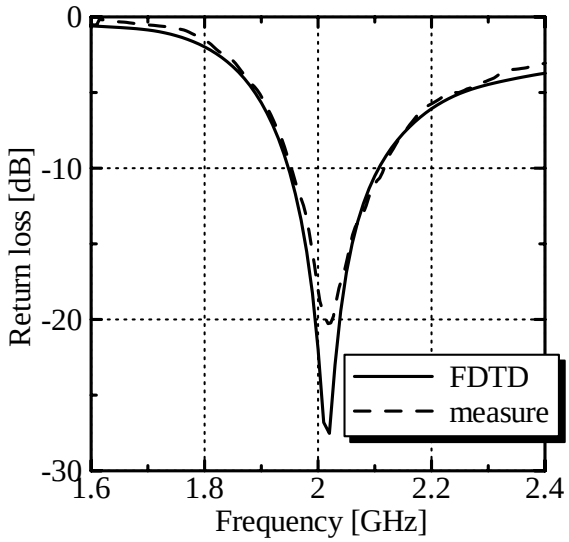

Figure 2.29: Return loss characteristics of printed dipole

ground plane is discussed. Figure 2.32 shows the variations in the HPBW in the horizontal plane. The length lg of the ground plane is in the horizontal direction, and the conductor length lb for the edge of the ground plane is folded upward from the ground plane (toward the dipole side), as shown in Fig. 2.31. These are used as the parameters. The values of lg are 1.0 λ, 1.1 λ, and 1.2 λ; the ground plane is infinite in the vertical direction (the y direction in the figure). Note that in practical base station antennas, corner reflectors with a curved reflector surface are often used to reduce the radome radius [55]. This, in turn, reduces the wind loads. However, a reflector without curvature is studied to confirm the basic structure. The range of lg is such that the HPBW in the horizontal plane can be brought close to 60° by adjusting lb.

It can be observed in Fig. 2.32, that the HPBW in the horizontal plane is inversely proportional to lb, and it reaches its minimum value if lb is between 0.2 λ and 0.3 λ. From the above studies, the relationship between the HPBW of the printed dipole in the horizontal plane and the ground plane parameter is elucidated, making it possible to realize a 60° beam.

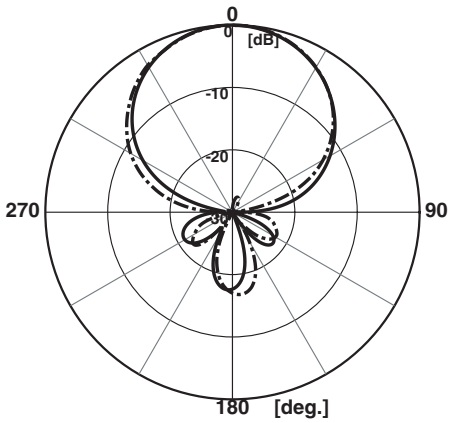

—— E_θ (FDTD) ····· E_ϕ (FDTD)

–·–·– E_θ (measure) –··–·· E_ϕ (measure)

(a) E-plane

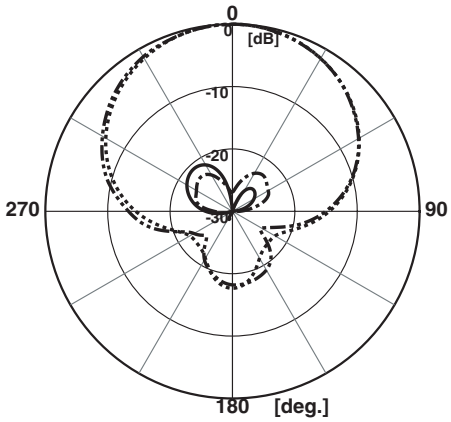

—— E_θ (FDTD) ····· E_ϕ (FDTD)

–·–·– E_θ (measure) –··–·· E_ϕ (measure)

(b) H-plane

Figure 2.30: Radiation Pattern of printed dipole

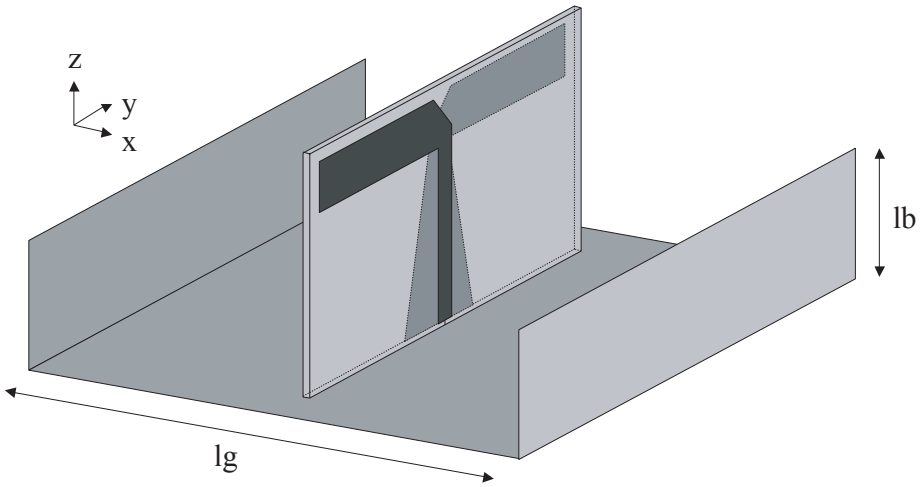

Figure 2.31: Parameters *lg* and *lb* for examination of horizontal beam width

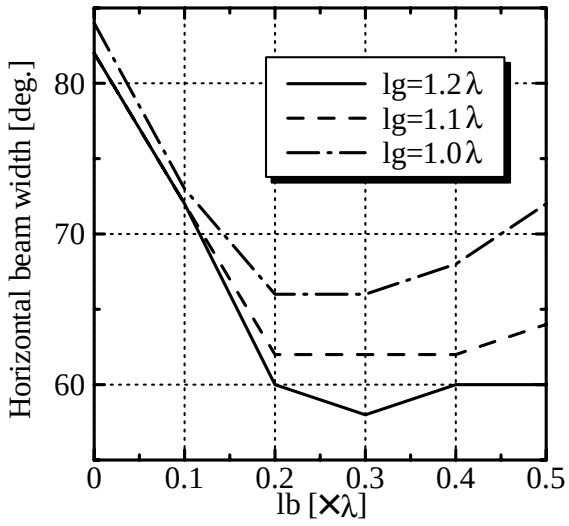

Figure 2.32: Horizontal beam width of printed dipole when patameter *lb* is varied

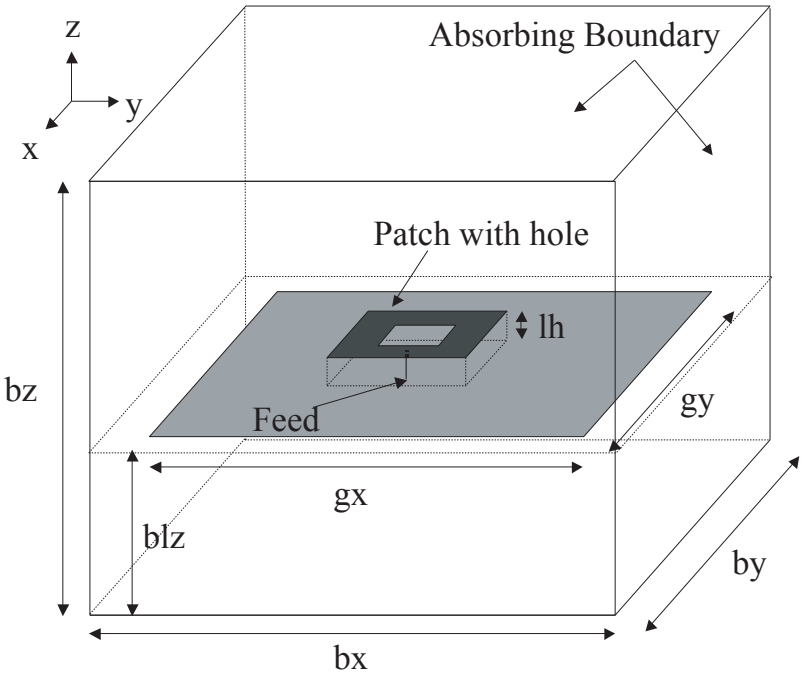

bx=by=178,bz=40,blz=14,gx=gy=150,lh=12[mm]

Figure 2.33: Analytic model of holed patch antenna

2.3.2 Holed Patch Antenna

The ground plane shape for a 60° HPBW in the horizontal plane has been elucidated by the analysis of the printed dipole antenna. As an antenna for the horizontal polarization, we consider a holed patch antenna to allow the passage of a Lecher wire for feeding the printed dipole. First, the FDTD method is used for analysis of the holed patch antenna placed on a finite ground plane, as shown in Fig. 2.33. The results are then compared with the experimental data.

Figure 2.34 shows the top view of the holed patch antenna. The values of lm and lh in Figs. 2.33 and 2.34 affect the matching condition of the holed patch antenna. Here, the values are fixed as $lm = 4$ mm (0.026 λ) and $lh = 12$ mm (0.08 λ). The dimensions of the cells are homogeneous at 1.0 mm in the x, y, and z directions, and the analysis domain is 178 × 178 × 40 cells. The return loss analyzed by the FDTD method with the above conditions and that obtained by measurement are shown in

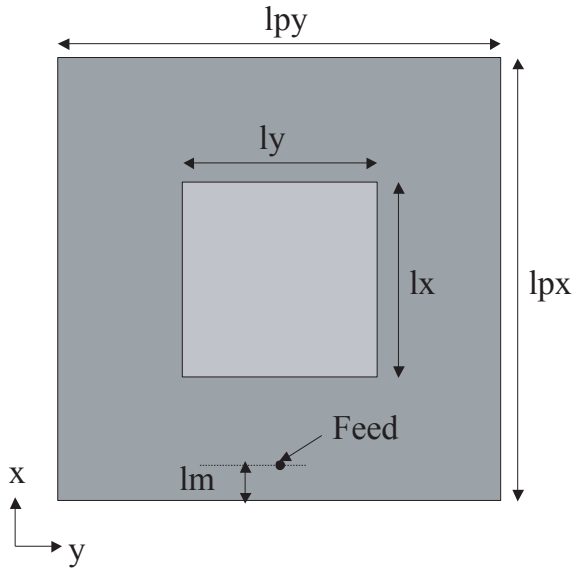

Figure 2.34: Top view of holed patch antenna (parameters lp, lh and lm)

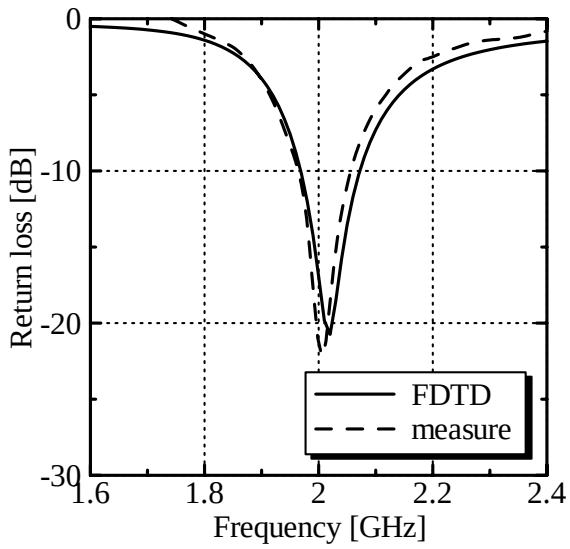

Figure 2.35: Return loss characteristics of holed patch antenna

Table 2.2: Design of holed patch antenna

Legth of hole edgelx, ly	Length of patch edgelpx, lpy
0.16λ	0.41λ
0.20λ	0.39λ
0.24λ	0.37λ
0.28λ	0.35λ

Fig. 2.35. The radiation patterns are given in Fig. 2.36. They are normalized to the maximum value of the co-polarization. The analytical and experimental results are in agreement. It can be observed from Fig. 2.36(a) that the HPBW in the E plane is 51°, and that the widening of the radiation pattern is required in order to attain a 60° beam. If magnetic currents are assumed at the patch edge, the radiation from the patch antenna can be considered as that from a two-element equal amplitude array whose element spacing is a resonant length of the lpx, as shown in Fig. 2.34. The beam width increases as the lpx decreases. In Ref. [38], the structure is bent in the E plane in order to reduce this magnetic current spacing. In our investigation, however, a hole shape that can reduce the magnetic current spacing lpx without folding or changing the resonant frequency is considered.

In the case of a holed patch antenna on a finite ground plane as shown in Fig. 2.37, in which the length of the ground plane in the horizontal direction is 1.1 λ and the length of the folded conductor along the edges of the ground plane is 0.2 λ, we varied the length of the hole in the x direction lx and that in the y direction ly and derived the return loss, which is shown in Fig. 2.38. The reason for the determination of the ground plane parameters will be described later. From Fig. 2.38, it is observed that the resonant frequency decreases as the hole size increases. This is because the current path around the hole becomes longer as the hole becomes larger. Next, as shown in Table 2.2, the lengths of the edges of the patch, lpx and lpy, are appropriately adjusted for each hole size. Figure 2.39 shows the HPBW in the horizontal plane as the hole size is varied in the re-design. The frequency is always 2 GHz when the radiation patterns in the horizontal plane are calculated. Figure

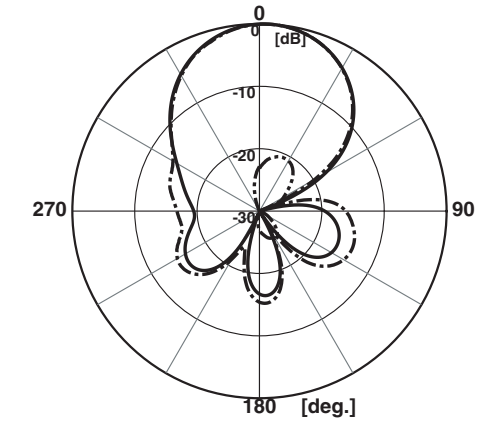

E_θ (FDTD) E_ϕ (FDTD)
E_θ (measure) E_ϕ (measure)

(a) E-plane

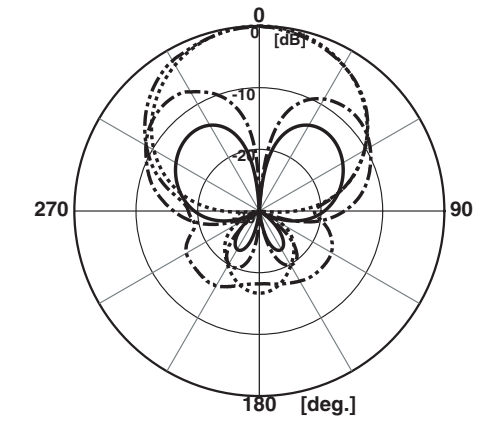

E_θ (FDTD) E_ϕ (FDTD)
E_θ (measure) E_ϕ (measure)

(b) H-plane

Figure 2.36: Radiation Pattern of holed patch antenna

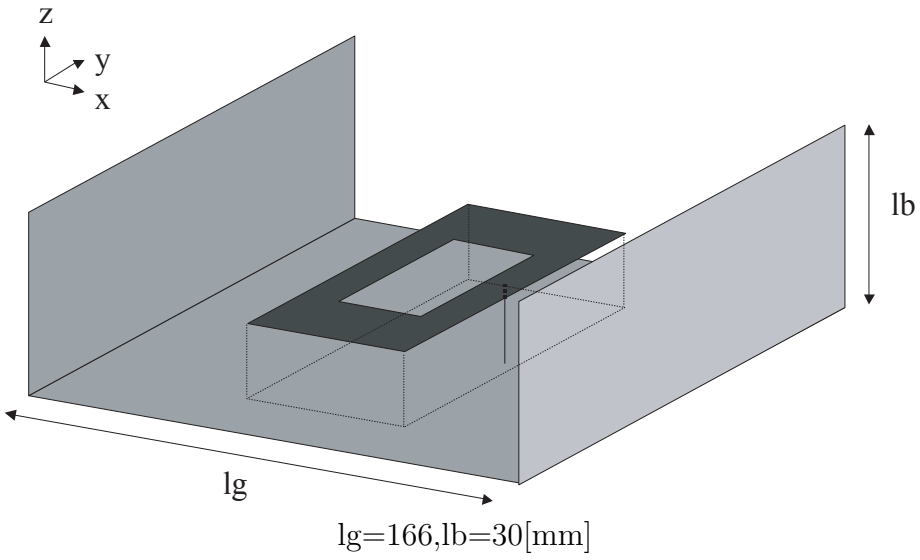

Figure 2.37: Analytic model for examination of horizontal beam width of holed patch antenna

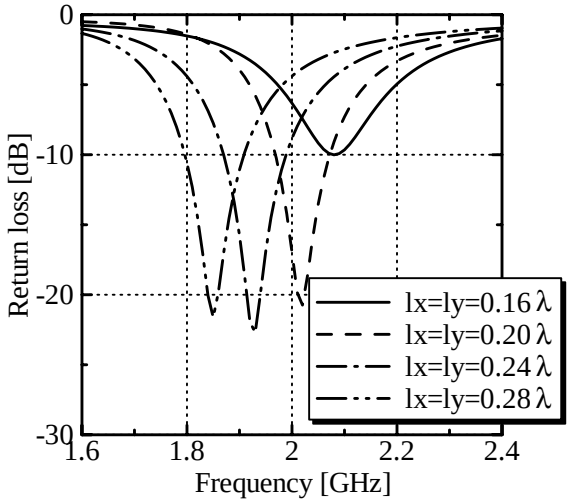

Figure 2.38: Return loss characteristics of holed patch antenna when parameter lx, ly is varied

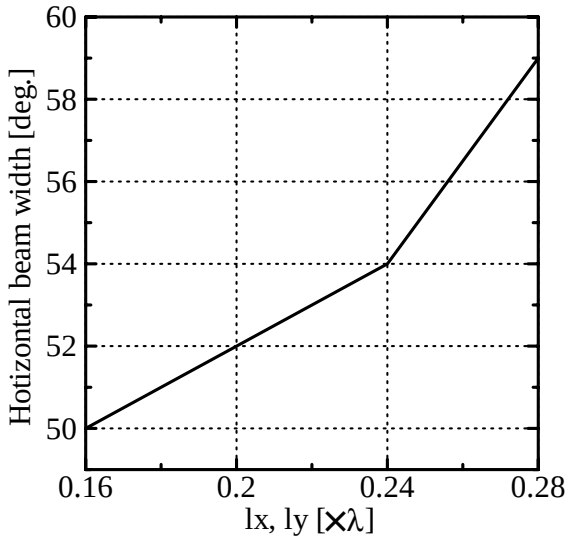

Figure 2.39: Horizontal beam width of holed patch antenna when patameter lx, ly is varied

2.39 shows that the HPBW in the horizontal plane is 59° if the length of the edges of the hole are $lx = ly = 0.28\ \lambda$. This analysis provides the relationship between the E-plane HPBW and the hole shape for a holed patch antenna and indicates that it is now possible to realize a beam of 60°.

It is important to note that the size of the hole cannot be increased beyond 0.28 λ due to the positional relationship of the feed for the patch. Furthermore, in comparison with the dipole, the controllable range of the beam width is narrower in the case of a holed patch. For the holed patch antenna, the beam becomes narrower for a larger reflector and becomes wider as the hole increases in size. Hence, the characteristics of the dipole, the beam width, and the structural parameters are in a trade-off relationship. Therefore, when designing the antenna, the effect of the characteristics of its elements must be taken into account. For instance, if the ground plate parameters (1.2 λ for the length of the ground plane in the horizontal direction and 0.2 λ for the conductor bent from the edge of the ground plane) for a 60° beam obtained from the study of the dipole are applied to the holed patch antenna, the beam widening region is exceeded, because the ground plane is too large.

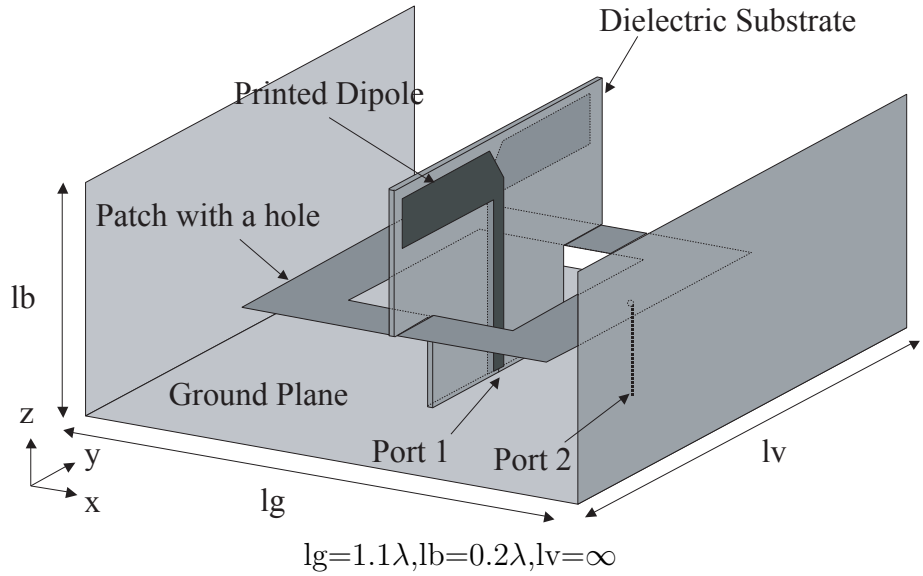

Figure 2.40: Bird's-Eye view of the polarization diversity antenna element

2.4 Hybrid Polarization Diversity Antenna

As a 2 GHz polarization diversity antenna, we consider the composite antenna shown in Fig. 2.40, using the ground plane parameters obtained for the HPBW in the horizontal plane of the printed dipole and the holed patch. First, let us consider a cellular phone base station antenna. Since the antenna forms an array, the FDTD analysis is truncated by absorbing boundaries, and the length lv of the ground plane along the y axis becomes infinite. To make the HPBW in the horizontal plane 60° in an application to base station antennas of 6-sector configuration, the ground plane length in the horizontal direction lg must be 1.1 λ, and the folded conductor length lb must be 0.2 λ, in addition to the points noted in the previous sections. Furthermore, for the fabrication process, the dielectric substrate has a convex shape in the ground plane direction, as shown in Fig. 2.40. Port 1 is the feed port for the printed dipole and Port 2 is the feed port for the holed patch. The cell size is homogeneous at 0.5 mm in the x, y, and z directions. The analysis domain is 358 × 144 × 88 cells.

In the composite antenna, it is important to reduce the mutual coupling between the elements so that each element can be used independently. For the proposed

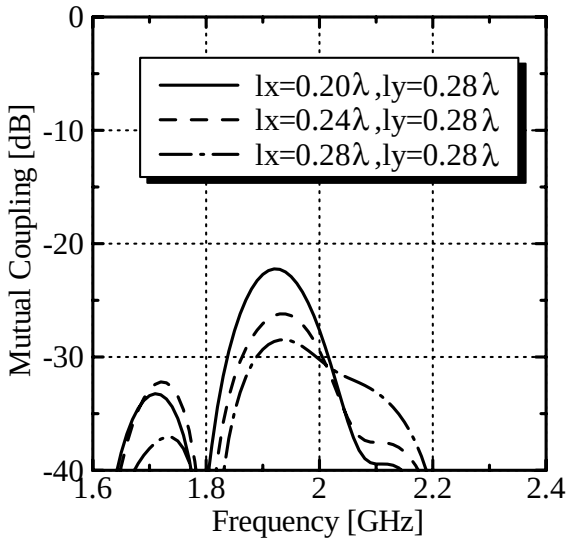

Figure 2.41: Mutual coupling characteristics when the parameter lx is varied

polarization diversity antenna, the mutual coupling between the printed dipole and the holed patch antenna is discussed. Regarding the self-diplexing antenna (which separates transmission and reception for satellite communication) that consists of a two-layer configuration of holed patch antennas, the hole shape is investigated as a parameter related to the mutual coupling [48]. When parameter $ly = 0.28\ \lambda$ in Fig. 2.37 is fixed and lx is varied, the mutual coupling between the elements is as shown in Fig. 2.41. From Fig. 2.41, it is clear that the mutual coupling between the elements at 2 GHz is -30.2 dB, and it is the lowest in the case of a square hole ($lx = ly = 0.28\ \lambda$) under the conditions selected. Furthermore, this coupling value indicates that each element can be operated independently.

Next, let us discuss the effect of the antenna height on the mutual coupling. The parameter representing the antenna height is ld for the printed dipole antenna as in Fig. 2.28, and lh for the holed patch antenna as in Fig. 2.33. It should be noted here that these parameters significantly affect the matching conditions of each element. Figures 2.42 and 2.43 show the return loss of each element when parameters ld and lh are varied. S11 represents the characteristics of the printed dipole, and S22 represents those of the holed patch. It can be observed in Fig. 2.42, that ld affects

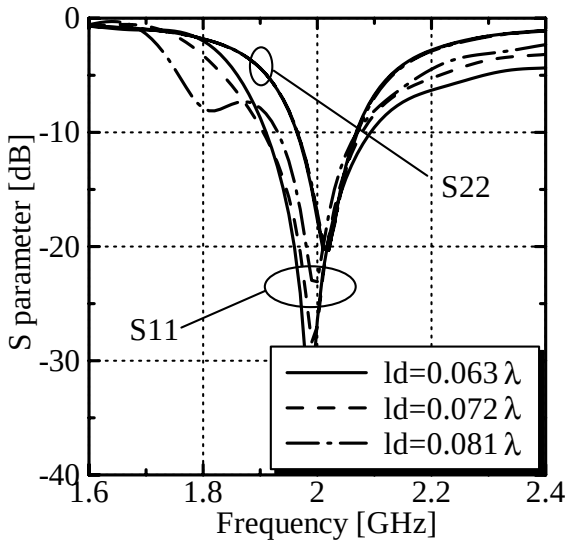

Figure 2.42: Return loss characteristics when the parameter ld is varied

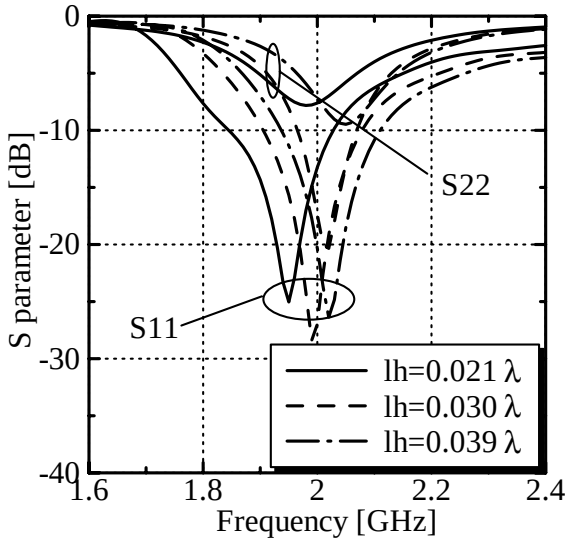

Figure 2.43: Return loss characteristics when the parameter lh is varied

Table 2.3: Final shape size of polarization diversity antenna

Dielectric substrate	ls	56
	ds	28.5
	ts	1
Dipole	lhd	26
	wd	6
	wl	3
	wt	14
	ld	24
Holed patch	lh	10
	lpx, lpy	58
	lx, ly	30
	lm	4
Reflector	lg	165
	lb	30
	lv	∞

only the resonant frequency of the printed dipole. Hence, it affects the matching conditions but not the characteristics of the holed patch antenna. On the other hand, it can be observed in Fig. 2.43 that lh significantly affects the matching conditions of both the printed dipole and the holed patch. In particular, in the case of a holed patch, there exists a relationship between the shape of the hole and the parameter lm expressing the feed position. Hence, the variations in lh have a few degrees of freedom for the matching condition. Furthermore, Figs. 2.44 and 2.45 show the mutual coupling when the parameters ld and lh are varied. It can be observed in Fig. 2.44 that the mutual coupling can be reduced if ld is increased. On the other hand, it can be observed in Fig. 2.45 that if lh is varied, there is an optimum value that minimizes the mutual coupling while the matching condition of the elements is still maintained. Here, the mutual coupling is -27.4 dB when $lh = 0.030\ \lambda$.

From the above discussions, the value of the S parameters analyzed by the FDTD method and measured at the design values are plotted in Fig. 2.46, and the radiation patterns in the horizontal plane are plotted in Fig. 2.47. The final shape dimensions of the elements and the reflector are shown in Table 2.3. The measured mutual coupling

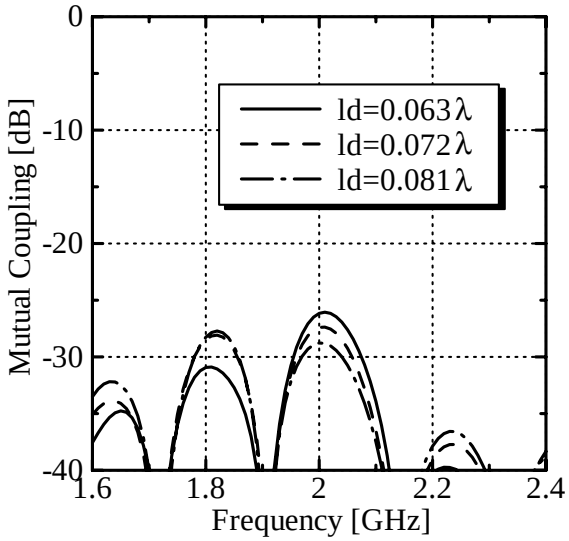

Figure 2.44: Mutual coupling characteristics when the parameter ld is varied

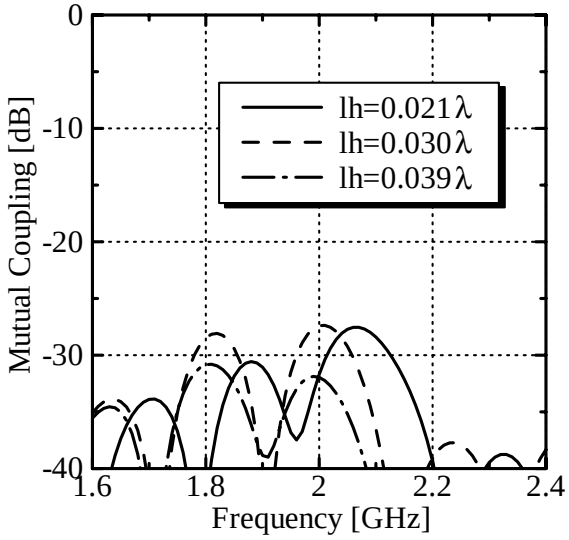

Figure 2.45: Mutual coupling characteristics when the parameter lh is varied

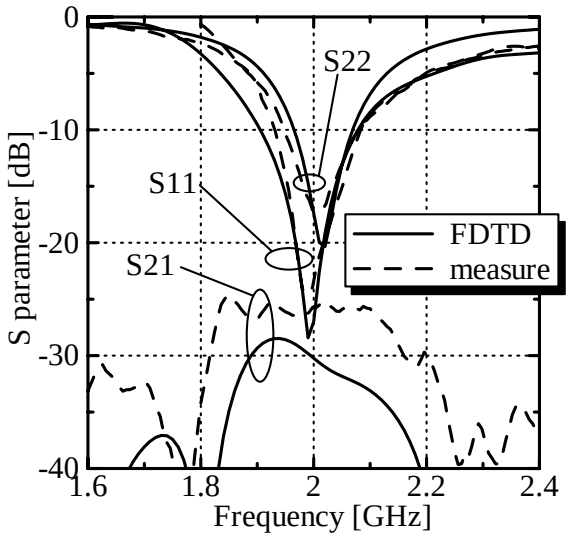

Figure 2.46: Return loss characteristics of the polarization diversity antenna

between the elements at the resonant frequency of 2 GHz is −25.7 dB. The HPBW in the horizontal plane is 62° and 56°, for the printed dipole and the holed patch, respectively. The deviation from the designed beam width is considered to be affected by the fact that the ground plane is finite in size in the vertical direction. Furthermore, the relative bandwidth at −10 dB is 9.0% and 5.4% for the printed dipole antenna and the holed patch, respectively. Thus, polarization diversity reception is possible with the present antenna on the uplink channel, and a vertical polarization can be transmitted from the printed dipole for the downlink.

2.5 Summary

This chapter presents the feed modeling, which particularly affects antenna characteristics. The iteration for the convergence when using a gap feed model with an internal resistance, can be decreased to 1/300 in comparison with that obtained the usual gap feed model. We clarified the importance of the CP modeling of the feed and short pins for a planar inverted-F antenna. When a feed pin is modeled by a

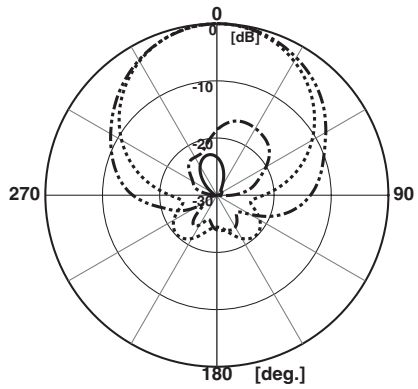

—— E_θ (FDTD) ····· E_ϕ (FDTD)

-·-·-· E_θ (measure) -··-··- E_ϕ (measure)

(a) Printed dipole antenna

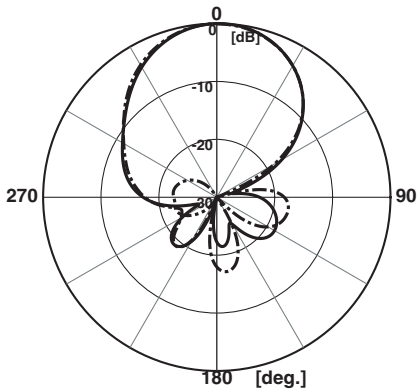

—— E_θ (FDTD) ····· E_ϕ (FDTD)

-·-·-· E_θ (measure) -··-··- E_ϕ (measure)

(b) Patch antenna with hole

Figure 2.47: Radiation pattern in horizontal plane of the polarization diversity antenna

square pillar and the radiuses of the short pins are considered by CP modeling, simulation results are in agreement with the experimental results. We also examined a modeling of the coaxial cable to feed a microstrip patch antenna and confirmed the accuracy improvement in comparison with the result obtained by a usual microstrip feed model.

This chapter analyzes the characteristics of the printed monopole antenna by the FDTD method, in order to provide the guiding principle for the numerical simulation. As a result of the parameter study, the minimum number of cells is 10 for the distance between the absorbing boundary and the antenna for any ground plane size. When we used very fine grids, no difference in the calculated results of the modeling of the taper shape was observed between the sub-cellular technique and the stair-stepped approximation. Moreover, the taper length changes the reactance component of the input impedance of the printed monopole antenna.

For the introduction of the IMT-2000 system, a 60° beam polarization diversity antenna at 2 GHz was designed. With regard to the printed dipole antenna used for the vertical polarization, the relationship between the ground plane shape and the HPBW in the horizontal plane was studied. In the calculation of the radiation pattern by the FDTD method, it was demonstrated that a finite-size ground plane must be considered. The ground plane parameters for the realization of a 60° beam were determined. With regard to the holed patch antenna used for horizontal polarization, it was found that the beam width is increased by changing the hole shape. Furthermore, a polarization diversity antenna consisting of a printed dipole and a holed patch was proposed. The relationship between the hole shape of the patch antenna and the mutual coupling between the elements was studied. A mutual coupling of -25.7 dB between the antennas and a beam width of 60° in the horizontal plane were realized.

Chapter 3

Mutual Coupling between the Transmitting and Receiving Antennas with a Choke

3.1 Introduction

In this chapter, we examine the antenna structure for a repeater. The antenna constructed is a patch array antenna of 4 elements. At the edge of the ground plane is a choke structure, and the parameters of this structure affect the front to back (FB) ratio [108]. We have also designed the optimum parameters of the element using electromagnetic analysis. Furthermore, we show the relationship between the mutual coupling and the distance between the elements when the antennas are arranged back-to-back. A high FB ratio is required to control mutual coupling. We also discuss the antenna structure of a 4-port feed type and the coupling of a beam tilted antenna and confirm that the mutual coupling is changed by the front to side (FS) ratio of the element. The calculated results are compared with the experimental results. Next, we investigate a 16-element patch array antenna, which refers to the 4-element design method. The suppression of the FB ratio by a choke is small in the case of the 16-element array, because its side lobe level (SLL) is large. We examine the effect of restraining the mutual coupling using binomial, Chebyshev, and Taylor

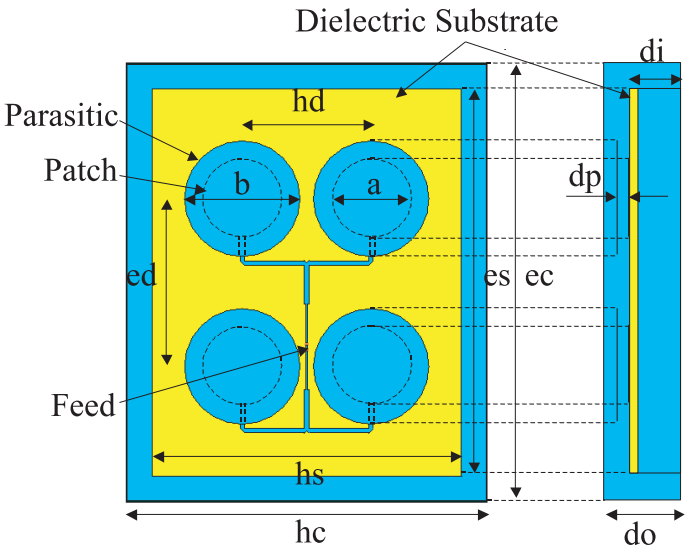

a=0.31λ,b=0.45λ,hd=0.5λ,ed=0.65λ,hs=1.2λ,es=1.5λ,
hc=1.4λ,ec=1.7λ,dp=0.05λ

Figure 3.1: Structure of circular patch array antenna

arrays by controlling the amplitude of each element.

3.2 4 Element Patch Array Antenna

3.2.1 Choke-Loaded Patch Array Antenna

Figure 3.1 shows the element structure of a circular patch array antenna. This antenna has a choke structure of length *di* in the rear direction from the end of the dielectric substrate, with a dielectric constant of 3.5 and a thickness of 1.2 mm. The impedance matching is performed by use of a lumped element circuit connected to the feed point, and it is composed of one series inductor (L = 1 nH) and one parallel capacitor (C = 0.6 pF). λ is the free-space wavelength at 2 GHz, and *dp* is the height of the parasitic element. CST Microwave Studio is used for the electromagnetic analysis, and the structure parameters are optimized. Figure 3.2 shows the FB ratio characteristics, when the lengths *di* and *do* of the choke walls are varied. The FB ratio reaches the

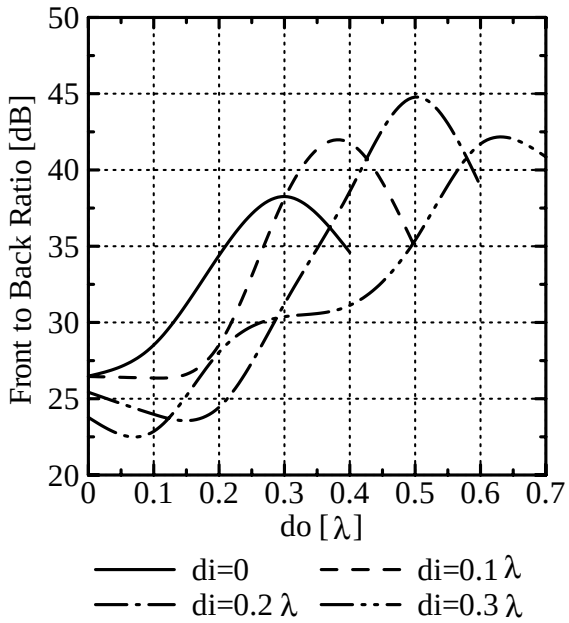

Figure 3.2: Front to back ratio characteristics, when the length *di* and *do* of the wall in choke are varied.

maximum value of 45 dB at approximately $di = 0.2\ \lambda$ and $do = 0.5\ \lambda$. Figures 3.3 and 3.4 show the return loss and radiation pattern characteristics when $di = 0.2\ \lambda$ and $do = 0.5\ \lambda$ as shown in Fig. 3.1. The bandwidth of a return loss less than -10 dB is 20.3% (1.85–2.27 GHz), and the directional gain at 2 GHz is 12.3 dBi.

Figure 3.5 shows the structure of the repeater system using the same antenna elements arranged back-to-back. In actuality, this repeater system will be used as a booster, and the space between the elements will be filled using an RF circuit block. However, the effect of this block is not examined in this chapter. Figure 3.6 shows the mutual coupling characteristics when the interval *ed* is varied. The value of the mutual coupling is plotted at the highest value of the bandwidth (1.92–2.17 GHz), and the parameters of the choke ($di = 0.2\ \lambda$ and $do = 0.5\ \lambda$) are fixed. When an element interval becomes large, mutual coupling is controlled at -99.1 dB in the case wherein $ed = 4\ \lambda$. Furthermore, we discuss the relationship between the FB ratio of the element and the mutual coupling, as shown in Fig. 3.7. The parameters of the

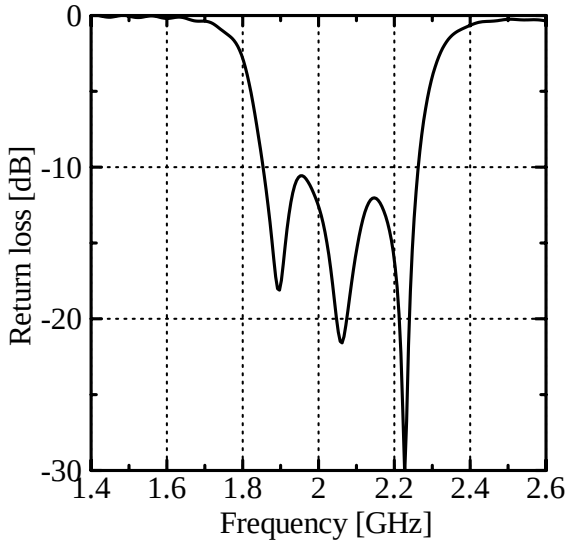

Figure 3.3: Return loss characteristics (di=0.2λ, do=0.5λ)

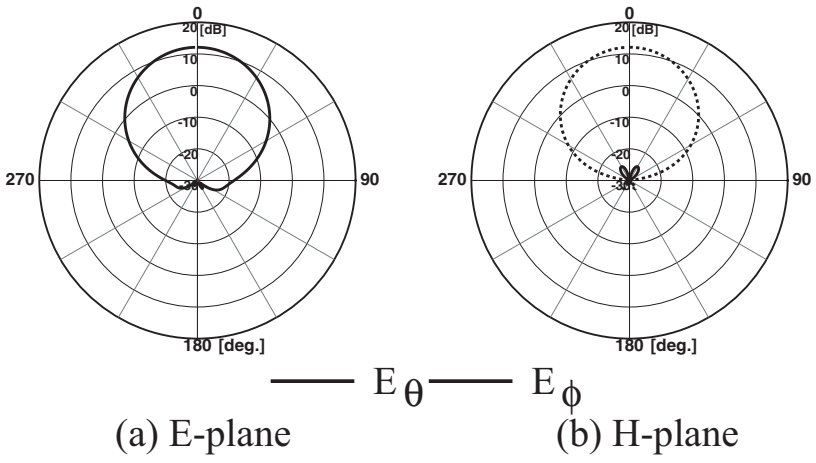

Figure 3.4: Radiation pattern characteristics (di=0.2λ, do=0.5λ).

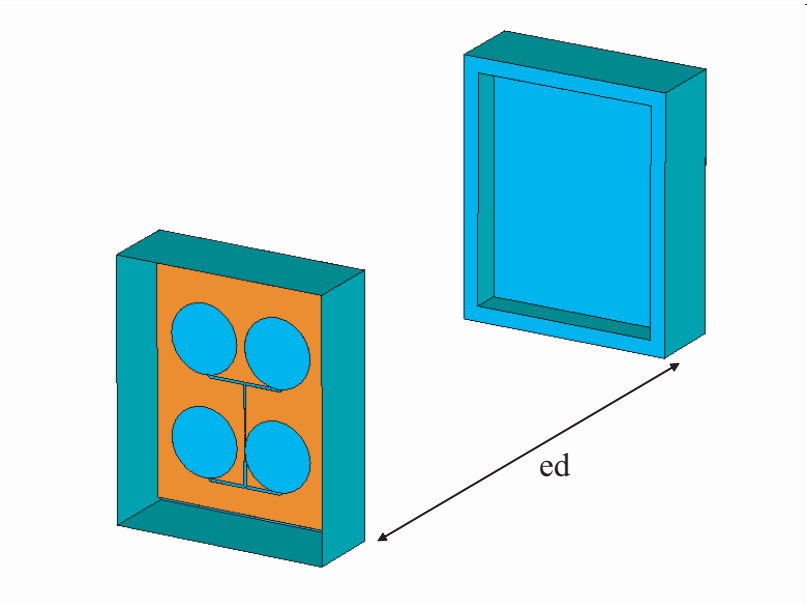

Figure 3.5: Structure of repeater system using identical antenna elements arranged back to back.

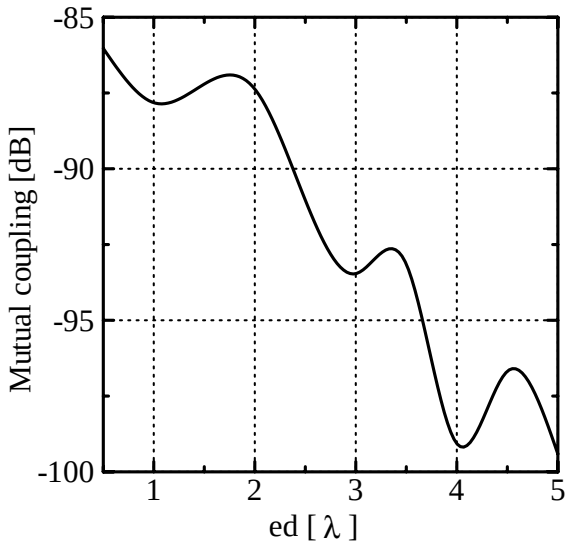

Figure 3.6: Mutual coupling characteristics, when *ed* is varied (di=0.2λ, do=0.5λ fixed).

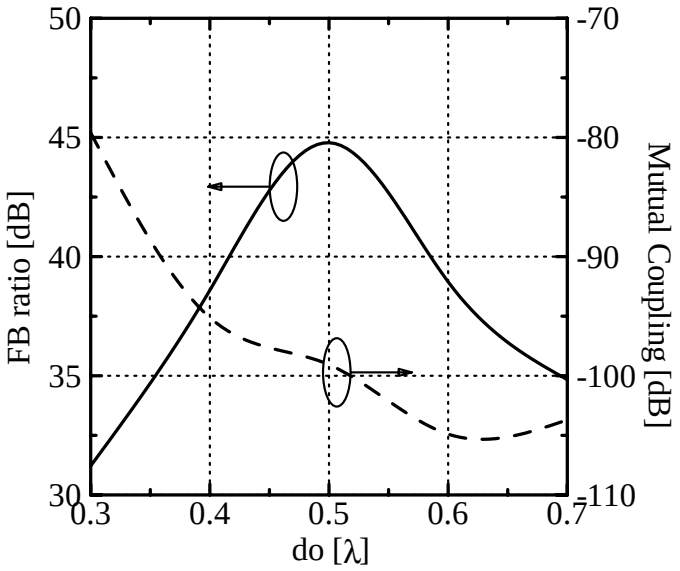

Figure 3.7: FB ratio and mutual coupling characteristics, when *do* is varied (di=0.2λ, ed=4λ fixed).

choke are also fixed, and the length *do* of the outer side of the choke is varied. When the parameter *do* is taken as approximately 0.52 λ, the mutual coupling decreases to less than -100 dB. However, the maximum value of the FB ratio increases to 44.8 dB at $do = 0.5\ \lambda$.

3.2.2 Beam-Tilted Patch Array Antenna

Figure 3.8 shows the structure of the repeater using 4-element patch array antennas. Figure 3.8 (a) shows the 4-port method that is used to feed each antenna element. Figure 3.8 (b) shows a 1-port feed type, which is the fed in-phase in each antenna, and is of the same structure as that shown in Fig. 3.1. In this section, we examine the mutual coupling when a phase difference is applied to the 4 ports and results in a tilted main beam. We also examine the case of the repeater arranged at an angle of 90° (1-port feed type).

The method of computing mutual coupling between the 4-port feed types is as follows: First, this antenna feeds the feed ports of points #1–#4 of Fig. 3.8 (a),

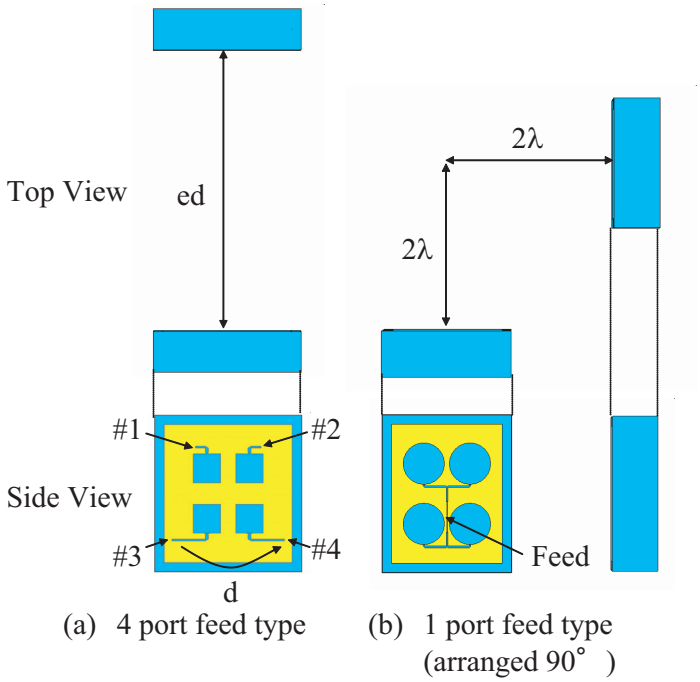

Figure 3.8: Repeater structures using two methods of patch array antenna excitation.

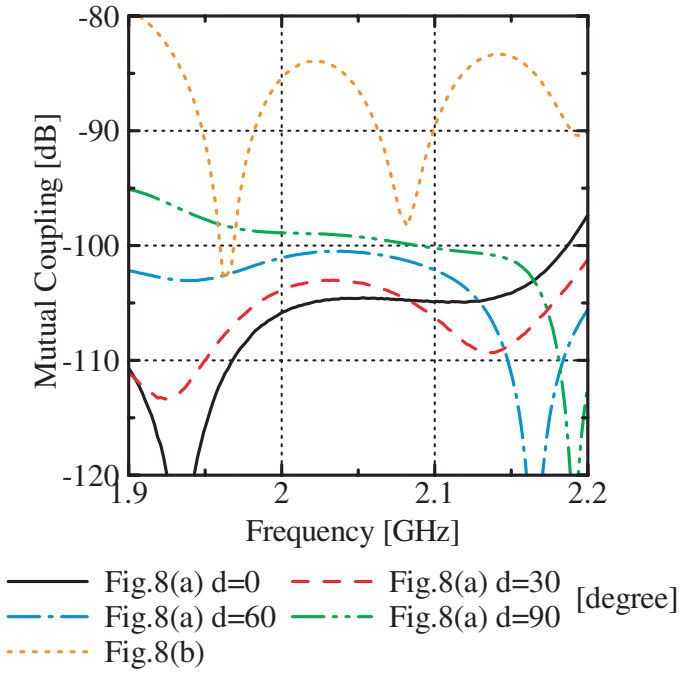

Figure 3.9: Mutual coupling characteristics in of the two feed types in Fig. 8 ($ed = 4\lambda$ fixed).

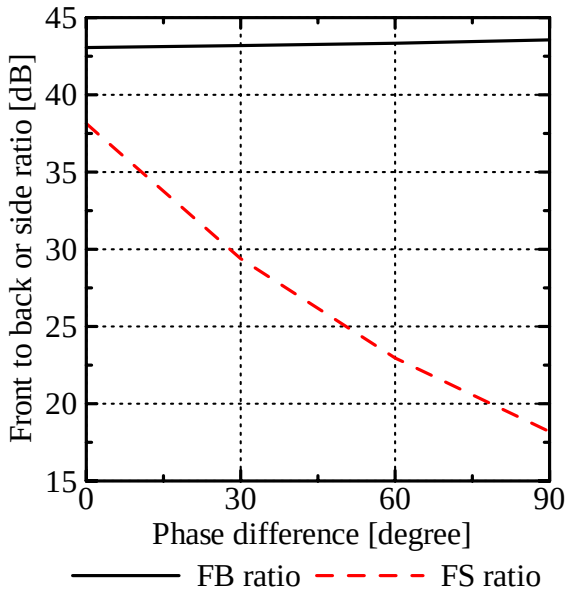

Figure 3.10: Front to back or side ratio (*back* means highest value in range of ± 30° from 180° back of main beam, and *side* means ± 90°).

and we obtain the S matrix of each port. CST Microwave Studio is also used for the electromagnetic analysis. Next, the mutual coupling is computed from the S matrix, which shows the transmitting and receiving circuit. The transmitting and receiving circuit is the T-branch circuit that feeds points #2 and #4 with the phase difference d toward points #1 and #3. Figure 3.9 shows the mutual coupling characteristics when the phase difference d is varied. When $d = 90°$, the mutual coupling increases to 6 dB as compared with a no-phase difference, and it increases to 20 dB when the arrangement is as shown in Fig. 3.8 (b). Figure 3.10 shows the FB and FS ratios of the antenna element when the phase difference d is varied. The main beam is tilted ± 16° when d is ± 90°. An FB ratio is plotted at the highest values in the range of ± 30° from 180° back of the main beam, and the FS ratio is plotted in the range of ± 90°. The FS ratio changes greatly though the FB ratio is fixed when a phase difference is added between the elements, as shown in Fig. 3.10. Therefore, the increase in mutual coupling is believe to be the effect of the FS ratio of the element.

We manufactured the repeater using two sets of 4-element patch array antennas

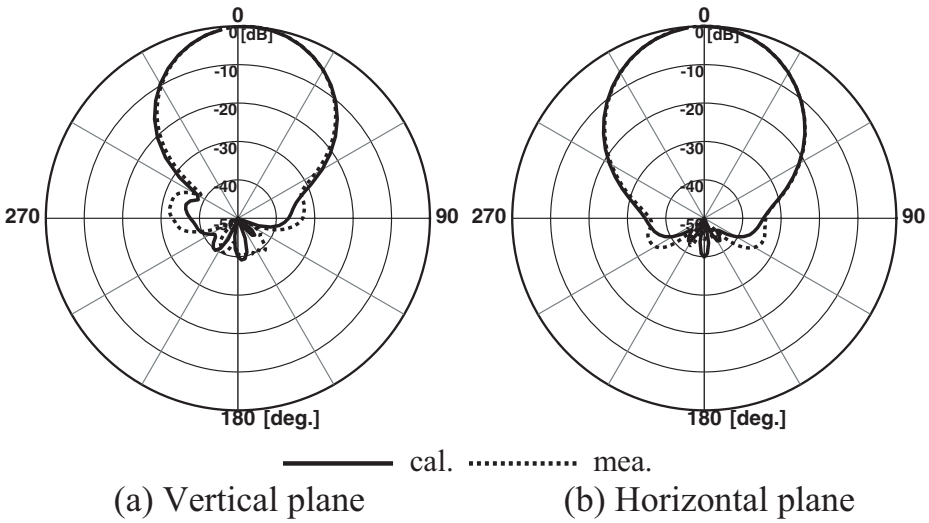

Figure 3.11: Radiation pattern characteristics in comparison with calculation and measurement of Fig. 8 (a) (calculation frequency is 1.92GHz).

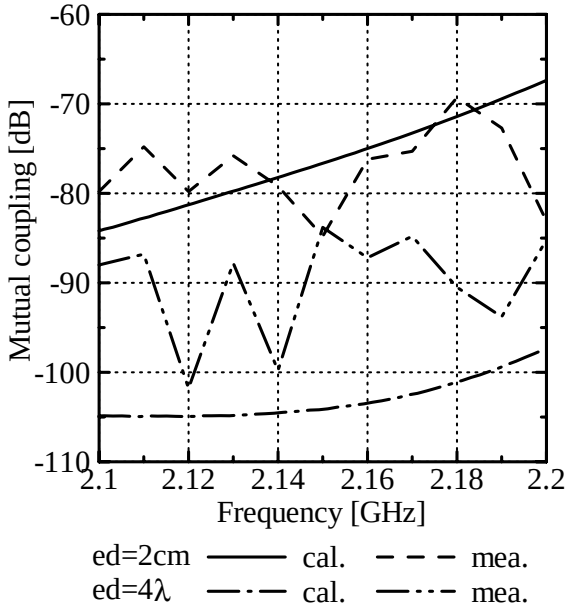

Figure 3.12: Mutual coupling characteristics in comparison with calculation and measurement.

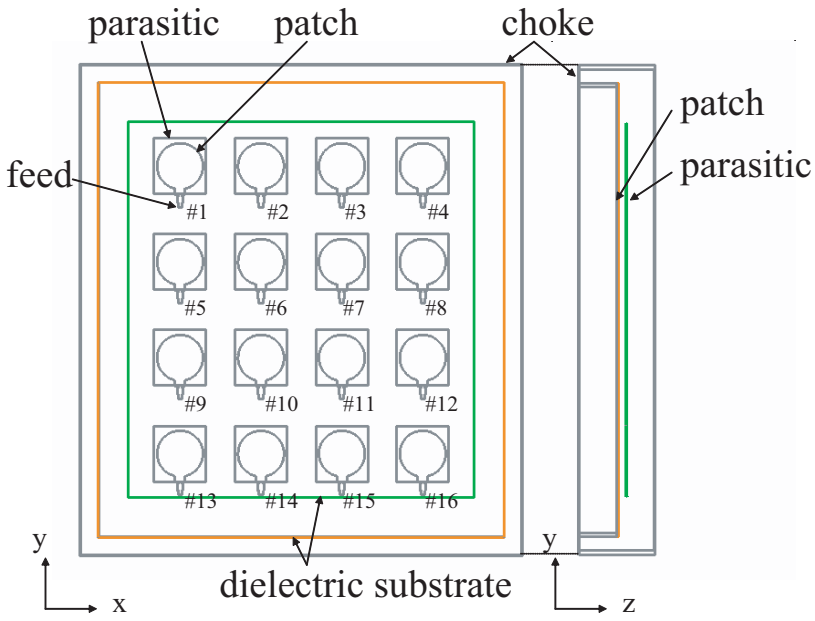

Figure 3.13: Structure of 16 element patch array antenna with choke

in this experiment. The input power from the signal generator to one of the patch array antennas was 0 dBm. A measuring receiver was connected to the other antenna, and the field intensity was measured. The frequency range was 2.1–2.2 GHz. Figure 3.11 and 3.12 show the radiation pattern characteristics and mutual coupling of the measurement result. With regard to the radiation pattern, the analytical results were in agreement with the measurements. The analytical results were in agreement with the tendency of the measured results when the interval of the elements was 2 cm, as shown in Fig. 3.12. However, the accuracy of the measurement of the mutual coupling was low in the case of $ed = 4\ \lambda$.

3.3 16 Element Patch Array Antenna

3.3.1 Binomial Array

Figure 3.13 shows the 16-element patch array antenna with a choke. The parameters of the dielectric substrate are as follows: The substrate used for the patch antenna has

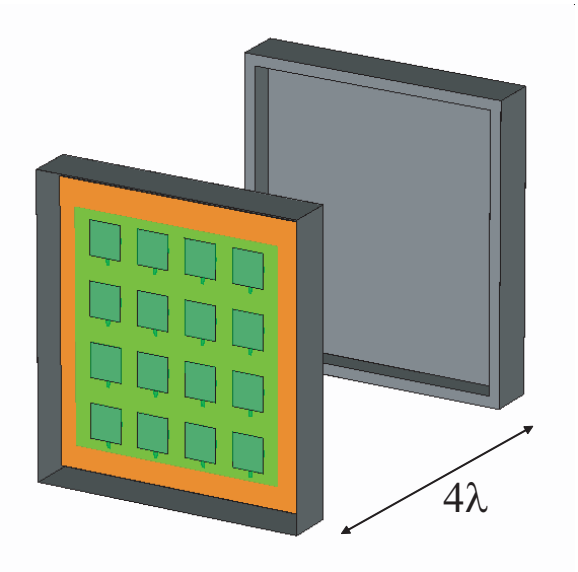

Figure 3.14: Repeater system consisting of two pairs of patch array antennas

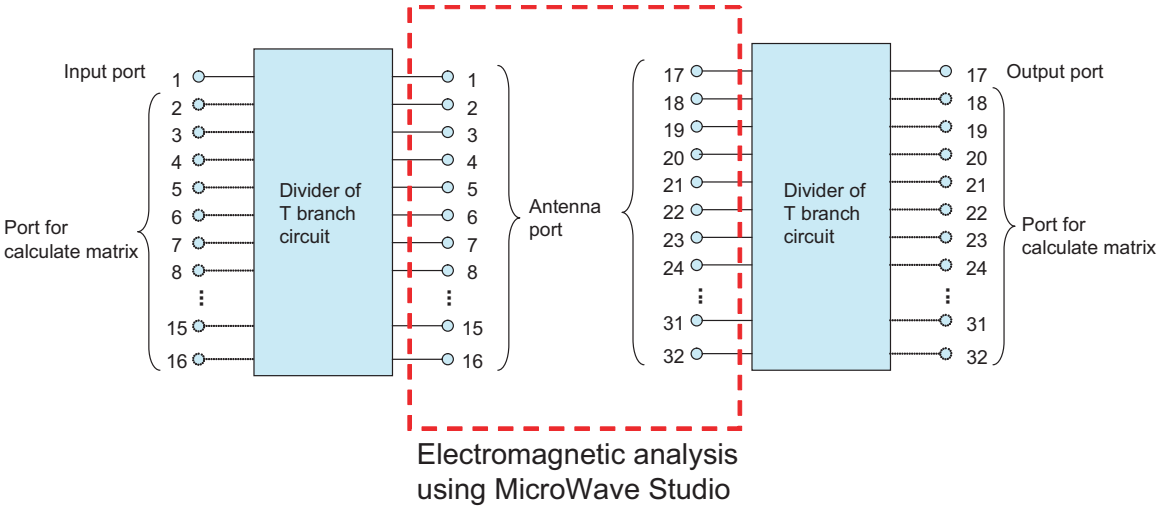

Figure 3.15: Analytic method for mutual coupling characteristics

a dielectric constant of 3.3, a dielectric dissipation factor of 0.0040, and a thickness of 1.6 mm. The substrate used for the parasitic element has a dielectric constant of 3.88, a dielectric dissipation factor of 0.016, and a thickness of 1.0 mm. The diameter of each patch is 45.2 mm, and the antenna is connected with a microstrip stepped impedance transformer for matching at the required band (1.92–2.17 GHz). The size of the parasitic elements is 51 $\times$ 54.5 mm and the height from the patch is 7 mm. When this antenna is fed uniformly and in phase in each element, the radiation gain at 2 GHz is 19.0 dBi, and the FB ratio is 38.3 dB. Further, the mutual coupling is -83.6 dB when the interval between the elements of the two sets becomes 4 λ, as shown in Fig. 3.14. CST Microwave Studio is used for the electromagnetic analysis. Figure 3.15 shows the analytical method for the mutual coupling characteristics. The input and output ports are connected with each port of the antenna using a T-branch divider circuit.

The choke structure greatly affects the suppression of an FB ratio in the case of a 2 $\times$ 2 element array. However, the suppression of the FB ratio by the choke is small at 7.1 dB in the case of a 16-element array, because the FB ratio of only the reflector is 31.2 dB. We examined the effect of restraining the mutual coupling using a binomial pattern by controlling the amplitude of each element. The binomial pattern can be achieved when points #6, #7, #10, and #11 are fed with an amplitude of 1.0; that fed to points #2, #3, #5, #8, #9, #12, #14, and #15 is 0.333; and that fed to points #1, #4, #13, and #16 is 0.111. Figure 3.16 shows the radiation pattern of the E plane when the amplitude is controlled near the E and H planes. The binomial pattern causes a decrease in the SLL of 17.5 dB as well as a deterioration in the directional gain of 1.5 dB. Figure 3.17 shows the mutual coupling characteristics when the interval of the elements becomes 4 λ, and it also shows that the side lobe control of the E plane is more effective in the suppression of coupling than the H plane. Mutual coupling between the elements becomes -104.9 dB by when a binomial pattern in the E and H planes is used.

Figure 3.18 shows the S21 characteristics when the element interval d of the prototype antennas based on the design of the binomial array is varied. The Agilent PNA E8363B vector network analyzer is used for the measurement, and the system

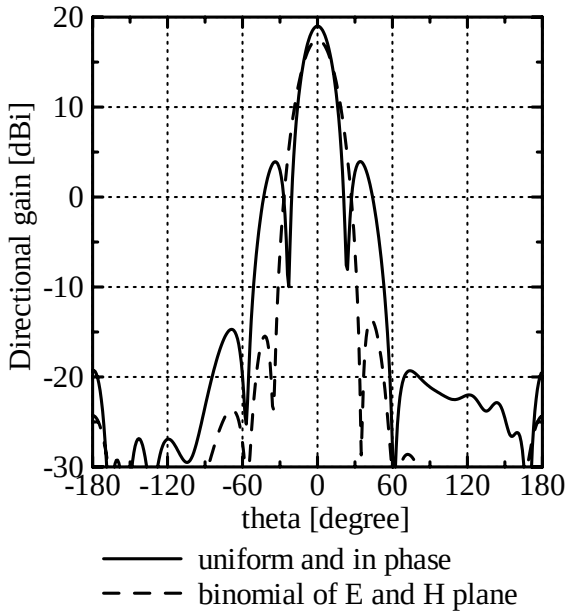

Figure 3.16: Radiation pattern of E plane in the case of uniform and binomial patterns

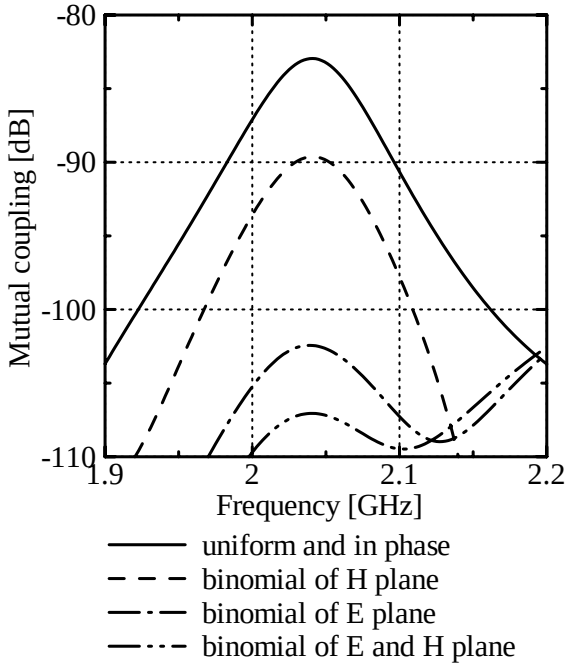

Figure 3.17: Mutual coupling characteristics in the case of uniform and binomial patterns

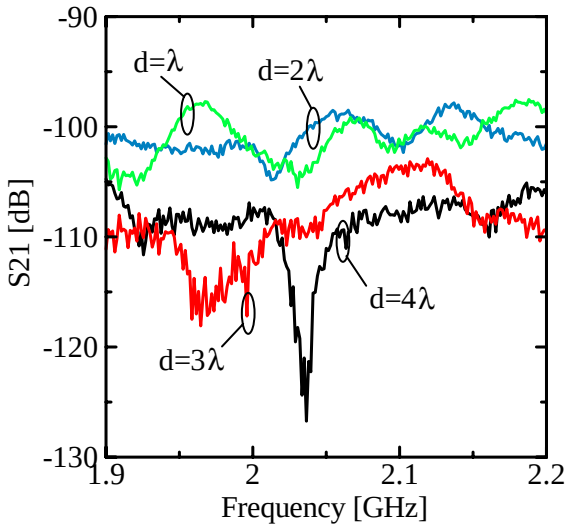

Figure 3.18: Measured mutual coupling characteristics of binomial arrays when d is varied.

dynamic ranges are 119 dB (500 MHz to 2 GHz) and 122 dB (2 to 10 GHz) under the condition of the 10 Hz IF bandwidth. The maximum value of the mutual coupling in the range of 1.92 to 2.17 GHz is -106.3 dB in the case of $d = 4\ \lambda$.

3.3.2 Chebyshev and Taylor Arrays

The Chebyshev pattern can be achieved by matching the amplitude corresponding to the coefficient of a third-degree Chebyshev polynomial after determination of the SLL. For example, when the SLL is determined to be 25 dB, points #6, #7, #10, and #11 are fed with an amplitude of 1.0; that fed to points #2, #3, #5, #8, #9, #12, #14, and #15 is 0.483; and that fed to points #1, #4, #13, and #16 are 0.233. Figure 3.19 shows the radiation pattern of the E plane when the amplitude is controlled about the E and H planes. The used of the Chebyshev pattern causes a decrease in the SLL of 19.1 dB and also a deterioration in the directional gain of 1.6 dB. Figure 3.20 shows the mutual coupling characteristics when the interval of the elements becomes 4 λ. When the SLL is 25 dB and there is a change in it, the mutual coupling decreases, and becomes -100.1 dB.

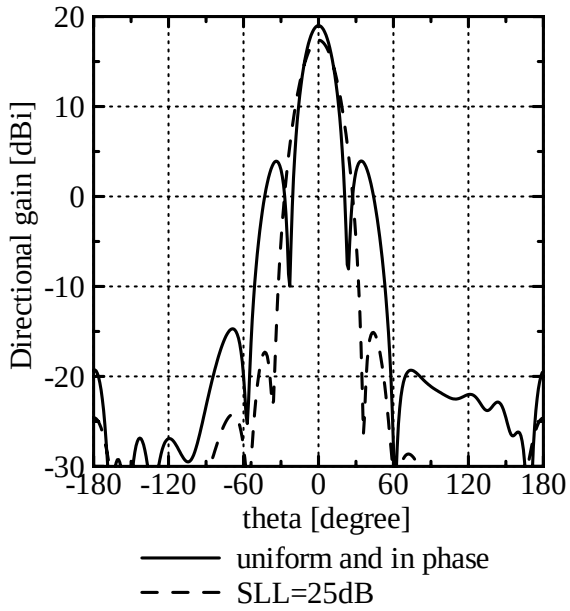

Figure 3.19: Radiation pattern of E plane in the case of uniform and chebyshev patterns

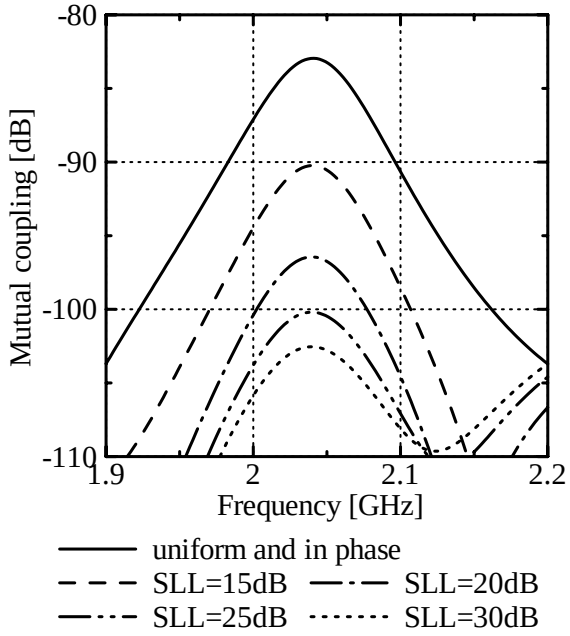

Figure 3.20: Mutual coupling characteristics in the case of uniform and chebyshev patterns

The Taylor pattern can be also achieved by matching the amplitude. Figure 3.21 shows the radiation pattern of the E plane when the amplitude is controlled about the E and H planes. The use of the Taylor pattern causes a decrease in the SLL of 21.1 dB and also a deterioration in the directional gain of 1.7 dB. Figure 3.22 shows the mutual coupling characteristics when the interval of the elements becomes 4 λ. The mutual coupling becomes -101.1 dB when the SLL is 25 dB.

3.4 Summary

This chapter presented the mutual coupling characteristics of 4-element patch array antennas with chokes used for repeater systems. The choke structures affect the FB ratio, and the mutual coupling is less than -100 dB when suitable parameters are chosen. The mutual coupling is 6 dB higher than in the case without the phase difference, because the SLL of the beam-tilted antenna is high. We have also presented the mutual coupling characteristics of 16-element patch array antennas with chokes that are used for repeater systems. The binomial, Chebyshev and Taylor arrays affect the restraint of the SLL, and the mutual coupling is less than -100 dB when suitable parameters are chosen.

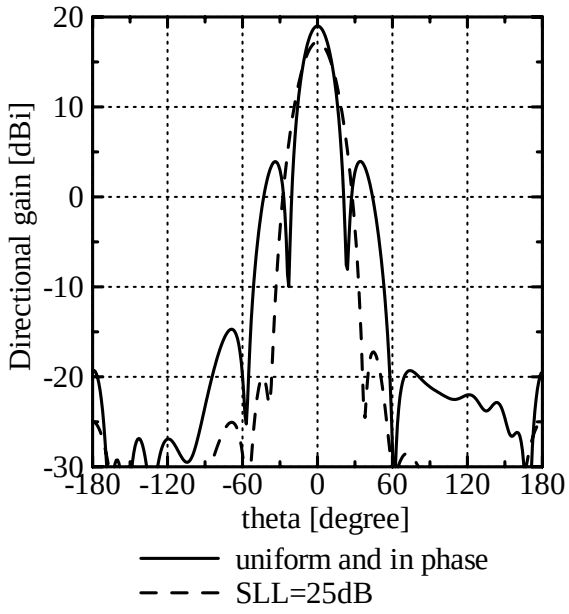

Figure 3.21: Radiation pattern of E plane in case of uniform and taylor pattern

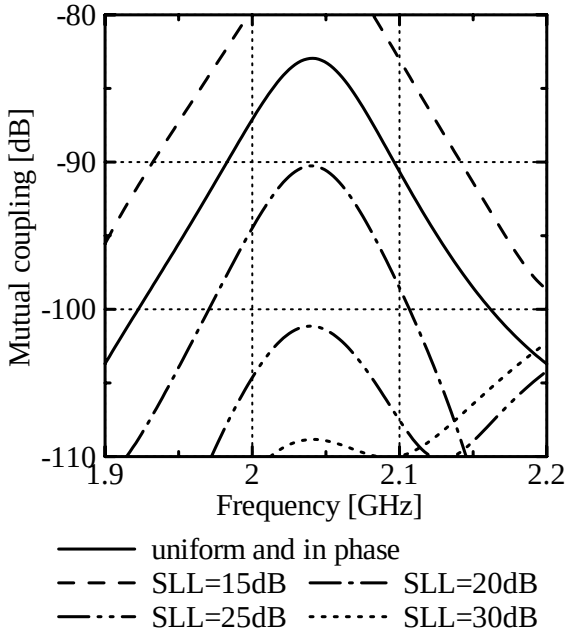

Figure 3.22: Mutual coupling characteristics in case of uniform and taylor pattern

Chapter 4

Modeling of Balun to Feed a Dual Frequency Antenna

4.1 Introduction

In this chapter, the operating principle of a balun used to feed a printed dipole antenna, which is used for a base station in mobile communications, is analyzed by the FDTD method. The characteristics of the open and short stubs comprising the balun are computed using an equivalent circuit connected to the dipole. It is shown that frequency co-use is possible with a printed dipole antenna integrated with a balun. The relationship between the structural parameters of the balun and the two resonant frequencies is also shown. A built-in balun printed dipole antenna with a reflector is discussed whether to function as a balun at the different frequency.

4.2 Balun Characteristics

Figure 4.1 shows the structure of the dipole antenna printed on a substrate. The dielectric substrate has a relative permittivity of 3.5 and a thickness of 1.2 mm. The wavelength λ used for the structural parameters is the free space wavelength at 900 MHz. The parameters necessary for the FDTD analysis are a cell size of 0.75 mm in the x and y directions and 0.3 mm in the z direction. The meshes are uniform.

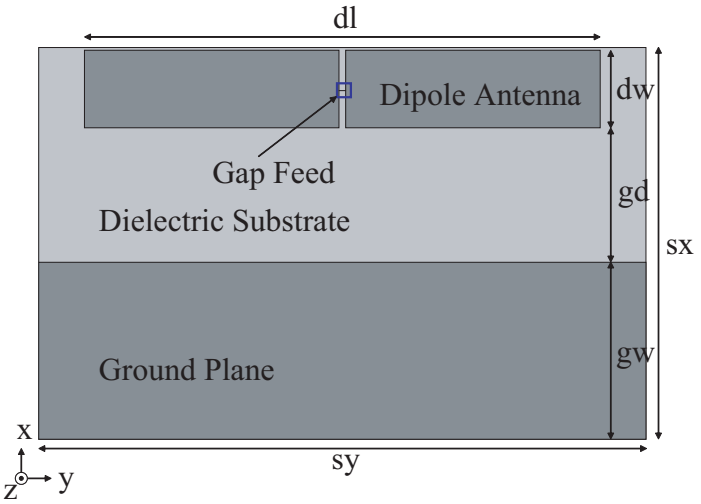

sx=0.329λ, sy=0.45λ, dl=0.383λ, dw=0.065λ, gd=0.113λ , gw=0.149λ

Figure 4.1: Structure of printed dipole antenna

The number of time steps is 18,000, which is equal to the number of time steps with a feed current amplitude of 10^{-5}. In order to accelerate the convergence of this feed current, a 50 Ω internal resistor is provided in the feed section. An 8-layer PML is used as the absorbing boundary.

The input impedance characteristics of the ground plane printed on the same substrate shown in Fig. 4.1 (d + g) and of the dipole only (d) are compared in Fig. 4.2. In the 800–900 MHz range, the input resistance when the ground plane is attached tends to become smaller than that in the case of a dipole alone. In addition, the input reactance becomes more inductive. The bandwidth at 900 MHz decreases due to the ground plane. These results agree with those obtained by an analysis based on the method of moments [62]. Furthermore, techniques such as the placement of parasitic elements are needed to widen the bandwidth.

When the dipole antenna is fed by a coaxial cable, a balun is needed for a balanced-to-unbalanced conversion. A printed dipole antenna with an integrated balun is shown in Fig. 4.3. Several types of baluns are available, including the quarter-wave sleeve (bazooka) balun, the balun using a half-wave circumference line, and the divided coaxial balun. A branch conductor balun is used to feed a printed dipole [72]–[74].

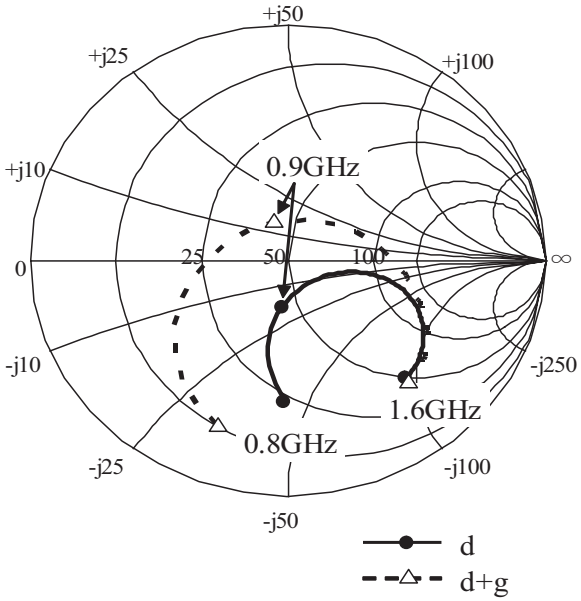

Figure 4.2: Input impedance characteristics

Its structure is shown in Fig. 4.4(a). When the lengths of the open and short sections of the branch conductor are 1/4 that of the wavelength at the operating frequency, the structure is operated as though the load is directly connected to the coaxial line. The equivalent circuit of the balun using a branch conductor is shown in Fig. 4.4(b). Here, Z_o, Z_s and Z_L are the characteristic impedances of the open stub, short stub, and load (dipole). The impedance looking into the load side from the coaxial line side is $Z_{in} = Z_L$ if $Z_o = 0$ and Z_s is infinite.

Figure 4.5 shows models of the open (o) and shorted (s) sections of the branch conductor shown in Fig. 4.4 printed on the substrate. The stub lengths in Fig. 4.5 are $lo = 0.146\ \lambda$ and $sh = 0.144\ \lambda$. The back of the substrate for the open stub is an infinite ground plane, and there is no ground plane on the back of the short stub. Figure 4.6 shows the input impedance at the observation point, indicated by □. It is evident that when the frequency is 900 MHz, the input impedance is 0 at the open stub and nearly infinite at the short stub. As the frequency increases, the reactance for the open stub increases and that for the short stub decreases.

A printed dipole with a short stub is shown in Fig. 4.7. Here, a short stub is

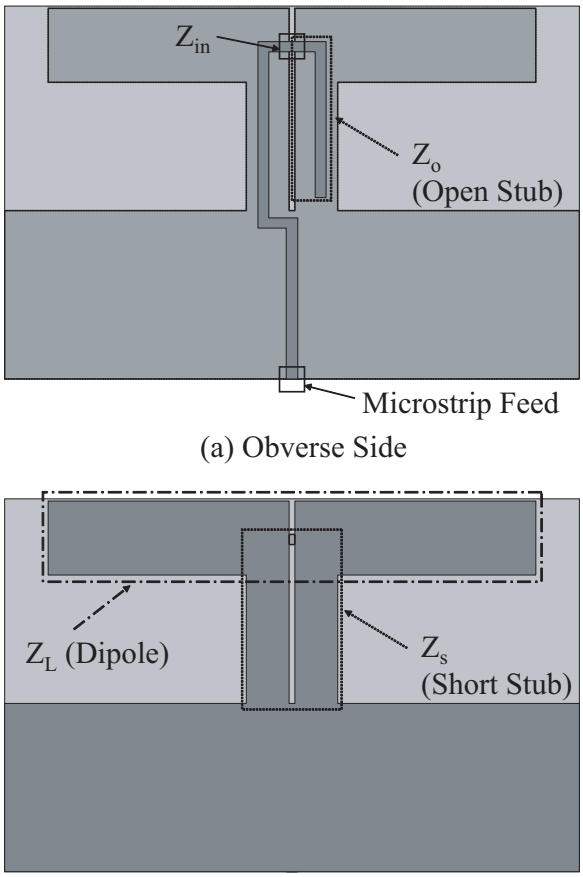

Figure 4.3: Built-in balun printed dipole antenna

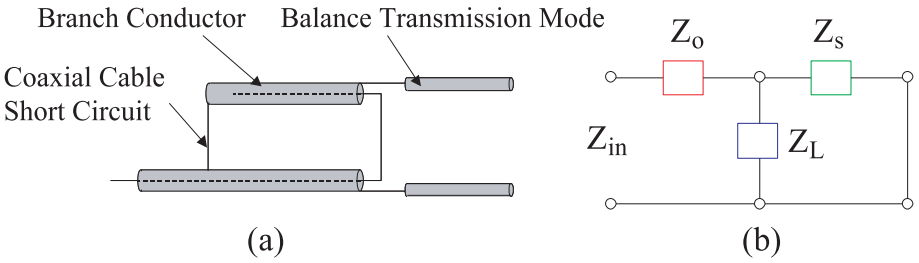

Figure 4.4: Balun by branch conductor and equivalent circuit

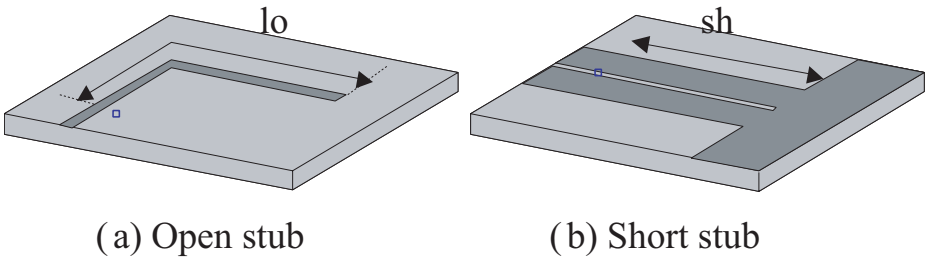

Figure 4.5: Open-circuit stub and short-circuit stub

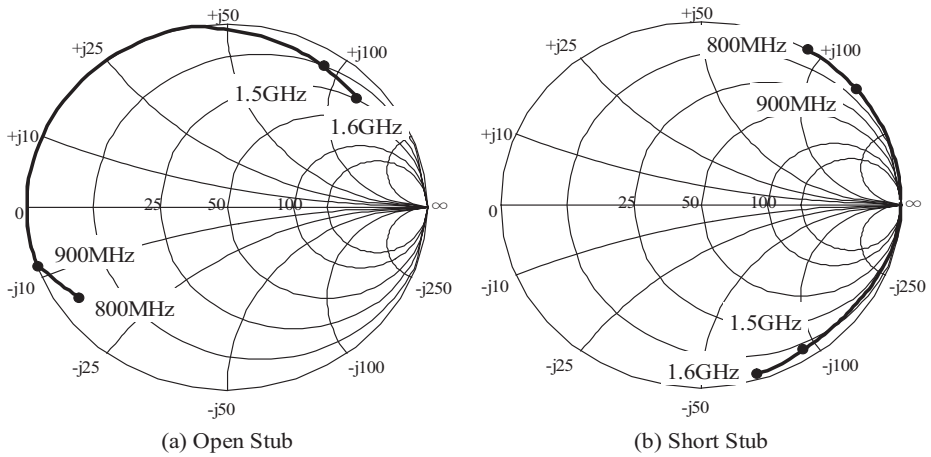

Figure 4.6: Input impedance characteristics of open-circuit stub and short-circuit stub

connected in parallel with the dipole. The input impedance characteristic is shown in Fig. 4.8. It is found that the impedance at 1.5 GHz does not change, while the input resistance tends to increase at 800–900 MHz. Let us discuss the characteristics of the printed dipole with a short stub. If the characteristics of the short stub shown in Fig. 4.6(b) are simply connected in parallel with the dipole, such characteristics cannot be obtained. Furthermore, in the structure shown in Fig. 4.7, the center slit (with a width of *sw*) dividing the short stub becomes capacitive. As a result, the capacitive characteristic of the slit section is connected in series with the short stub in order to obtain the characteristics as shown in Fig. 4.8.

When an open stub is connected in series with the dipole integrated with a short stub, the structure is as shown in Fig. 4.9, and the input impedance is as shown in Fig. 4.10. It is now found that the characteristics do not change at 900 MHz when an open stub is loaded and the inductance is loaded at 1.5 GHz. Hence, the impedance moves on an equi-resistance circle only at 1.5 GHz, so that matching with 50 Ω can be accomplished.

Let us now summarize the above principle. The feed circuit consisting of an open stub and a short stub works as a balun at 900 MHz, but it functions as a matching circuit at 1.5 GHz. Hence, by constructing only a balun structure, dual resonance characteristics at 900 MHz and 1.5 GHz can be obtained. Using this structure, there is no need to provide a parasitic element to realize the frequency co-use of the antenna.

4.3 Stepped Impedance Model

Dual resonance is confirmed at the center of the dipole. In order to accomplish feeding on the antenna printed on a substrate, a structure that can feed at the edge of the substrate by means of a feed line is needed. Figures 4.11 and 4.12 show the printed dipole under two condition– Type 1, in which the width of the feed line changes once, and Type 2, in which the width changes several times. In each figure, z0–z5 represents the locations where the impedance of the line is computed. The line width of Type 1 shown in Fig. 4.11 is 1.5 mm from z2 to z5, and it is 3.0 mm elsewhere. Figures 4.13 and 4.14 show the impedance loci at 900 MHz and 1.5 GHz in each model. The

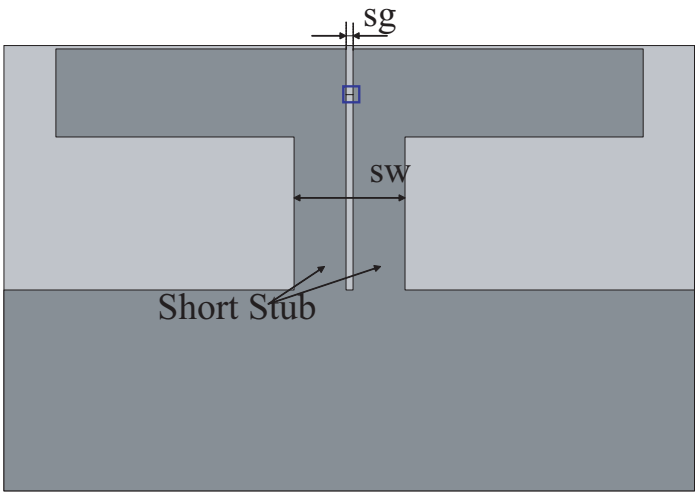

Figure 4.7: Printed dipole antenna with short-circuit stub

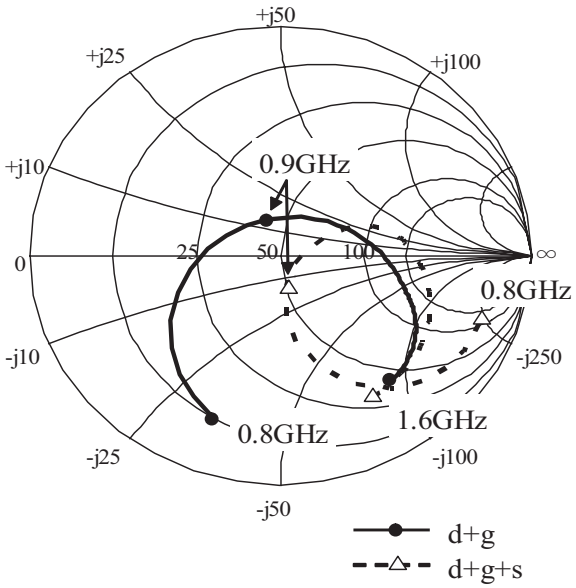

Figure 4.8: Input impedance characteristics of printed dipole with short stub

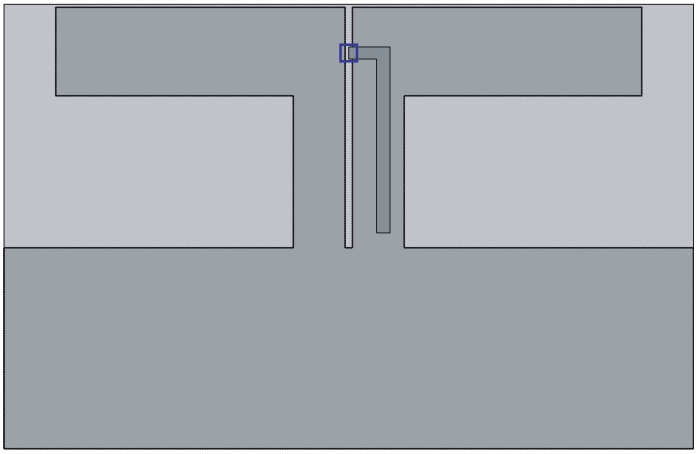

Figure 4.9: Printed dipole antenna with open-circuit and short-circuit stub

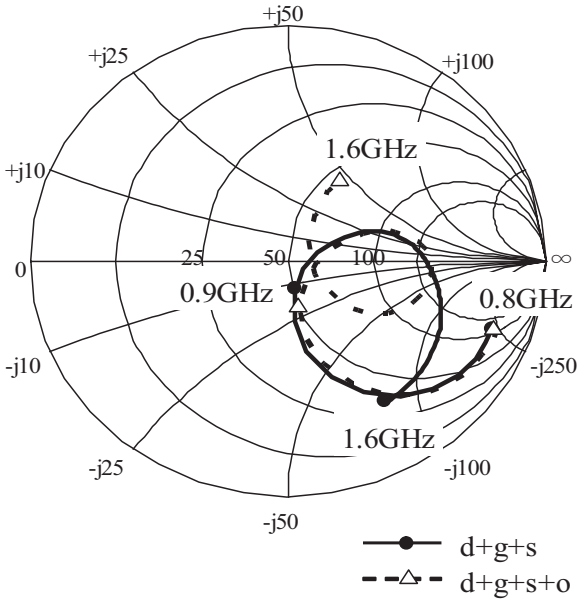

Figure 4.10: Input impedance characteristics of printed dipole with open and short stub

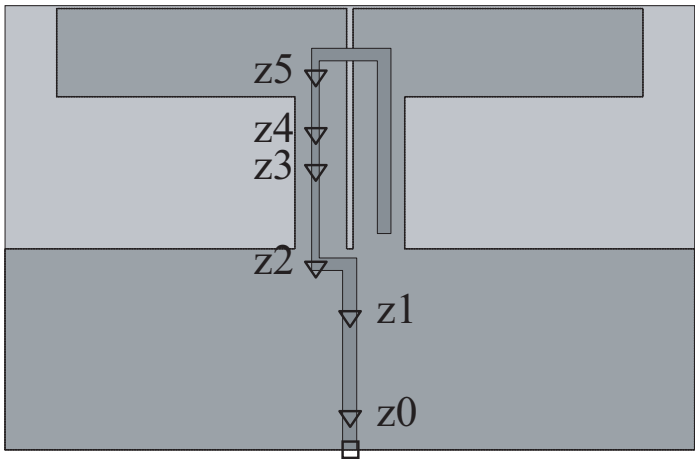

Figure 4.11: Printed dipole fed by stepped impedance line (Type 1)

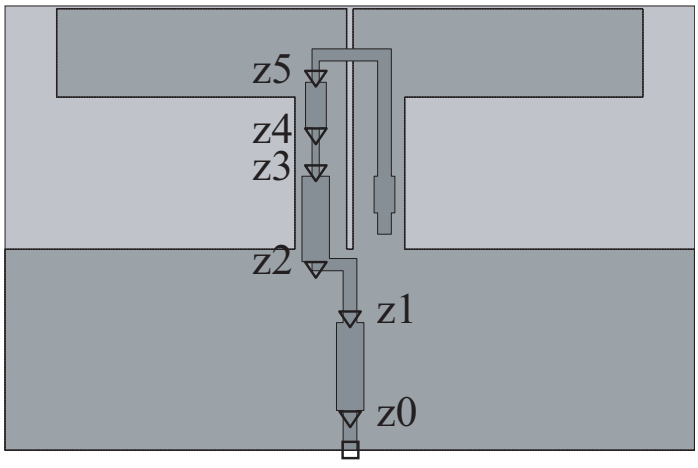

Figure 4.12: Printed dipole fed by several stepped impedance lines (Type 2)

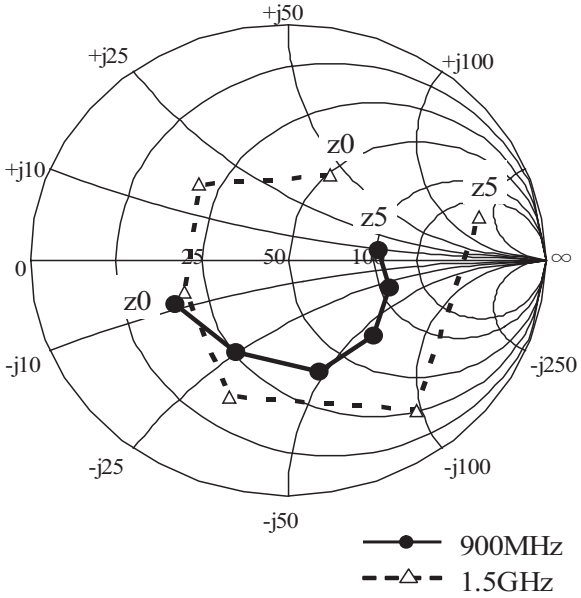

Figure 4.13: Input impedance of printed dipole type 1

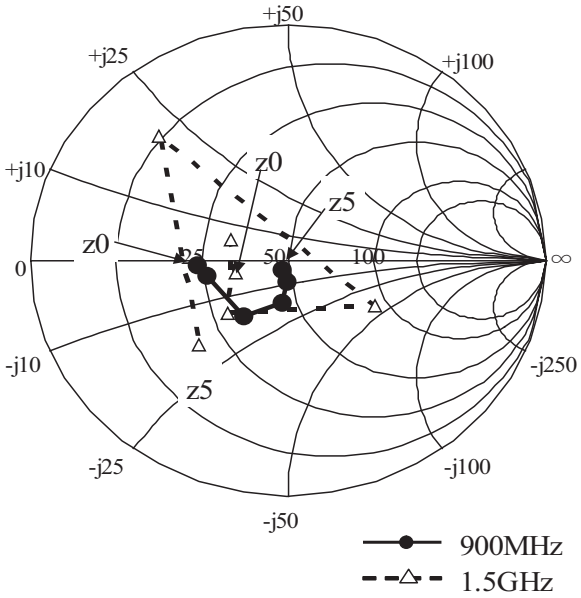

Figure 4.14: Input impedance of printed dipole type 2

impedance value at point z5 is different in Type 1 and Type 2, because the line width at the tip of the open stub changes in Type 2.

In Type 1, where the line width from z2 to z5 is narrower, a series L is loaded. The impedance matching is more effectively improved in this manner than by simply moving the feed point to the substrate edge with a 50 Ω line. However, matching is not sufficient, as can be observed in Fig. 4.13. Nevertheless, the impedance can be fine-tuned by using several stepped impedances as in Type 2. It can be observed in Fig. 4.14 that matching with 50 Ω is possible at point z0. Hence, the impedance-matching condition at the desired frequency can be adjusted by appropriately placing the step impedances. The width, length, and location of the step impedance are obtained by the cut-and-try approach.

Next, since the feed point can be modified by a feed line, a Type 2 antenna was fabricated, and the experimental and analysis values were compared. Figure 4.15 shows the input impedance characteristics and return loss characteristics. The tendency of the experimental values and that of the analysis are in agreement, confirming the effectiveness of the FDTD method used in this paper.

4.4 Multi-Frequency Antenna

Since the validity of the analysis has been confirmed by the experiment with a test antenna, the variations in the resonance frequency produced by changing the stub length are now presented. In this manner, the controllable range of the dual resonance frequencies of the present antenna can be found, and applications can be made possible. Figure 4.16 shows the impedance characteristics of the open stub when its line length lo is varied. As lo decreases, the impedance moves counterclockwise. Figure 4.17 shows the return loss characteristic when this open stub and a dipole integrated with a short stub are connected in a series. The length of the short stub is $sh = 0.144\ \lambda$.

It is now found that there is a slight change in the matching condition at 900 MHz, but that the resonant frequency is shifted at 1.5 GHz. If the range with a return loss of less than -10 dB is chosen, the frequency can be controlled with in the 1.42–1.66

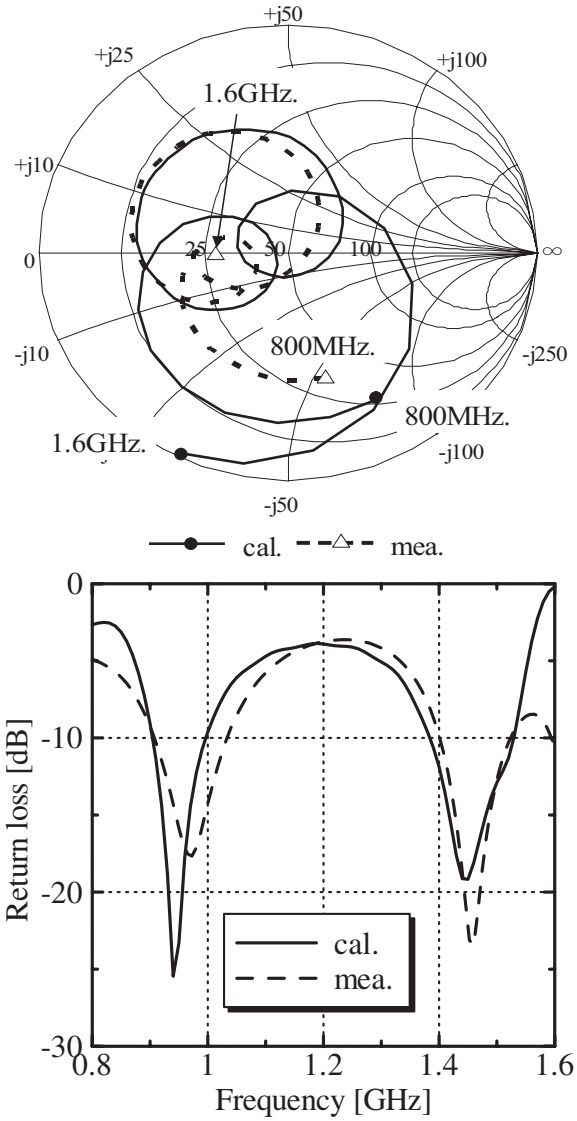

Figure 4.15: Input impedance and return loss characteristics of printed dipole

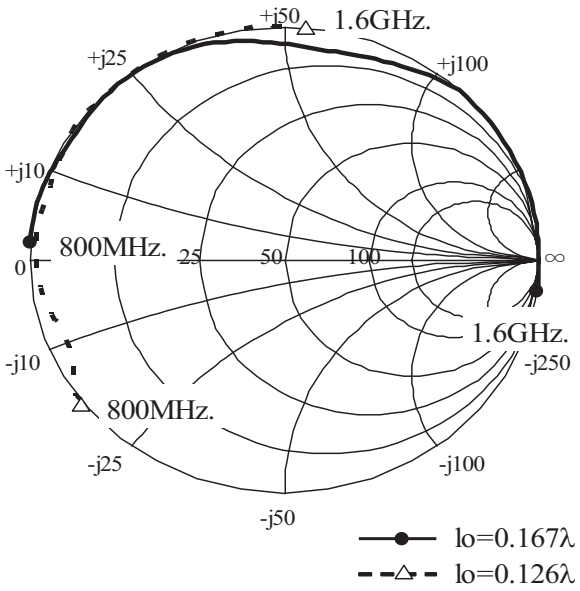

Figure 4.16: Input impedance when length of open stub is varied

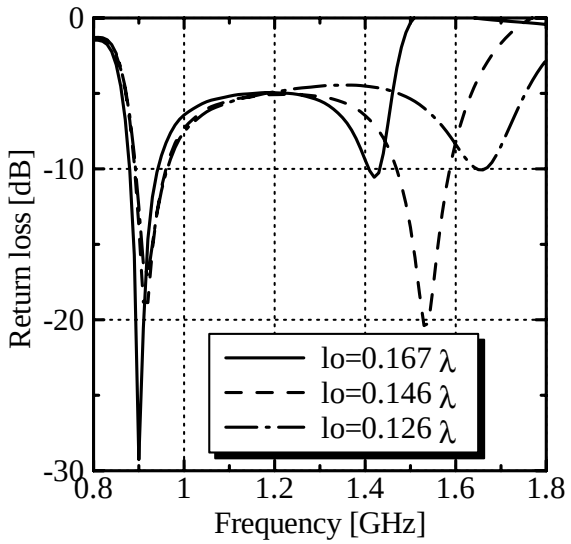

Figure 4.17: Return loss characteristics of printed dipole when length of open stub is varied

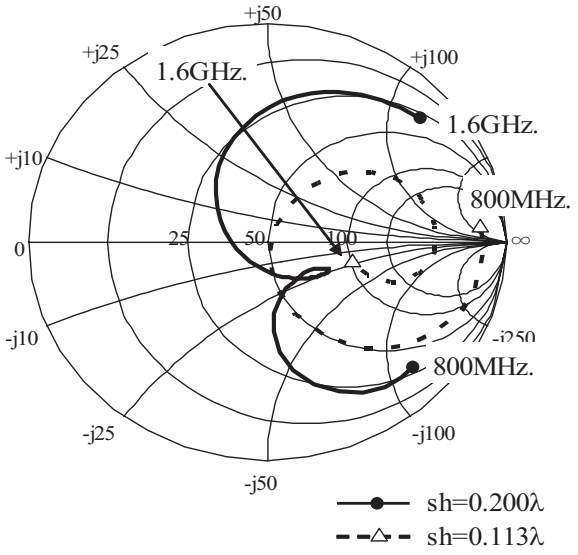

Figure 4.18: Input impedance when length of short stub is varied

GHz range. At the edges of the controllable range, there is a deterioration in the matching condition, but it can be improved by adjusting of the step impedance of th feed line. In addition, outside the controllable range, the impedance itself is near the periphery of the Smith chart. This makes it difficult to control the adjustment of the line. If matching is attempted, the feed line increases.

Similarly, Figure 4.18 shows the impedance characteristics when the short stub and the dipole with a ground plane are connected in parallel and the length sh of the short stub is varied. Figure 4.19 shows the return loss characteristics when this dipole with a short stub and an open stub (lo=0.146λ) are connected in series. It is now found that the matching condition varies somewhat at 900 MHz, while the resonant frequency is significantly shifted at 1.5 GHz. The results are substantially different from those in Fig. 4.17 when the stub length is increased (sh = 0.200 λ). The matching condition at the second resonant frequency is not deteriorated but that of the first resonance is. Figure 4.20 shows the return loss characteristic when the stub length is further increased. The second resonant frequency approaches the first resonance. Hence, if the short stub length is increased, the dual frequency characteristics approach broadband characteristics. In the case of $sh = 0.200\ \lambda$ shown

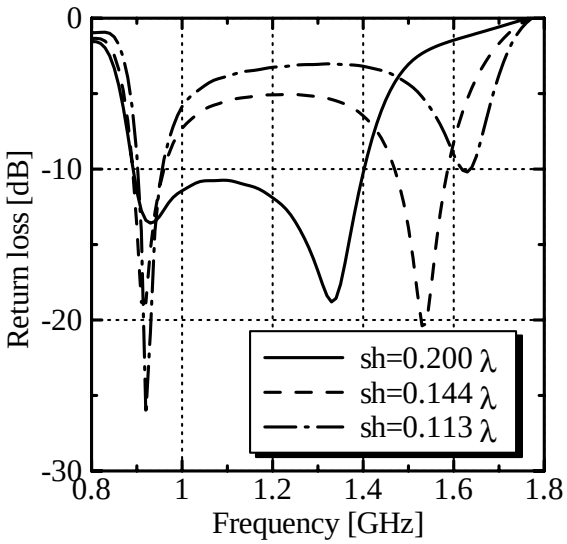

Figure 4.19: Return loss characteristics of printed dipole when length of short stub is varied

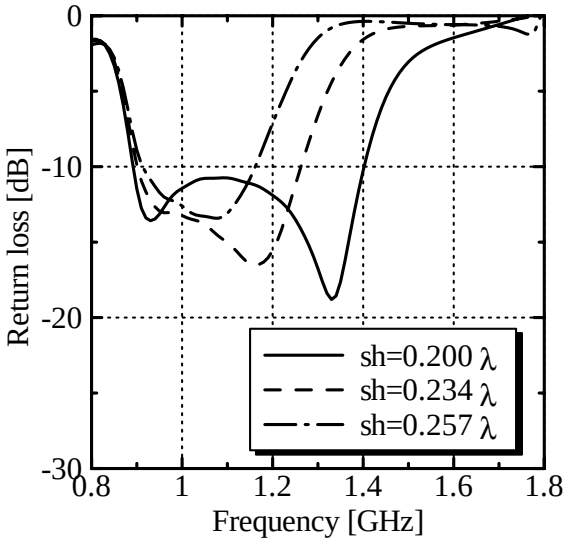

Figure 4.20: Return loss characteristics of printed dipole when length of short stub is varied

in Figs. 4.19 and 4.20, the relative bandwidth for a return loss of less than −10 dB is 43.5%. In Fig. 4.18, it is confirmed based on the kink at the center that a broadband characteristic can be realized. Hence, if the range is chosen for a return loss of less than −10 dB, the upper limit of the resonant frequency can be controlled up to 1.63 GHz by changing the short stub. The lower side of the control range cannot be defined for the above reason. In addition, the matching condition of the first resonance frequency does not change significantly even if the stub is made longer than $sh = 0.200\ \lambda$.

The above findings are now summarized. First, the short stub, with which the physical size of the antenna is determined, is adjusted by carrying out design within the frequency range that is capable of controlling the second resonant frequency. Next, by adjusting the open stub with its length arbitrarily set, the resonant frequencies are finely adjusted. The design of these feed circuits allows the dual resonance characteristics to be freely controlled. The length of the short stub indicates the length between the dipole and the ground plane. This length significantly affects the radiation pattern of the antenna. In the design of the feed line, it is necessary to take into account the radiation pattern at each frequency in addition to the circuit design for frequency co-use.

4.5 Built-in Balun Printed Dipole with Reflector

The base station antenna, which is actually used, is the corner reflector antenna composed in a radome by a printed dipole and a reflector [51]. Figure 4.21 shows a printed dipole antenna with a reflector, which has a hole for the feed line in the center of the reflector. The ground plane printed on the back of dielectric substrate is connected with the reflector. Figure 4.22 shows the return loss characteristics of a printed dipole with and without a reflector. The arrangement of the reflector significantly affect the matching conditions at 1.5 GHz. Figure 4.23 shows the current distribution on the back of the substrate and the reflector in the two resonant frequencies (f1, f2). The current on the substrate is strongly distributed at 1.5 GHz in the model without a reflector, and its current is almost suppressed by arranging a reflector.

The current on the reflector is strongly distributed at 900 MHz in the whole surface

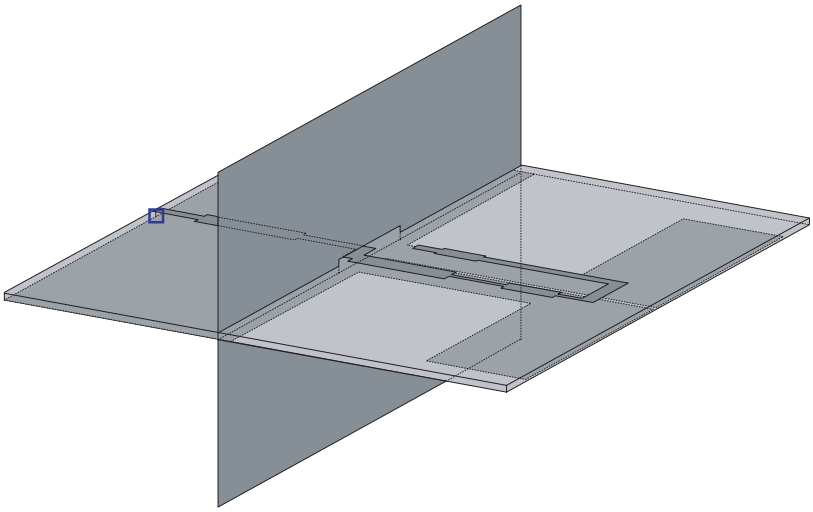

Figure 4.21: Built-in balun printed dipole antenna with reflector

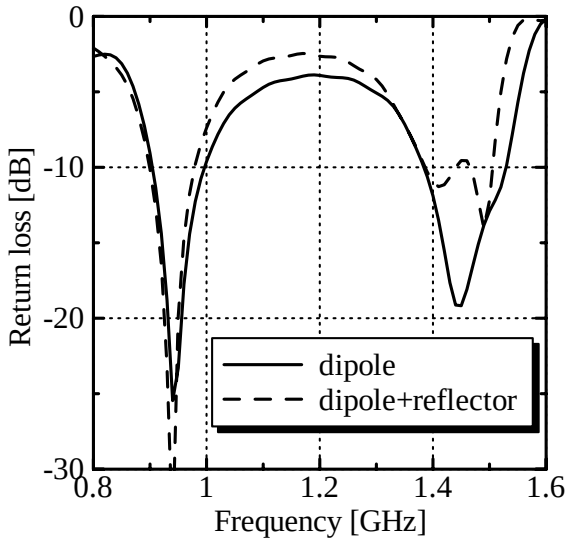

Figure 4.22: Return loss characteristics of built-in balun printed dipole antenna with and without reflector

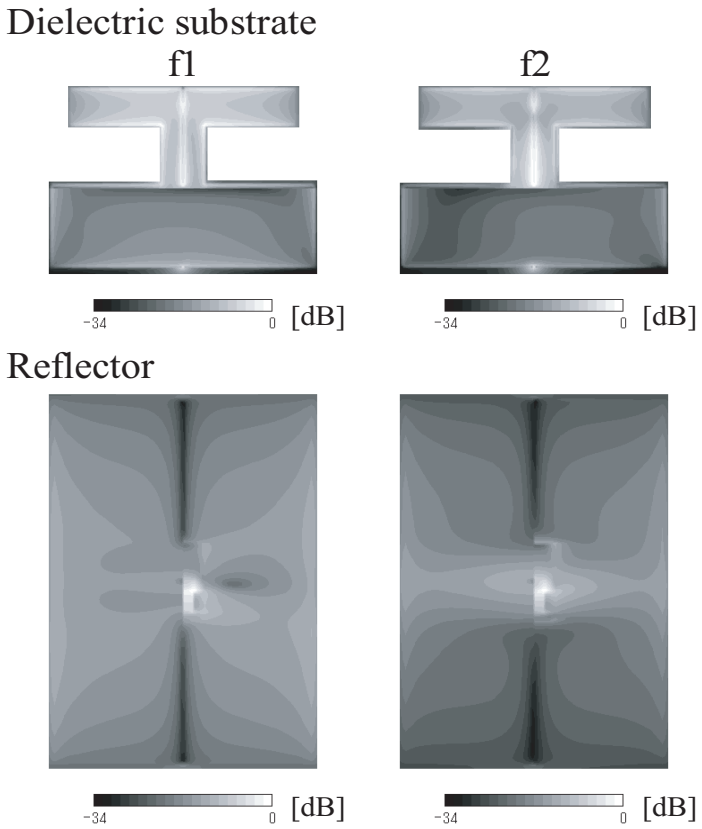

Figure 4.23: Current distribution of built-in balun printed dipole antenna with reflector (f1 = 900 MHz, f2 = 1.5 GHz)

of the reflector. However, the current is strongly distributed at 1.5GHz in the vertical direction of the substrate from the feed point, and there are few currents distributed in other parts of the reflector.

Next, the characteristics of the antenna with the reflector is examined. Figure 4.24 shows a printed dipole antenna without a balun to compare the built-in balun type. Figure 4.25 shows the current distributions of each model at 900 MHz and 1.5GHz. The current distributed in the reflector is small in the case of the dipole without a balun. When a balun is connected, the current distributed specially in the reflector at f2 is large. Because the length of open and short stub becomes 0.42 λ at f2, and its circuit functions as a matching circuit at f2.

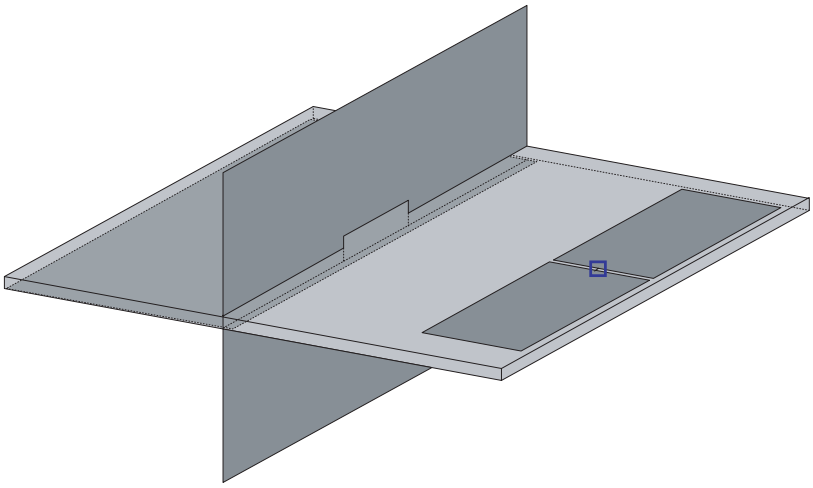

Figure 4.24: Printed dipole antenna with reflector

Figure 4.26 shows E-plane (xy plane) radiation pattern in each model at f1 and f2 to examine the effect of the current distributed in the reflector. The radiation pattern agree in each model and each frequency. Therefore, there are few influences on the radiation pattern though the current is strongly distributed with the antenna with a balun in the reflector.

4.6 Summary

The operating principle of a balun for feeding a printed dipole antenna as a frequency co-use antenna is analyzed by the FDTD method. The parameters of the open stub connected to the dipole antenna in series and the short stub connected in parallel are investigated in detail. It is found that these stubs realize dual resonances. The controllable range of the dual resonant frequencies is found by varying the lengths of the open and short stubs. There are few influences on the radiation pattern though the current is strongly distributed with the antenna with a balun in the reflector.

This antenna has already been put to practical use in a triple band antenna for the cellular base station [63].

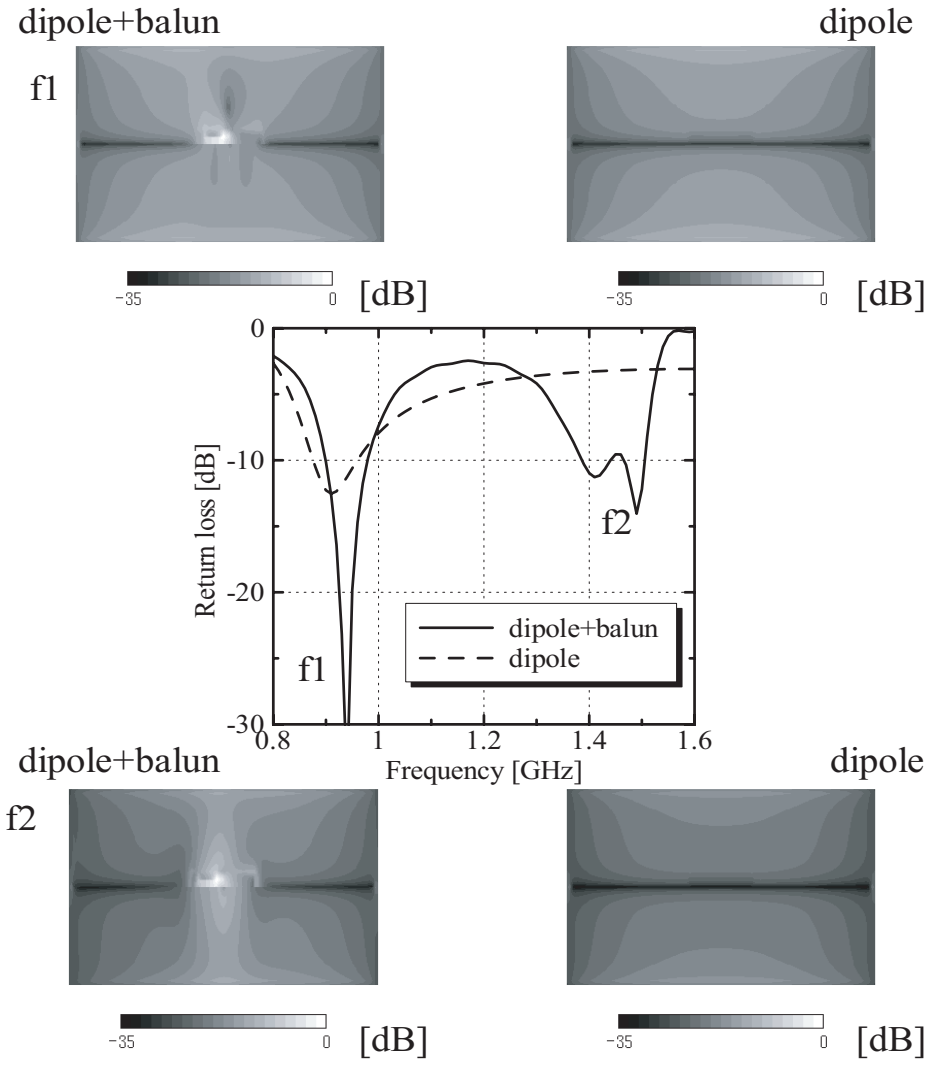

Figure 4.25: Current distribution of printed dipole with and without balun (f1 = 900 MHz, f2 = 1.5 GHz)

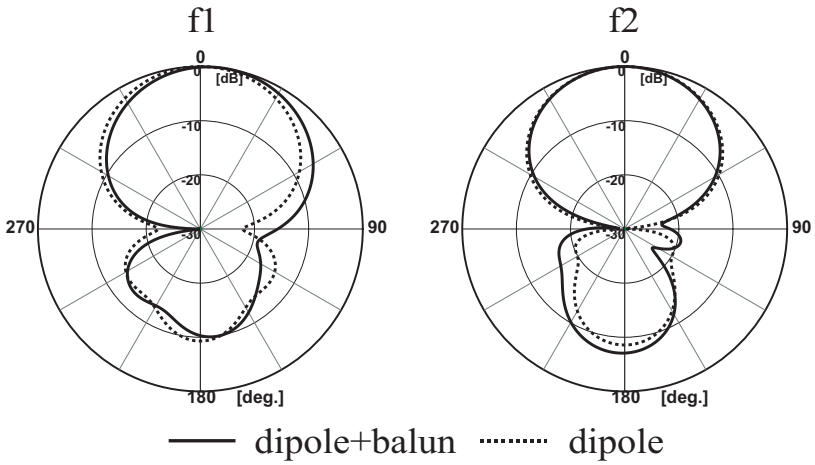

Figure 4.26: Radiation pattern characteristics of printed dipole with and without balun at 1.5 GHz

Chapter 5

Modeling of GaAsFET for Active Integrated Antenna

5.1 Introduction

In this chapter, we investigate the FDTD analysis of an active integrated antenna with an amplifier or an oscillator. The GaAs FET is implemented by TOM, and a state equation is directly solved by the parameters of the equivalent circuit, which is mentioned in the device sheet [82][83][84]. The voltage source approach is examined in the 8.5 GHz low noise amplifier, and we discuss the process of DC excitation and the convergence characteristic. The experimental results are compared with the calculated results for the radiation pattern of an active patch antenna, and we show the increase in the cross polarization level. We also examine the radiation pattern of an active slot antenna. Furthermore, we show that the cross-polarization level can be controlled by separating the radiation and circuit parts in the face and the back of a substrate.

Next, an active integrated antenna with an oscillator is discussed. The voltage source, which is precisely modeled the actual structure for a coplanar waveguide, is presented. An oscillating condition significantly depends on the coupling between the elements, and the effect of the length of the gate and drain line to the oscillating frequency is examined in detail.

Table 5.1: FDTD analytic condition for active device

Cell Size	$\Delta x = \Delta y = \Delta z$ =0.262mm
Time Step	0.454ps
Iteration	15,000 time steps
ABC	PML 8 layer
Incident Voltage	Gaussian Pulse modulated at 8.5GHz

5.2 Combined FDTD for Active Devices

Figure 5.1 shows the analytic model of an 8.5 GHz low-noise amplifier, which uses HJFET (NE3210S01). The circuit parameter of TOM, which is one of the large-signal circuit models, is mentioned in the device sheet [84]. In this section, we calculate the state equation of TOM by using this parameter in each time step by the Newton-Raphson method. This calculation was performed based on the voltage source approach to achieving a combination with an electromagnetic field [78].

Figure 5.2 shows the TOM model. The nonlinear circuit elements are the gate-source capacitor C_{gs}, gate-drain capacitor C_{gd}, drain current I_{ds}, gate current I_{gs}, and drain-gate current I_{gd}. The parameters of C_{gs}, C_{gd}, I_{gs}, and I_{gd} are the same as expressed by the Statz model, and the state variables are capacitor voltage $v_g, v_{G'D'}, v_d$ and inductor current i_{L_g}, i_{L_d}. A state equation is composed of the node equation, which can be obtained by applying Kirchhoff's first law to the G', D' node of Fig. 5.2, to the equation of the electric potential of the difference between $G' - D' - S'$ and $G' - S'$, and to the equation that contains the voltage source of a gate and drain of Thevenin's theorem.

Table 5.1 shows the FDTD analytic condition in this section. The bias voltage is an exponential rising function, and the incident voltage presented a delay of 5,000 steps, because the Gaussian pulse must be fed after the bias voltage fully stabilizes [85]. The S parameter is calculated by the following process. First, a microstrip line of 50 Ω is modeled only on the infinite ground plane. The incident pulse is fed and a voltage (V_{inc}) is obtained at the observation point. Next, the amplifier

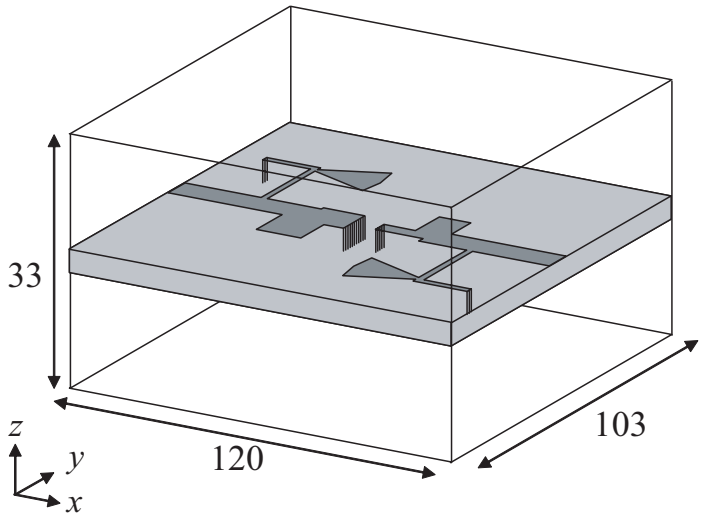

Figure 5.1: Analytic model of low noise amplifier on infinite ground plane (unit : cell).

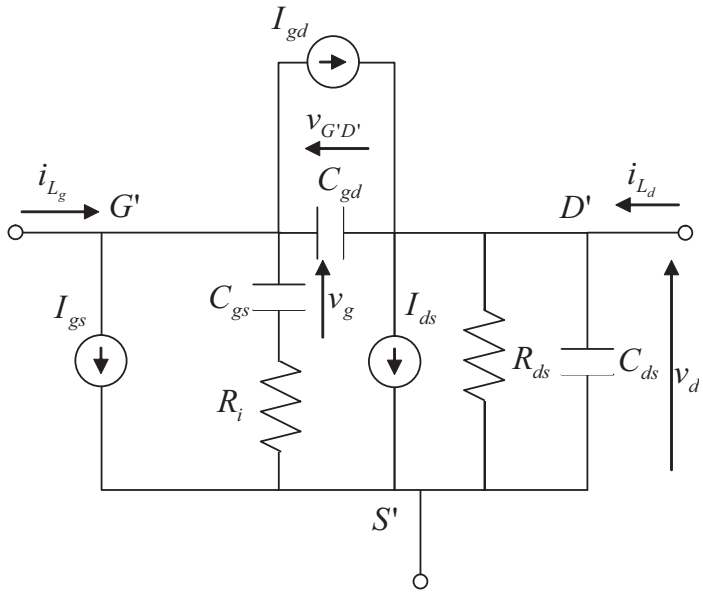

Figure 5.2: TOM model.

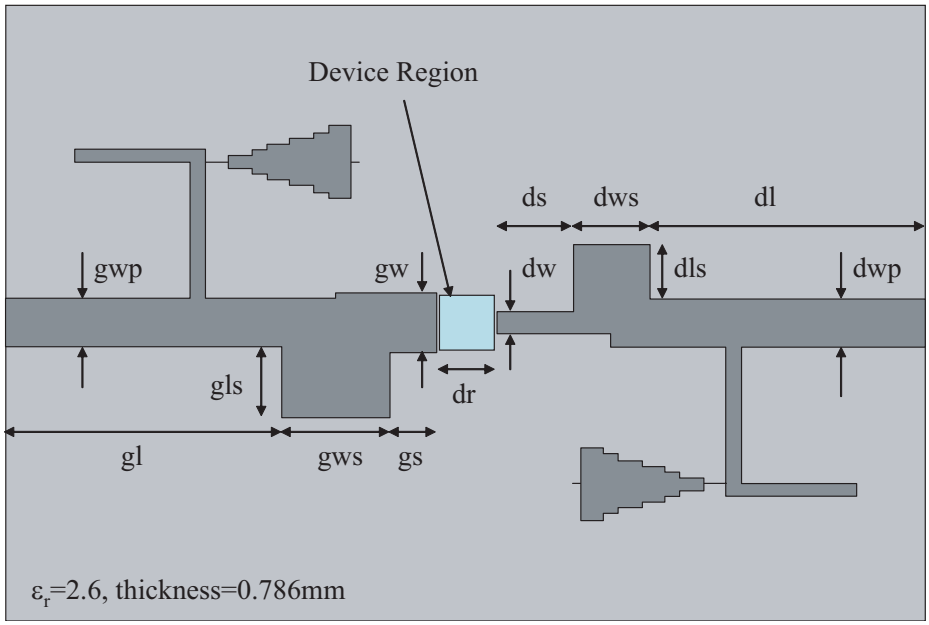

gw=2.62, gs=1.572, gws=3.668, gls=3.144, gwp=2.096, gl=9.432, dw=1.048, ds=2.62, dws=2.62, dls=2.358, dwp=2.096, dl=9.432, dr=2.096 [mm]

Figure 5.3: Structure of low noise amplifier.

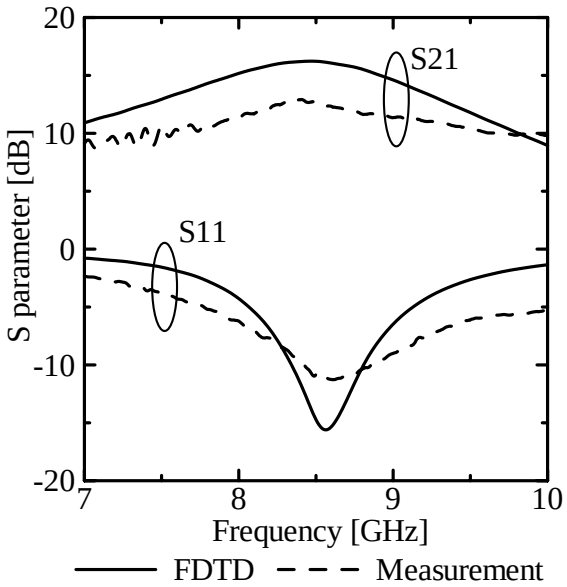

Figure 5.4: Calculate and experiment results of S parameters.

(including the matching circuits) is modeled. Only the bias voltage is fed, and the voltage (V_{bias1}, V_{bias2}) at the observation points is obtained. Finally, the bias voltage and incident pulse are fed, and the voltage (V_{obs1}, V_{obs2}) at the observation points is obtained. The S parameter can be calculated by

$$S11 = (V_{obs1} - V_{bias1} - V_{inc})/V_{inc} \quad (5.1)$$

$$S21 = (V_{obs2} - V_{bias2})/V_{inc}. \quad (5.2)$$

Figure 5.3 shows the structure and parameters of the low noise amplifier. Figure 5.4 shows the analytic result obtained by the FDTD method of the model, including the bias circuit. The analytic result of the matching frequency of S11 is agreement with the experimental result. The gain of the experiment result of S21 is lower than the calculation, because an infinite ground plane is used in the analysis. Figure 5.5 shows the existence of modeling of the bias circuit. When a bias circuit does not exist, the bias voltage is renewed by accumulation in all the components of E_z under the main microstrip line. When a bias circuit exists, a short pin ($E_z = 0$) is set up

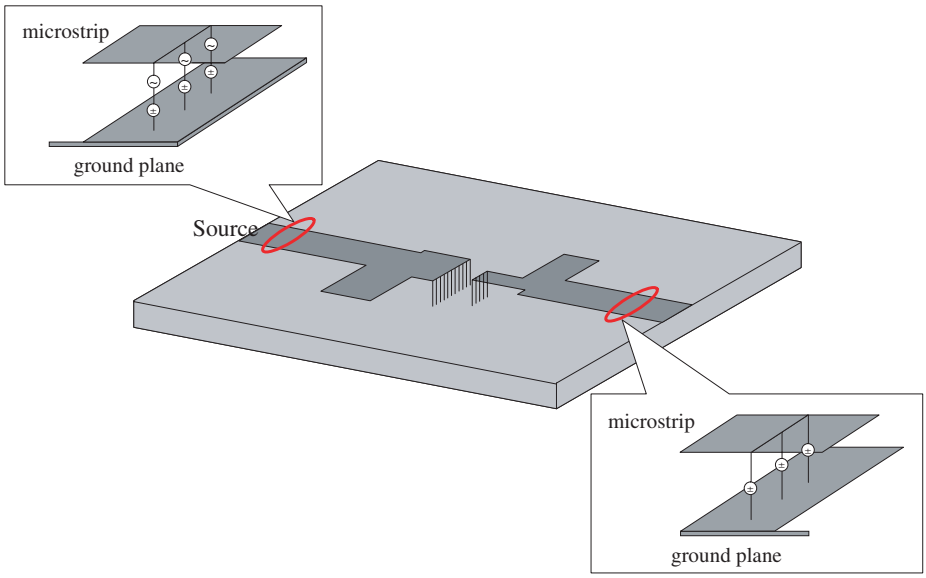

(a) without bias circuit

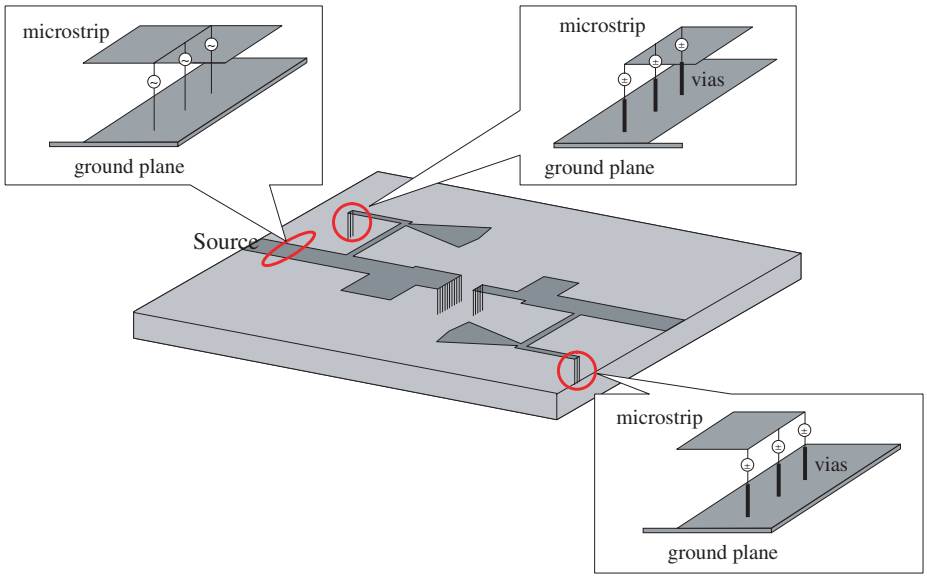

(b) with bias circuit

Figure 5.5: Modeling of bias circuit.

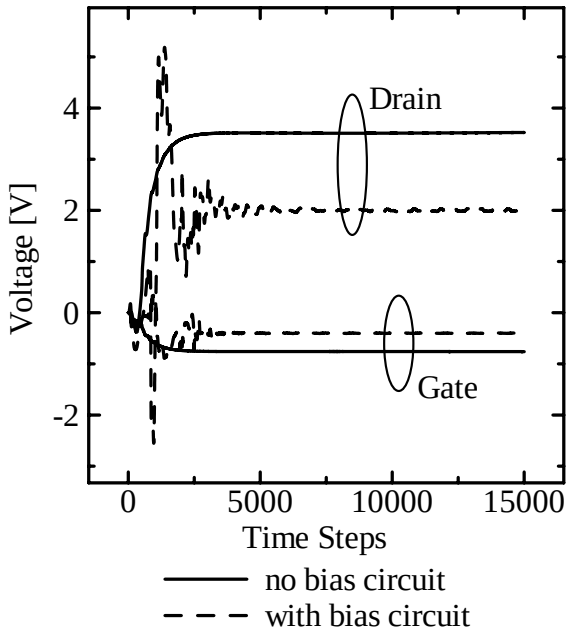

Figure 5.6: Voltage characteristics of gate and drain.

under the edge of the pad, and the bias voltage is renewed by compelling at 1 cell under the pad. The bias setting voltages are $V_{gs} = -0.4$ V, $V_{ds} = 2.0$ V.

Figure 5.6 shows the gate and drain voltage characteristics when bias circuit exists. The voltage converges on the setting voltage when the voltage is fed by setting up a bias circuit. The bias voltage does not stabilize in the accumulation renewal, that is, the open condition when a voltage is fed. It vibrates when connected, in particular with the antenna. On the other hand, a voltage standard stabilizes, because it is physically connected with the ground plane in the compulsory renewal, that is, the short condition when a voltage is fed. Therefore, the voltage that is fed at the bias circuit converges on the setting voltage.

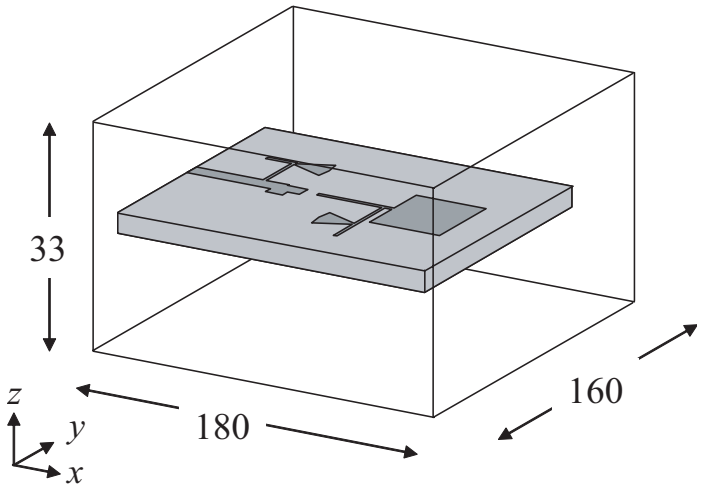

Figure 5.7: Analytic model of active patch antenna with amplifier.

5.3 Active Integrated Antenna with Amplifier

5.3.1 Active Patch Antenna

Figures 5.7 and 5.8 show the model and structure parameters of an active patch antenna with amplifier [75]. In this model, the patch antenna is connected with the drain side. The matching circuits for the gate and drain sides were redesigned under the condition wherein a patch antenna was connected. Figures 5.9 and 5.10 show the co- and cross- polarization of radiation pattern characteristics on the E and H planes. On this graph, the radiation pattern of the normal patch antenna with the feed offset in the 50 Ω microstrip line is also plotted. Moreover, each figure shows the experiment value of the radiation pattern of active receiving antennas that connect a patch antenna with the gate side. The level of this radiation pattern is standardized with the gain in the maximum radiation direction of each antenna.

Though an analytic result largely corresponds with the experimental value, an error can be confirmed for the radiation pattern on the back of the substrate. This depends on whether the lead line is being connected with the gate and drain from the power supply. The cross polarization level of the simple patch antenna is less than −40 dB in the analytic result. In the case of the active antenna, a maximum radiation

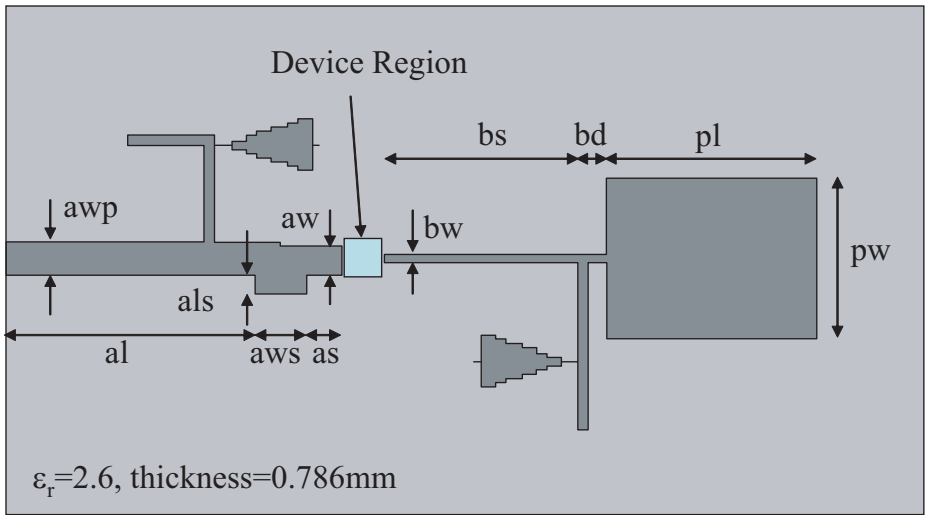

aw=1.834, as=1.834, aws=2.62, als=1.048, awp=2.096, al=12.838, bw=0.524, bs=9.956, bd=1.572, pl=10.742, pw=9.956 [mm]

Figure 5.8: Structure of active patch antenna with amplifier.

of −6.9 dB can be confirmed in the E plane, and that in the H plane becomes −12.1 dB. Therefore, when the active function is added to the patch antenna, the increase in the cross polarization component is analyzed.

Figure 5.11 shows the electromagnetic distribution of the active patch antenna, and the H_x component is strongly distributed along the edge of the patch. Moreover, the H_y component is strongly distributed along the drain-side bias line, and this component is the cause of the increase in the cross polarization. It becomes necessary to change the position of the drain-side bias line or shield a circuit. This separates it from the radiation part to control a cross polarization.

Figure 5.12 shows the structure of a shield box, which surrounds the part of the low noise amplifier. The shield box has a hole, through which a microstrip line is passed on the drain side to feed a patch antenna. This hole is away from the circuit part, approximately 1 cm to the top of the box. Figure 5.13 shows the radiation pattern with and without a shield box for comparison. The level of the radiation pattern is standardized by the maximum value. Cross polarization with a shield box becomes less than −30 dB of the radiation pattern in the E plane, though that

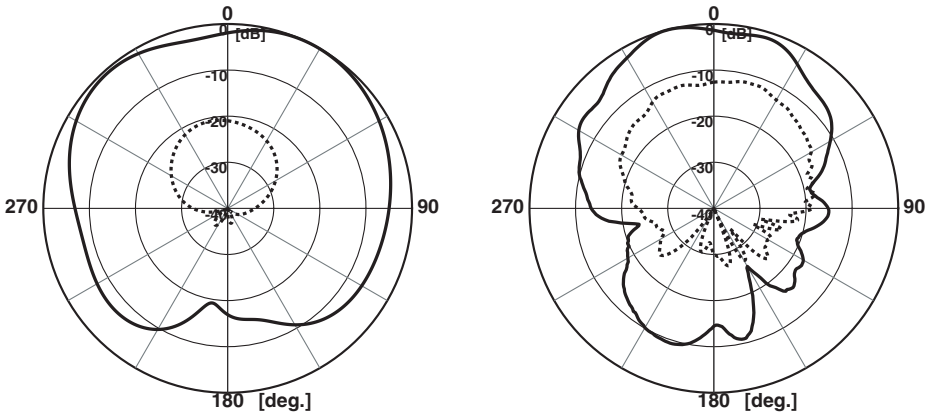

FDTD Measurement

(a) Co-polarization

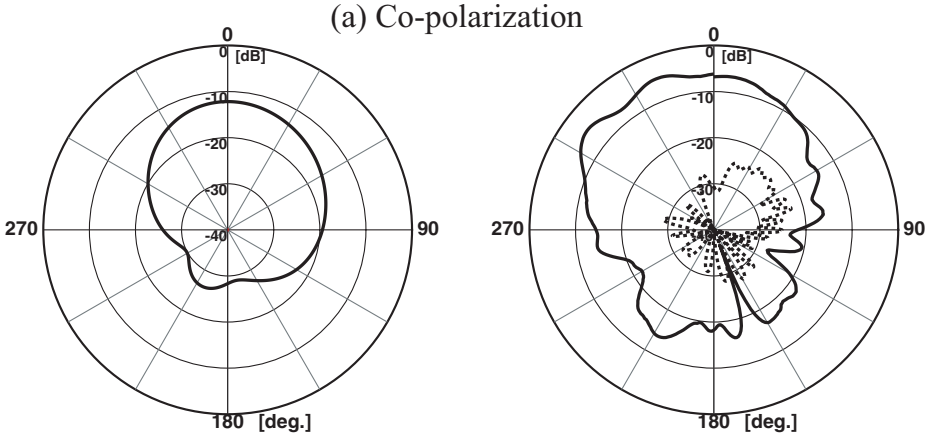

FDTD Measurement

(b) Cross-polarization

Active antenna ····· Patch antenna

Figure 5.9: Radiation pattern of E plane.

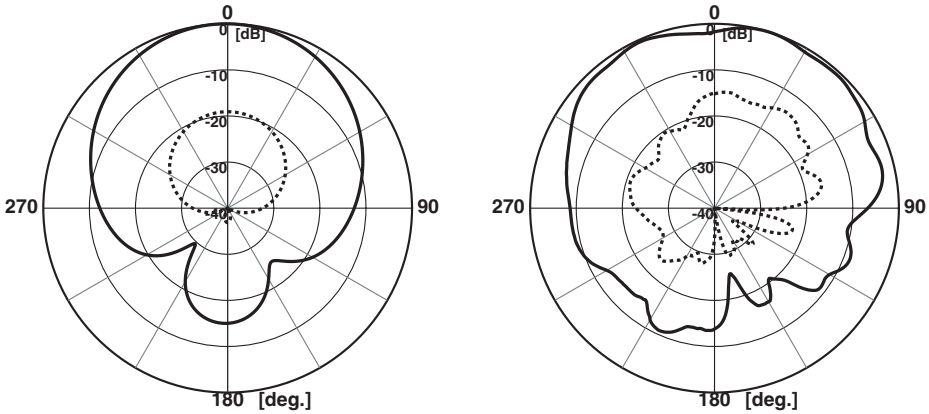

FDTD Measurement

(a) Co-polarization

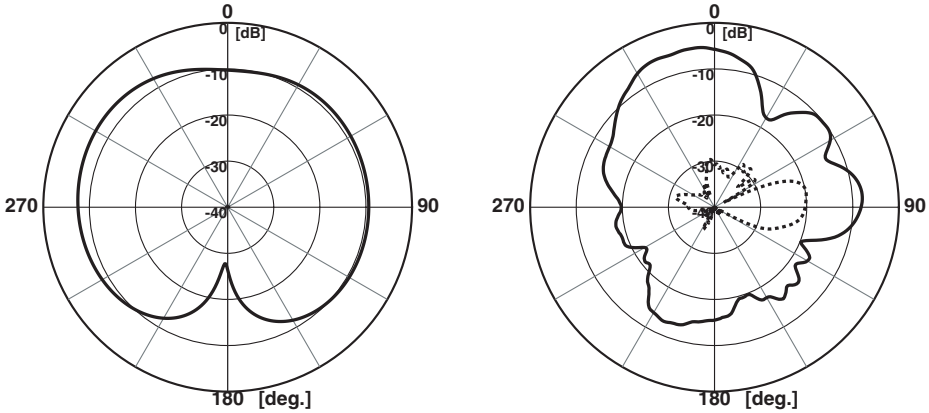

FDTD Measurement

(b) Cross-polarization

Active antenna ····· Patch antenna

Figure 5.10: Radiation pattern of H plane.

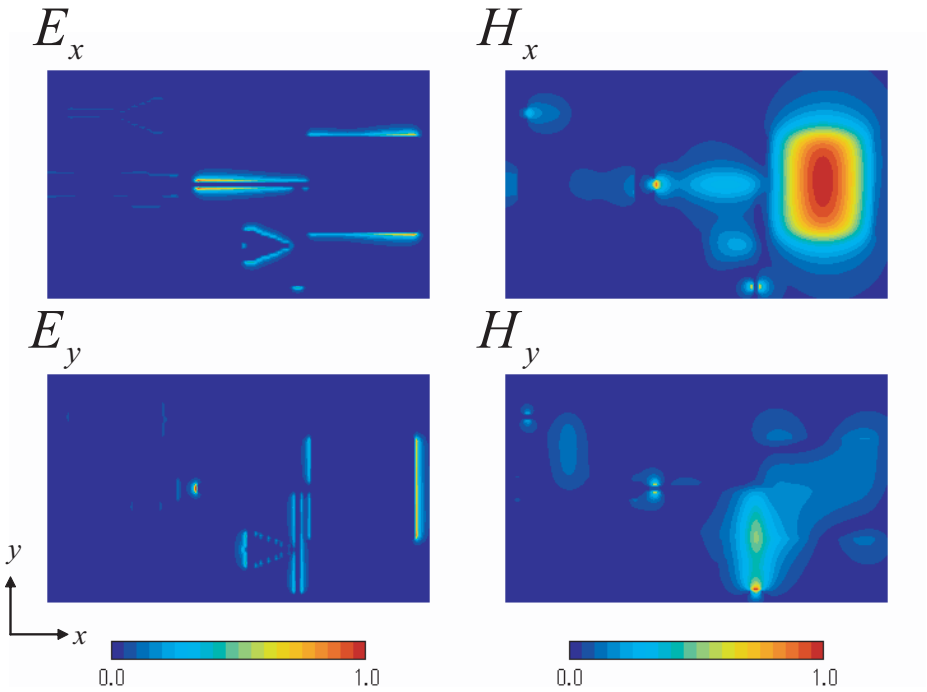

Figure 5.11: Current distribution.

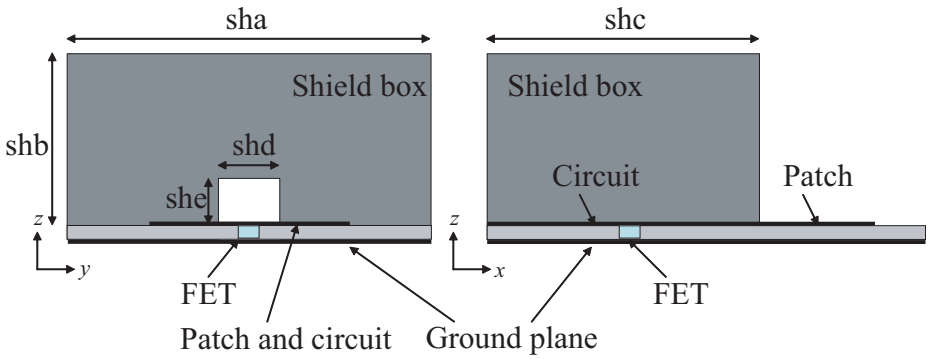

sha=31.44, shb=9.694, shc=29.344, shd=5.24, she=2.62 [mm]

Figure 5.12: Structure of active patch antenna with shield box.

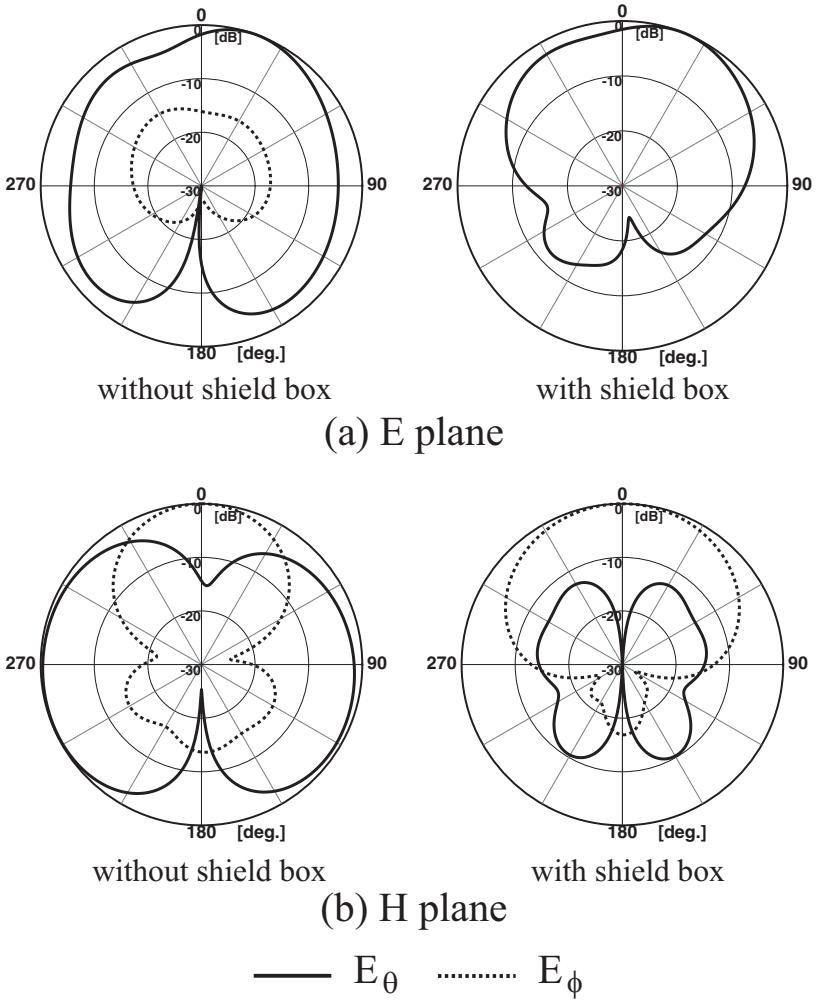

Figure 5.13: Radiation pattern with shield box.

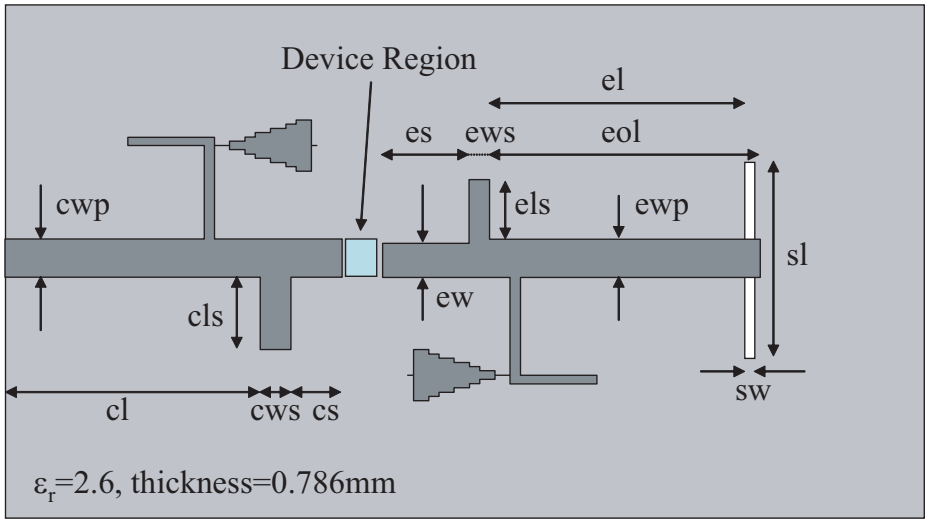

cs=2.62, cws=1.572, cls=4.454, cwp=2.358, cl=13.1, ew=2.096, es=4.454, ews=1.048, els=3.668, ewp=2.358, el=13.1, eol=13.886, sl=12.052, sw=0.524 [mm]

Figure 5.14: Structure of active slot antenna with amplifier.

without the shield box becomes −15 dB. The cross polarization with a shield box can be decreased by −10 dB compared with the radiation pattern in the H plane, though the same radiation level can be confirmed without a shield box for co- and cross- polarization.

Therefore, we confirmed that the repression of cross polarization of an active patch antenna was effective in shielding a circuit part.

5.3.2 Active Slot Antenna

Figure 5.14 shows the structure parameter of an active slot antenna with an amplifier. This antenna is designed such that it comprises a low noise amplifier and a slot antenna connected with the drain side to individually achieve an impedance matching of 50 Ω. Figures 5.15 and 5.16 show the radiation pattern of the active patch and active slot antennas in the zx and yz planes. In the case of each antenna, the radiation pattern is normalized with the gain in the maximum radiation direction. The ground plane is assumed to be infinity, and the 0 degree direction of the graph becomes a

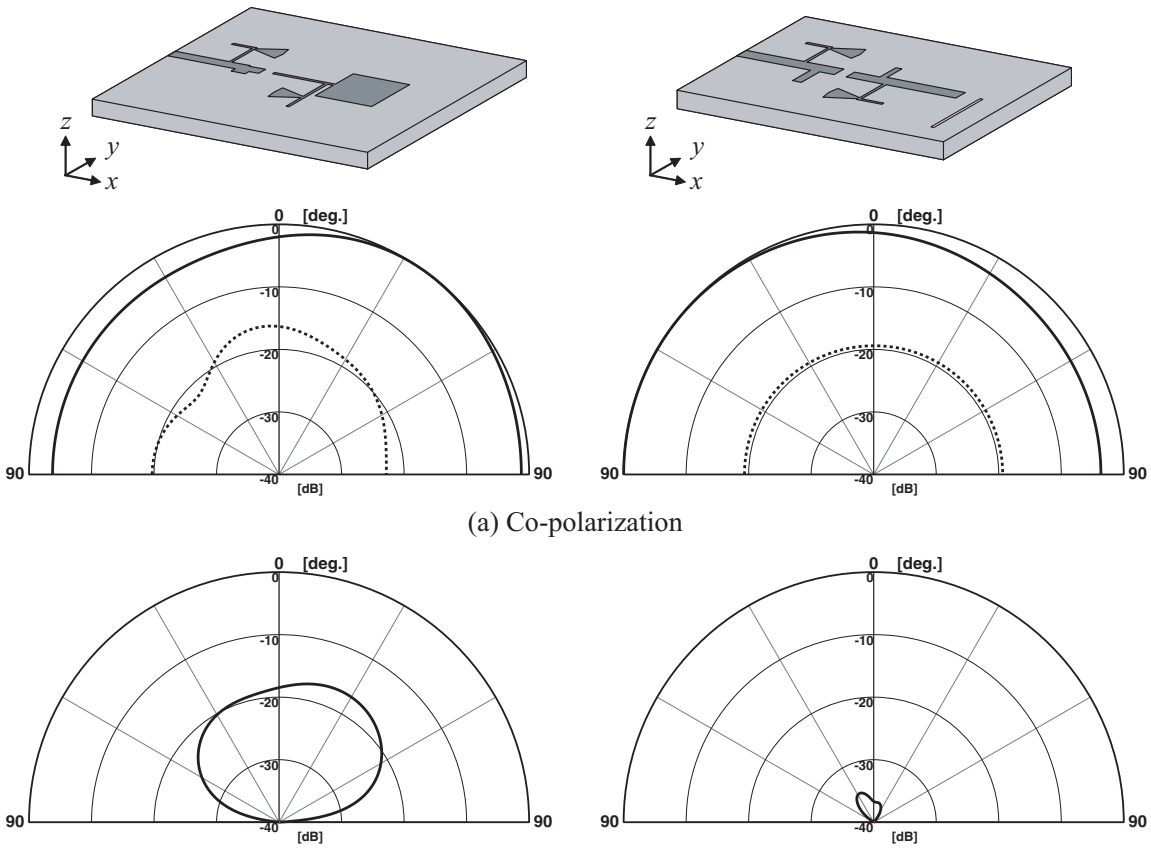

(a) Co-polarization

(b) Cross-polarization

With Active Element ····· Radiation Element Only

Figure 5.15: Radiation pattern of zx plane.

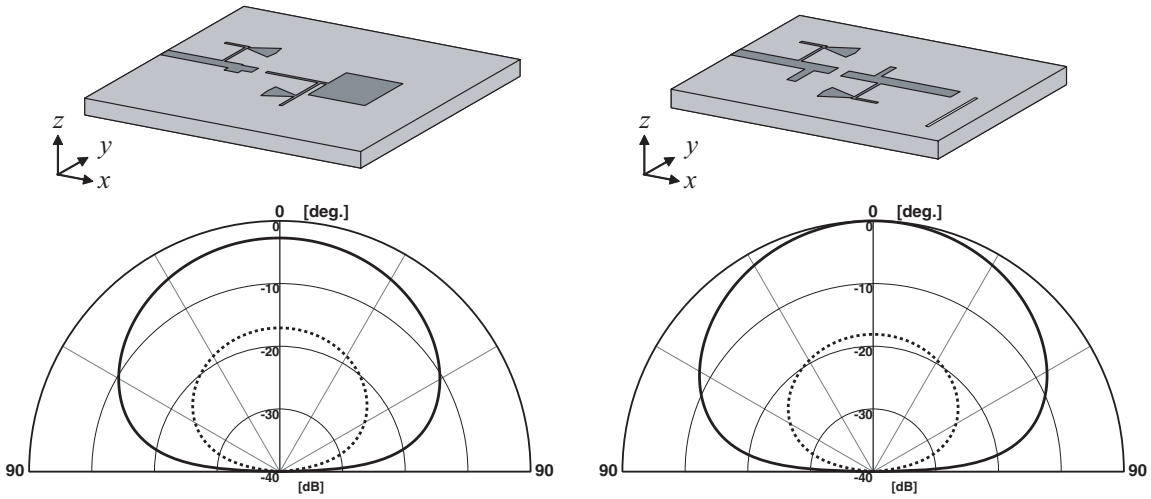

(a) Co-polarization

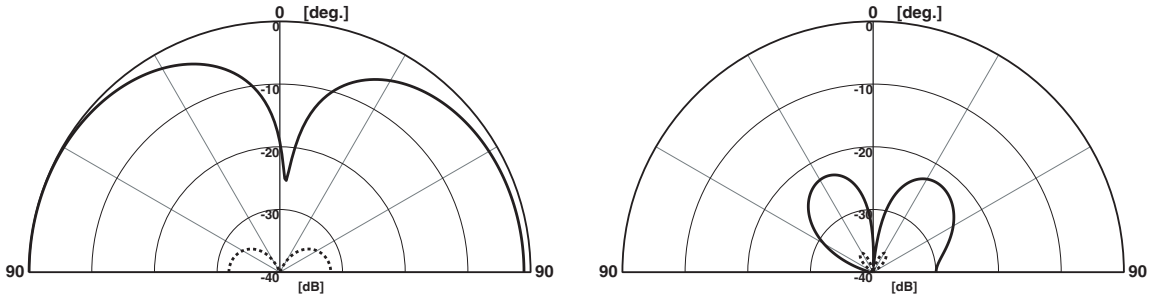

(b) Cross-polarization

With Active Element ····· Radiation Element Only

Figure 5.16: Radiation pattern of yz plane.

patch in the $+z$ direction and a slot antenna in the $-z$ direction, respectively. Based on the analytic result, when the radiation element is a slot antenna, cross polarization can be controlled in comparison with an active patch antenna in the zx plane of 34 dB and the yz plane of 39 dB.

Therefore, the increase in cross polarization can be controlled by using the slot antenna of which a radiation part can be separated from the circuit part. The radiation to the back of the ground plane cannot be ignored, because the antenna is, in actuality, constructed on a finite ground plane. Furthermore, we must examine the shape of the shield box in detail to control unnecessary radiation. Research on these issues, including the analytic method, must be conducted in the future.

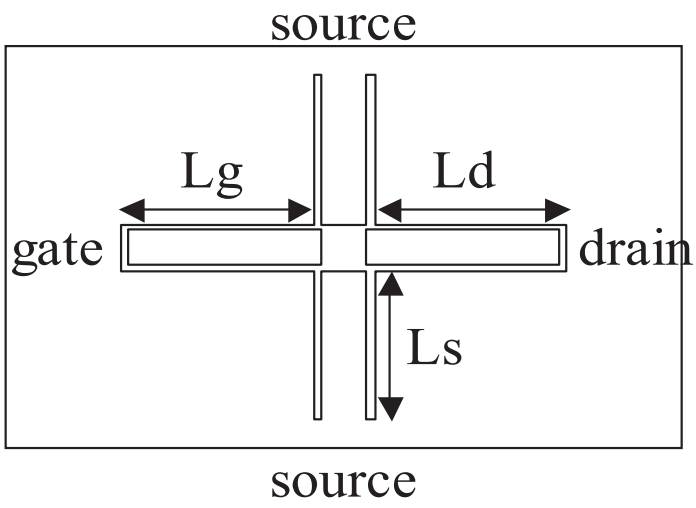

Figure 5.17: Analytic model of active antenna with oscillator

5.4 Active Integrated Antenna with Oscillator

5.4.1 Voltage Source Approach for Coplanar Waveguide

Figure 5.17 shows the structure of an active antenna with an oscillator [86][87]. A GaAsFET (NE3210S01) is installed in the substrate ($\varepsilon_r = 2.6$) of $84.8 \times 68.8 \times 1.6$ [mm]. A DC bias voltage of 3.0 V is applied to a drain port, and an output port is observed when a feed pin is connected in the center of a drain conductor. The size of a cell is $\Delta x = \Delta y = \Delta z = 0.4$ mm, the iteration is 6,000, and the absorbing boundary condition is an 8-layer PML. The equivalent circuit of the FET is shown with TOM, and a state equation is solved at each time step of the FDTD. Figure 5.18 shows the voltage source needed to combine the electromagnetic and circuit calculation. In model A, a pin is connected with the ground conductor (source line) from the center conductor of a coplanar waveguide (gate and drain line), as shown in Fig. 5.18(a). Model A precisely models the actual structure, because four leads of the FET are connected in each of the gate, drain, and two source lines. The voltage source of model B is located directly below the microstrip line, which is connected with the ground plane, as shown in Fig. 5.18(b).

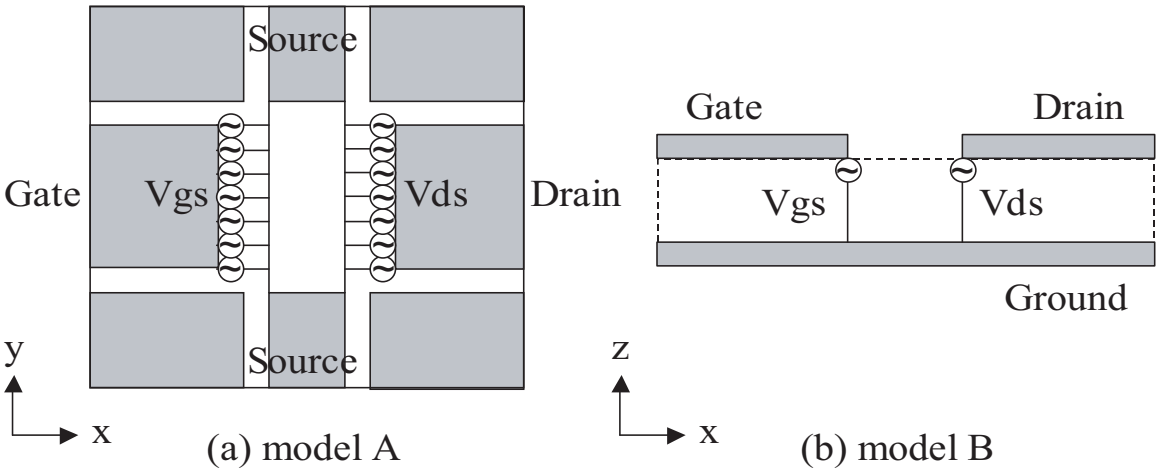

Figure 5.18: Voltage source for coplanar waveguide

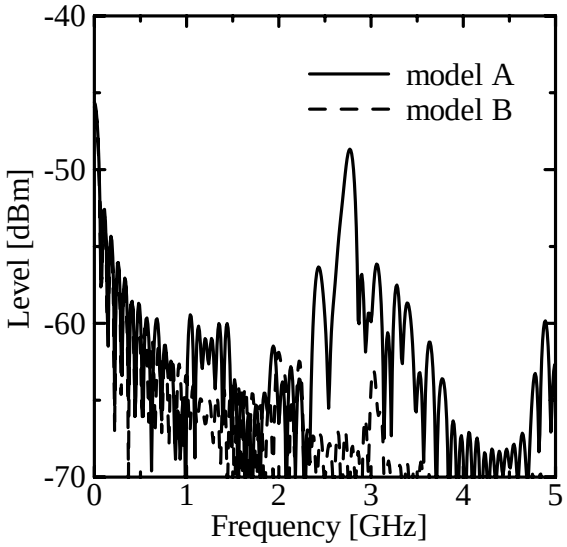

Figure 5.19: oscillating frequency of two voltage source types

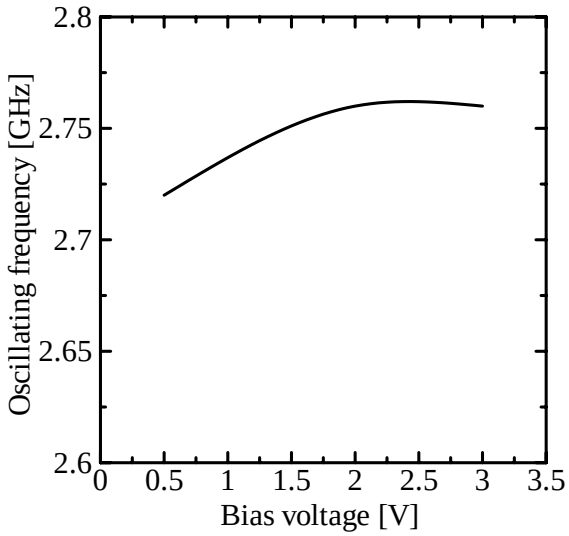

Lg=Ld=35, Ls=25 [mm]

Figure 5.20: Oscillating frequency when the bias voltage is varied.

Figure 5.19 shows the oscillating frequency of two voltage source types. An oscillating frequency can be confirmed with the model A. However, spectrums except for the oscillating frequency exists, and unstable with each model.

5.4.2 Oscillating Frequency

Figure 5.17 shows the analytic model of an active antenna with an oscillator. The width of the coplanar line is 0.2 mm. The edges of the two source lines are connected to each other via the ground conductor. Figure 5.20 shows the oscillating frequency when the bias voltage V_{ds} is varied. Figure 5.21 shows the oscillating frequency when the length of the source line L_s is varied. The effect of V_{ds} and L_s on the oscillating frequency is minimal, but L_s influences the oscillating level. Figure 5.22 shows the oscillating frequency when the sum of the length of the gate and drain line is varied. L_s is the quarter wavelength of the oscillating frequency. The oscillating frequency is that wherein $L_g + L_d$ becomes a half-wavelength. f_0 is the plotted value when the frequency is converted into half of the free space wavelengths. The experimental value is in agreement with the analytic results.

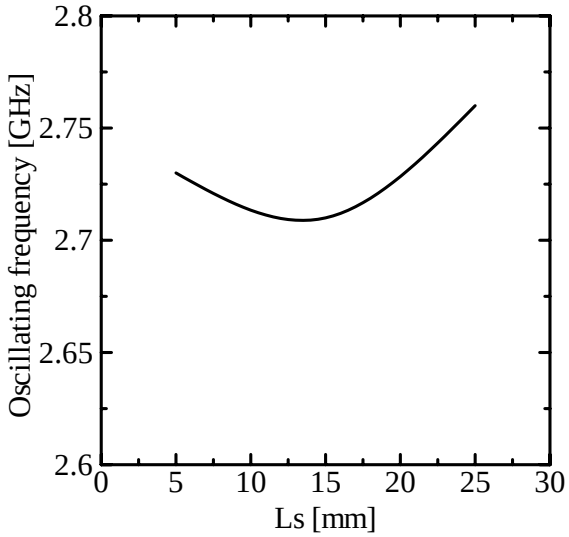

Lg=Ld=35 [mm], Vds=2.0 [V]

Figure 5.21: Oscillating frequency when L_s is varied.

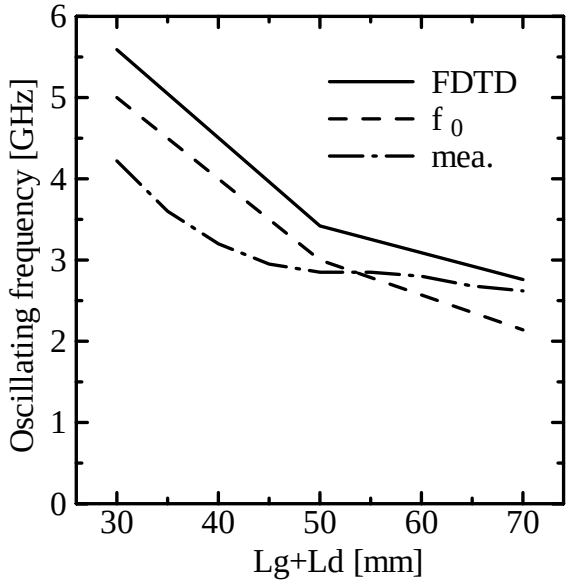

Figure 5.22: Oscillating frequency when $L_g + L_d$ is varied.

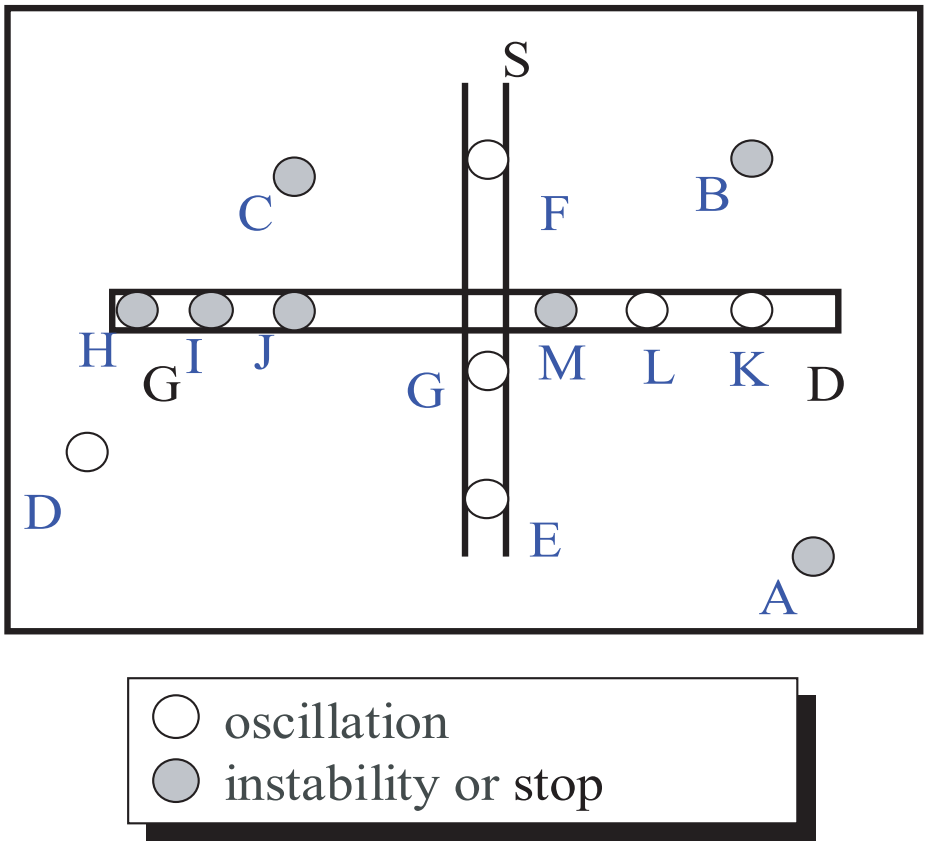

Figure 5.23: Measurement of oscillating condition

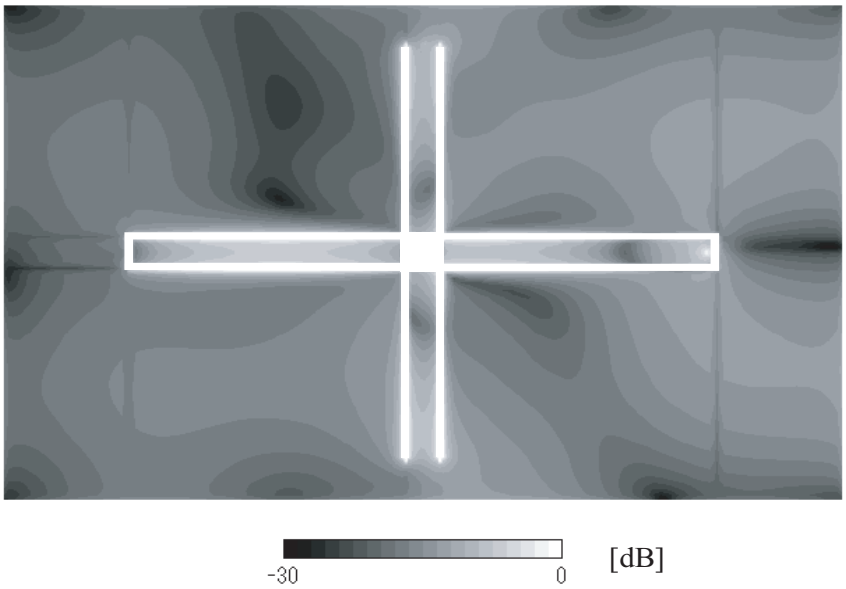

Figure 5.24: Current distribution of active antenna with oscillator

Figure 5.23 shows the measurement of the oscillating condition with various output ports. Figure 5.24 shows the current distribution of an analytic result. The location at which the oscillation is unstable or stops is the location at which the current is strongly or weakly distributed in the measurement. Figure 5.25 shows an active antenna with an oscillator and parasitic element. When this antenna is used as a self-oscillating mixer, the IF level increases upon arranging the parasitic element. Figure 5.26 shows the effect of the parasitic element on the radiation pattern. The radiation level of 5.4 dB in the $+z$ direction increases in comparison with the case wherein the parasitic element is not present. The IF output level increases as a result of the increase in the receiving levels of RF.

5.5 Summary

In this chapter, we investigated the FDTD analysis of an active integrated antenna. When adopting the incident method of measuring device voltage in the 8.5 GHz low

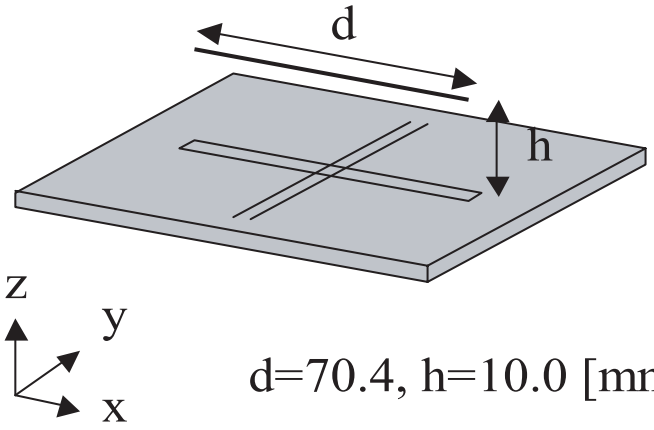

Figure 5.25: Active antenna with oscillator and parasitic element

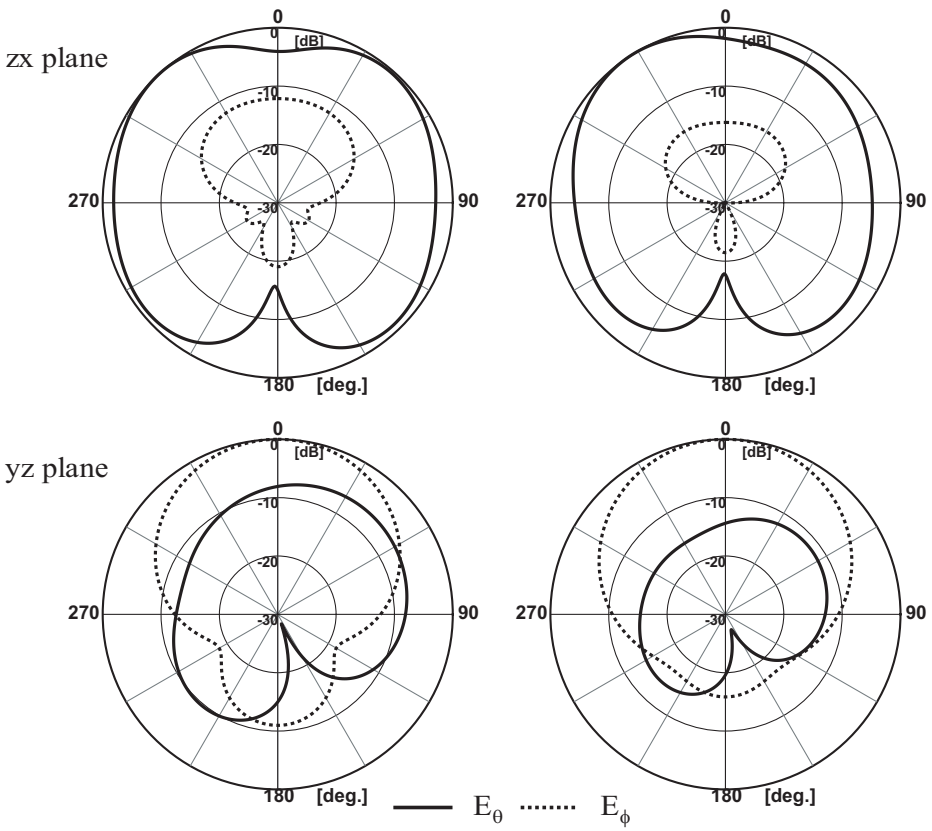

(a) without parasitic (b) with parasitic

Figure 5.26: Effect of parasitic element to radiation pattern

noise amplifier, the bias voltage converges on the setting voltage as a result of the modeling of all bias circuits and feeding a voltage through the short pin. We also compared the analytic and experimental results on the radiation pattern of an active patch antenna. The cross polarization levels increase due to the effect of the current which charges along the drain bias line, which is arranged in the neighborhood of the patch antenna. We examined the radiation pattern of an active slot antenna and showed that a cross polarization could be controlled by separating the radiation and circuit parts on the face and back of a substrate.

An oscillating condition of an active integrated antenna with an oscillator was examined in detail. The voltage source for a coplanar waveguide was proposed, and we compared the length of the gate and drain line and the oscillating frequency.

Chapter 6

Conclusion

The objective of this study was to propose a modeling for mobile communication antenna by FDTD method and its application. This dissertation discussed the following:

1. Modeling of an antenna and its immediate environment

2. Modeling of an equivalent circuit

Chapter 2 presented a modeling of the hybrid polarization diversity antenna with a side reflector. A highly accurate analysis is required to realize the coupling of -30 dB between each element for vertical and horizontal polarization. The HPBW of base stations, which is determined by the side reflector, is also designed for the various sectors. A basic technique (especially, with respect to achieving accuracy and reducing the calculation time) for FDTD analysis was discussed to examine the effect of the immediate environment of the antennas. The horizontal HPBWs of a dipole antenna and a holed patch antenna were optimized by modeling the side reflector. The mutual coupling of the hybrid antenna, which can be arranged in the same position, was analyzed and compared with the measurement.

Chapter 3 presented a mutual coupling between a transmitting and receiving antenna with a choke. The repeater system requires a coupling of -100 dB, and it is difficult to obtain its value through the measurement. The increase in the front-to-back (FB) or side ratio caused the suppression of mutual coupling in the case

of 4-element and 16-element arrays. Optimum choke parameters and SLL, achieved using binomial, Chebyshev and Taylor arrays, attained a mutual coupling of -100 dB. The validity of this structure was confirmed by the measurement.

Chapter 4 presented the modeling of a balun to feed a dual frequency antenna. The operating principle of a dual frequency antenna was proved with the modeling of the equivalent circuit of balun. The parameters of a series-connected open stub and a parallel-connected short were examined in detail. The stub length could help realize the multi-frequency operation.

Chapter 5 presented the modeling of a GaAsFET for an active integrated antenna. The modeling of the equivalent circuit of an active element was described in detail. The characteristics of the integrated antenna could be accurately computed using the modeling of a bias circuit and a finite ground plane. An active integrated antenna with an oscillator, which is used the self-oscillating mixer with electromagnetically-coupled antenna elements, was also examined. The voltage source, which is precisely modeled the actual structure for a coplanar waveguide, and an oscillating condition were presented.

Bibliography

[1] K. S. Yee, "Numerical solution of initial boundary value problems involving Maxwell's equations in isotropic media, "IEEE Trans. Antennas Propagat., vol. 14, no. 3, pp. 302-307, May 1966.

[2] A. Taflove and S. C. Hagness, "Computational Electrodynamics: The Finite-Difference Time-Domain Method, "Artech House, 2000.

[3] K. S. Kunz and R. J. Luebbers, "The Finite Difference Time Domain Method for Electromagnetics, "CRC Press, 1993.

[4] T. Uno, "Finite difference time domain method for electromagnetic field and antennas, "Corona Publishing Co., Ltd., 1998.

[5] http://www.micro.elec.okayama-u.ac.jp/~fujimori/FDTD/index.html

[6] T. Namiki, "A new FDTD algorithm based on alternating-direction implicit method, "IEEE Trans. Microwave Theory Tech., vol. 47, no. 10, pp. 2003-2007, Oct. 1999.

[7] F. Zheng, Z. Chen and J. Zhang, "A finite-difference time-domain Method without the Courant stability conditions, "IEEE Microwave Guided Wave Lett., vol. 9, no. 11, pp. 441-443, Nov. 1999.

[8] F. Zheng, Z. Chen and J. Zhang, "Toward the development of a three-dimensional unconditionally stable Finite-difference time-domain method, "IEEE Trans. Microwave Theory Tech., vol. 48, no. 9, pp. 1537-1543, Sept. 2000.

[9] T. Namiki, "3-D ADI-FDTD method-unconditionally stable time-domain algorithm for solving full vector Maxwell's equations, "IEEE Trans. Microwave Theory Tech., vol. 48, no. 10, pp. 1743-1748, Oct. 2000.

[10] T. Namiki and K. Ito, "Numerical simulation using ADI-FDTD method to estimate shielding effectiveness of thin conductive enclosures, "IEEE Trans. Microwave Theory Tech., vol. 49, no. 6, pp. 1060-1066, June 2001.

[11] T. Namiki and K. Ito, "Investigation of numerical errors of the two-dimensional ADI-FDTD method, "IEEE Trans. Microwave Theory Tech., vol. 48, no. 11, pp. 1950-1956, Nov. 2000.

[12] F. Zheng and Z. Chen, "Numerical dispersion analysis of the unconditionally stable 3-D ADI-FDTD method, "IEEE Trans. Microwave Theory Tech., vol. 49, no. 5, pp. 1006-1009, May 2001.

[13] W. Heinrich, K. Beilenhoff, P. Mezzanotte and L. Roselli, "Optimum mesh grading for finite-difference method, "IEEE Trans. Microwave Theory Tech., vol. 44, no. 9, pp. 1569-1574, Sept. 1996.

[14] Y. Wenhua and R. Mittra, "A technique for improving the accuracy of the nonuniform finite-difference time-domain algorithm, "IEEE Trans. Microwave Theory Tech., vol. 47, no. 3, pp. 353-356, March 1999.

[15] H. Jiang and H. Arai, "Analysis of computation error in antenna's simulation by using non-uniform mesh FDTD, "IEICE Trans. Commun., vol. E83-B, no. 7, pp. 1544-1553, July 2000.

[16] M. W. Chevalier, R. J. Luebbers and V. P. Cable, "FDTD local grid with material traverse, "IEEE Trans. Antennas Propagat., vol. 45, no. 3, pp. 411-421, March 1997.

[17] M. Okoniewski, E. Okoniewska and M. A. Stuchly, "Three-dimensional subgridding algorithm for FDTD, "IEEE Trans. Antennas Propagat., vol. 45, no. 3, pp. 422-429, March 1997.

[18] M. J. White, M. F. Iskander and Z. Huang, "Development of a multigrid FDTD code for three-dimensional applications, "IEEE Trans. Antennas Propagat., vol. 45, no. 10, pp. 1512-1517, Oct. 1997.

[19] K. R. Umashankar, A. Taflove and B. Beker, "Calculation and experimental validation of induced currents on coupled wires in an arbitrary shaped cavity, "IEEE Trans. Antennas Propagat., vol. 35, pp. 1248-1257, Nov. 1987.

[20] T. G. Jurgens, A. Taflove, K. Umashankar and T. G. Moore, "Finite-difference time-domain modeling of curved surfaces, "IEEE Trans. Antennas Propagat., vol. 40, no. 4, pp. 357-366, April 1992.

[21] J. J. Boonzaaier and C. W. I. Pistorius, "Thin wire dipoles–a finite-difference time-domain approach, "Electron. Lett., vol. 26, no. 22, pp. 1891-1892, Oct. 1990.

[22] R. Luebbers, L. Chen, T. Uno and S. Adachi, "FDTD calculation of radiation patterns, impedance, and gain for a monopole antenna on a conducting box, "IEEE Trans. Antennas Propagat., vol. 40, no. 12, pp. 1577-1583, Dec. 1992.

[23] T. Onishi, T. Kashiwa, Y. Naito and Y. Hosoya, "On the analysis of a patch antenna fed by coaxial cable using the FD-TD method, "IEICE Trans. Commun., vol. J80-B-II, no. 10, pp. 921-924, Oct. 1997.

[24] S-M Shum and K-M Luk, "FDTD analysis of probe-fed cylindrical dielectric resonator antenna, "IEEE Trans. Antennas Propagat., vol. 46, no. 3, pp. 325-333, March 1998.

[25] J. G. Maloney, K. L. Shlanger and G. S. Smith, "A simple FDTD model for transient excitation of antennas by transmission lines, "IEEE Trans. Antennas Propagat., vol. 42, no. 2, pp. 289-292, Feb. 1994.

[26] D. M. Sheen, S. M. Ali, M. D. Abouzahra and J. A. Kong, "Application of the three-dimensional finite-difference time-domain method to the analysis of planar

microstrip circuits, "IEEE Trans. Microwave Theory Tech., vol. 38, no. 7, pp. 849-857, July 1990.

[27] R. J. Luebbers and H. S. Langdon, "A simple feed model that reduces time steps needed for FDTD antenna and microstrip calculations, "IEEE Trans. Antennas Propagat., vol. 44, pp. 1000-1005, July 1996.

[28] K. Sawaya and Q. Chen, "Directivity of a monopole antenna on a finite ground plane, "IEICE Technical Report, AP97-54, pp. 9-12, June 1997.

[29] D. Yamamoto and H. Arai, "FDTD analysis of radiation pattern of antenna on truncated ground plane, "Proceedings of Asia Pacific Microwave Conference, Sydney, Australia, pp. 378-381, Dec. 2000.

[30] J. B. Schneider and K. L. Shlager, "FDTD simulations of TEM horns and the implications for staircased representations, "IEEE Trans. Antennas Propagat., vol. 45, no. 12, pp. 1830-1838, Dec. 1997.

[31] A. C. Cangellaris and D. B. Wright, "Analysis of the numerical error caused by the stair-stepped approximation of a conducting boundary in FDTD simulations of electromagnetic phenomena, "IEEE Trans. Antennas Propagat., vol. 39, no. 10, pp. 1518-1525, Oct. 1991.

[32] H. Arai and K. Cho, "Cellular and PHS base station antenna systems, "IEICE Trans. Commun. vol. E86-B, no. 3, pp. 980-992, March 2003.

[33] M. Nakano, T. Satoh and H. Arai, "Up-link polarization diversity and antenna gain measurement of hand-held terminal, "1995 IEEE AP-S Digest, pp. 1940-1943, June 1995.

[34] M. Nakano, S. Aizawa, T. Satoh, T. Matsuoka and H. Arai, "Up-link polarization diversity measurement for cellular communication systems using hand-held terminal, "1997 IEEE AP-S. Digest, pp. 1360-1363, June 1997.

[35] M. Nakano, T. Satoh and H. Arai, “Cellular base station polarization diversity measurement with human body effect at 900 MHz, ”IEICE Trans. Commun., vol. J83-B, no. 11, pp. 1554-1564, Nov. 2000.

[36] M. Nakano, S. Aizawa, T. Satoh, T. Matsuoka and H. Arai, “Small-sized polarization diversity antenna for cellular base stations, ”IEICE Society Conference, B-1-42, Sept. 1997.

[37] S. Moriyasu, T. Matsuoka, M. Nakano and H. Arai, “Printed dipole pair with modified parasitic elements and reflector, ”IEICE General Conference, B-1-150, March 1999.

[38] K. Fujimori, H. Arai and M. Furudate, “FDTD analysis for bent patch antenna with rooftop shaped ground plane, ”IEICE Technical Report, AP99-161, pp. 13-18, Jan. 2000.

[39] M. Shintaku and Y. Ebine, “Design of polarization diversity antenna at base station for cellular radio systems, ”IEICE Technical Report, AP98-29, pp. 43-50, July 1998.

[40] M. Shintaku and Y. Ebine, “A study of the polarization diversity antenna with 120° beam width on an experimental basis, ”IEICE Society Conference, B-1-108, Sept. 1998.

[41] Y. Sugimoto and Y. Ebine, “Design of a polarization diversity antenna of 60° beam-width in horizontal plane for cellular mobile radios, ”IEICE Technical Report, AP98-136, pp. 43-47, Jan. 1999.

[42] T. Shimura, M. Karikomi and Y. Ebine, “A 60 degrees beamwidth polarization diversity basestation antenna for 2 GHz band, ”IEICE Society Conference, B-1-95, Sept. 2000.

[43] T. Shimura, M. Karikomi and Y. Ebine, “An omni-directional polarization diversity array antenna using circular dipoles as horizontal polarization elements, ”IEICE Technical Report, AP99-260, March 2000.

[44] T. Shimura, M. Karikomi and Y. Ebine, "A 800/1500 MHz dual frequency bands and dual polarization antenna of 120 deg beamwidth for mobile base station, "IEICE General Conference, B-1-136, March 2001.

[45] T. Murayama, T. Koshio and N. Goto, "A hybrid antenna for new satellite EPIRB system, "IEICE General Conference, B-1-52, March 1997.

[46] Y. Udagawa, T. Murayama, T. Koshio and N. Goto, "A holed rectangular patch antenna, "IEICE General Conference, B-1-157, March 1998.

[47] Y. Rikuta, H. Arai and N. Goto, "Analysis of a holed rectangular patch antenna by using FDTD method "IEICE Society Conference, B-1-48, Sept. 1998.

[48] Y. Rikuta and H. Arai, "Self-diplexing antenna using patch antenna with a hole, "IEICE Trans. Commun., vol. J83-B, no. 8, pp. 1178-1185, Aug. 2000.

[49] S. Tsuda and M. Haneishi, "A construction of ring microstrip antennas, "IEICE Spring Conference, B-83, March 1992.

[50] N. Kuga and H. Arai, "A horizontal polarized wide-beam antenna with holed rectangular patch and monopole elements, "IEICE Technical Report, AP2000-78, pp. 25-29, Sept. 2000.

[51] Y. Ebine, "Dual frequency resonant base station antennas for PDC systems in Japan, "1999 IEEE AP-S Digest, pp. 564-567, June 1999.

[52] M. Kijima, Y. Ebine and Y. Yamada, "Development of a dual-frequency base station antenna for cellular mobile radio, "IEICE Trans. Commun., vol. E82-B, no. 4, 636-644, April 1999.

[53] Y. Yamada, Y. Ebine and M. Kijima, "Low sidelobe characteristics of a dual-frequency base station antenna in the case of electrical beam tilt use, "1999 IEEE AP-S Digest, vol. 4, pp. 2718-2721, June 1999.

[54] Y. Ebine, "Design of a dual-frequency base station antenna of 120° beam width in horizontal plane for cellular mobile radios, "IEICE Technical Report, AP97-73, pp. 17-24, July 1997.

[55] Y. Ebine, “A slender dual-frequency base station antenna for land mobile radios, ”IEICE Fall Conference, B-94, Sept. 1994.

[56] M. Karikomi, “Behaviors of parasitic elements on antenna bandwidth extension, ”IEICE Fall Conference, B-93, Sept. 1994.

[57] M. Karikomi and Y. Ebine, “Characteristics of printed dipole antenna with parasitic elements, ”IEICE Technical Report, AP89-2, 1989.

[58] M. Karikomi, “Effect of parasitic elements for the 0.9/1.5/2GHz corner reflector antenna with 120° beam width, ”IEICE Society Conference, B-1-80, Sept. 2002.

[59] T. Maruyama and K. Kagoshima, “Dual-frequency corner-reflector antennas fed by elements connected to parallel feed lines, ”IEICE Trans. Commun., vol. J77-B-II, no. 9, pp. 459-466, Sept. 1994.

[60] Y. Ebine, H. Tsunoda, K. Kosaka and N. Shimada, “Dual-frequency antennas with 60° beam-width by cross feeding dipole elements, ”IEICE General Conference, B-53, March 1995.

[61] M. Satoh, K. Mori and N. Shimada, “A corner-reflector antenna for dual-frequency use, ”IEICE Spring Conference, B-39, March 1989.

[62] Y. Ebine, “Impedance characteristics of a dual frequency corner reflector antenna with one side shorted metaric stabs, ”IEICE General Conference, B-1-59, March 1997.

[63] Y. Ebine, “Design of base station antennas for next generation cellular mobile radios(IMT-2000), ”IEICE Technical Report, AP2000-4, pp. 23-30, April 2000.

[64] K. Nakamura, K. Komada and Y. Ebine, “A triple-band antenna for mobile base stations, ”IEICE General Conference, B-1-66, March 2000.

[65] Y. Sugimoto and Y. Ebine, “A triple frequency base station antenna with 60° and 120° beam-width in horizontal plane for cellular mobile radios, ”IEICE Technical Report, AP99-47, pp. 35-42, July 1999.

[66] Y. Sugimoto and Y. Ebine, "An experimental study of a base station antenna with 60° and 120° beam-width in horizontal plane for cellular mobile radios, "IEICE Society Conference, B-1-75, Sept. 1999.

[67] Y. Ebine, Y. Sugimoto and M. Shintaku, "A base station antenna common used 0.8/1.5/2.0GHz bands for cellular mobile radios: 2GHz band offset beam antennas in horizontal plane, "IEICE Society Conference, B-1-76, Sept. 1999.

[68] H. Kakefuda, M. Karikomi and Y. Ebine, "A 0.8/1.5/2GHz base station antenna having dual 60 degrees beams for 2GHz band, "IEICE General Conference, B-1-65, March 2000.

[69] W. K. Roberts, "A new wide-band balun, "Proceedings of the IRE, vol. 45, pp. 1628-1631, Dec. 1957.

[70] R. Bawer and J. J. Wolfe, "A printed circuit balun for use with spiral antennas, "IRE Trans. Microwave Theory Tech., vol. MTT-8, pp. 319-325, May 1960.

[71] G. Oltman, "The compensated balun, "IEEE Trans. Microwave Theory Tech., vol. MTT-14, pp. 112-119, March 1966.

[72] B. Edward and D. Rees, "A broadband printed dipole with integrated balun, "Microwave Journal, pp. 339-344, May 1987.

[73] K. M. K. H. Leong, Y. Qian and T. Itoh, "Compact surface-wave assisted printed endfire antenna with multiples system compatibility, "2001 IEEE AP-S Digest, vol. 3, pp. 448-451, July 2001.

[74] G. S. Hilton and C. J. Railton, "Finite-difference time-domain analysis of a printed dipole antenna, "IEE 9th Int. Conf. Antennas Propagation, vol. 1, pp. 72-75, April 1995.

[75] K. Mori and H. Arai, "Study of active antenna receivers and calibration method for digital beamforming, "IEICE Trans. Commun., vol. J85-B, no. 9, pp. 1549-1557, Sept. 2002.

[76] C-N Kuo, B. Houshmand and T. Itoh, "Full-wave analysis of packaged microwave circuits with active and nonlinear devices: An FDTD approach, "IEEE Trans. Microwave Theory Tech., vol. 45, no. 5, pp. 819-826, May 1997.

[77] C-N Kuo, V. A. Thomas, S. T. Chew, B. Houshmand and T. Itoh, "Small signal analysis of active circuits using FDTD algorithm, "IEEE Trans. Microwave Theory Tech., vol. 5, no. 7, pp. 216-218, July 1995.

[78] C-N Kuo, R-B Wu, B. Houshmand and T. Itoh, "Modeling of microwave active devices using the FDTD analysis based on the voltage-source approach, "IEEE Microwave Guided Wave Lett., vol. 6, no. 5, pp. 199-201, May 1996.

[79] K-P Ma, M. Chen, B. Houshmand, Y. Qian and T. Itoh, "Global time-domain full-wave analysis of microwave circuits involving highly nonlinear phenomena and EMC effects, "IEEE Trans. Microwave Theory Tech., vol. 47, no. 6, pp. 859-866, June 1999.

[80] T. Uno and Y. Kanda, "Connection of black-box circuit and electromagnetic fields in FDTD computation, "IEICE Trans. Commun., vol. J81-B-2, no. 4, pp. 350-352, April 1998.

[81] A. Tsujimura, S. Sekine and H. Shoki, "A full-wave analysis of RF circuit by the FDTD method using scattering parameters, "IEICE Trans. Commun., vol. J85-B, no. 9, pp. 1526-1534, Sept. 2002.

[82] A. J. McCamant, G. D. McCormack and D. H. Smith, "An improved GaAs MESFET model for SPICE, "IEEE Trans. Microwave Theory Tech., vol. 38, no. 6, pp. 822-824, June 1990.

[83] H. Statz, P. Newman, I. W. Smith, R. A. Pucel and H. A. Haus, "GaAs FET device and circuit simulation in SPICE, "IEEE Trans. Electron Devices., vol. 34, pp. 160-169, Feb. 1987

[84] http://www.cel.com/pdf/datasheets/ne3210s1.pdf

[85] Y. Torimaru, K. Fujimori and S. Nogi, "FDTD analysis for low noise microwave amplifier using GaAsFET, "IEICE Technical Report, AP2002-127, pp. 49-54, Jan. 2003.

[86] K. Mori and H. Arai, "Active antenna using a parasitic element, "IEICE Trans. Commun., vol. J82-B, no. 9, pp. 1722-1729, Sept. 1999.

[87] K. D. Park, S. Sakurazawa and H. Arai, "Experimental study for optimizing self-oscillating mixer with electromagnetically coupled antenna element, "IEICE Trans. Commun., vol. J85-B, no. 9, pp. 1542-1548, Sept. 2002.

[88] H. Arai, "Base station antennas inside tunnels and subway stations, and outdoor compact base station antennas for PDC system in Japan, "1999 IEEE AP-S Digest, pp. 568-571, June 1999.

[89] Y. Fuke and Y. Ebine, "Optical transmission booster, "NTT DoCoMo Technical Journal, vol. 5, no. 1, pp. 29-32, April 1997.

[90] Y. Fuke, J. Suganuma and Y. Ebine, "Fiber-optic transmission of underground area for cellular mobile radio systems, "IEICE General Conference, B-563, March 1996.

[91] H. Arai and N. Goto, "Flat antennas for indoor cellular system, "1994 IEEE AP-S Digest, pp. 344-347, June 1994.

[92] H. Jiang and H. Arai, "FDTD analysis of low profile top loaded monopole antenna, "IEICE Trans. Commun., vol. E85-B, no. 11, pp. 2468-2475, Nov. 2002.

[93] K. Itoh, M. Shintaku and Y. Ebine, "Loop canceling booster including adaptive canceling function of interference waves, "NTT DoCoMo Technical Journal, vol. 5, no. 1, pp. 24-28, April 1997.

[94] H. Suzuki and Y. Ebine, "Configuration and performance of an open air booster for radio pager systems, "IEICE General Conference, B-428, March 1996.

[95] K. Itoh and Y. Ebine, “Auto gain adjustment booster for W-CDMA, ”IEICE General Conference, B-5-82, March 2000.

[96] K. Itoh and Y. Ebine, “Performance of a loop canceling booster for radio pager system, ”IEICE Society Conference, B-5-158, Sept. 1997.

[97] K. Itoh and Y. Ebine, “Field performance of a loop canceling booster for radio pager system, ”IEICE Society Conference, B-5-42, Sept. 1998.

[98] K. Itoh and Y. Ebine, “Influence on delay path of a loop canceling booster for radio pager system, ”IEICE General Conference, B-5-53, March 1999.

[99] T. Maeyama, T. Inoue, K. Kamimura and S. Yamato, “Development of CDMA repeater with echo canceller, ”IEICE Technical Report, AP2001-258, pp. 65-70, March 2002.

[100] M. Yamazaki and Y. Ebine, “Frequency converting repeater, ”NTT DoCoMo Technical Journal, vol. 5, no. 1, pp. 19-23, April 1997.

[101] M. Yamazaki, M. Nakada and Y. Ebine, “Characteristics of diversity reception for a repeater used frequency converter, ”IEICE General Conference, B-393, March 1995.

[102] M. Yamazaki and Y. Ebine, “A repeater used frequency converter for mobile communication systems, ”IEICE General Conference, B-5-147, March 1997.

[103] M. Yamazaki, Y. Ebine and H. Ohdate, “Frequency offset booster, ”NTT DoCoMo Technical Journal, vol. 5, no. 1, pp. 15-18, April 1997.

[104] Y. Rikuta, H. Arai and Y.Ebine, “Mutual coupling suppression of two dipole antennas backed by optimized reflector, ”2002 IEEE AP-S Digest, vol. 2, pp. 276-279, June 2002.

[105] M. Shintaku and Y. Ebine, “Improvement of coupling between antennas for mobile communication, ”IEICE Society Conference, B-74, Sept. 1996.

[106] M. Shintaku and Y. Ebine, “Study of coupling between antennas attached to a metal cylinder, ”IEICE General Conference, B-1-58, March 1997.

[107] M. Shintaku and Y. Ebine, “A study of decreasing in mutual coupling between antennas using for booster systems for mobile telecommunication systems, ”IEICE Society Conference, B-1-47, Sept. 1997.

[108] T. Nara, T. Hori and N. Nakajima, “Choke loaded low sidelobe microstrip broad side array antenna, ”IECE Technical Report, AP83-4, pp. 19-24, April 1983.

Publication List

Following lists contain the related publications of this dissertation.

Papers

1. Naobumi Michishita and Hiroyuki Arai, "A Polarization Diversity Antenna by Printed Dipole and Patch with a Hole, "IEICE Trans. Commun., vol. J85-B, no. 3, pp. 391-399, March 2002 (in Japanese).

2. Naobumi Michishita, Hiroyuki Arai, Koichi Tsunekawa and Masahiro Karikomi, "FDTD Analysis of Dual Frequency Printed Dipole Antenna, "IEICE Trans. Commun., vol. J86-B, no. 1, pp. 68-75, Jan. 2003 (in Japanese).

3. Naobumi Michishita and Hiroyuki Arai, "FDTD Analysis of Active Integrated Antenna with Amplifier, "IEICE Trans. Commun., vol. J86-B, no. 9, pp. 1766-1773, Sept. 2003 (in Japanese).

4. Naobumi Michishita, Hiroyuki Arai and Yasuko Kimura, "Mutual Coupling Characteristics of Choke Loaded Patch Array Antenna, "IEICE Trans. Commun. (submitted in 2004).

International Conferences

1. Naobumi Michishita, Hiroyuki Arai, Masayuki Nakano, Toshio Satoh and Tohru Matsuoka, "FDTD Analysis for Printed Dipole Antenna with Balun," 2000 Asia-Pacific Microwave Conference, pp. 739-742, Sydney, Australia, Dec. 2000.

2. Naobumi Michishita and Hiroyuki Arai, "FDTD Analysis of Printed Monopole Antenna," IEE Eleventh International Conference on Antennas and Propagation, vol.2, pp. 728-731, Manchester, UK, April 2001.

3. Naobumi Michishita and Hiroyuki Arai, "A Polarization Diversity Antenna by Printed Dipole and Patch with a Hole," 2001 IEEE Antennas and Propagation Society International Symposium, pp. 368-371, Boston, MA, July 2001.

4. Naobumi Michishita, Hiroyuki Arai, Koichi Tsunekawa and Masahiro Karikomi, "FDTD Analysis of Dual Frequency Printed Dipole Antenna," 2002 IEEE Antennas and Propagation Society International Symposium, vol. 2, pp. 40-43, San Antonio, TX, Jun. 2002.

5. Naobumi Michishita, Hiroyuki Arai and Yoshio Ebine, "Mutual Coupling Characteristics of Patch Antennas with Choke for Repeater Systems," IEE Twelfth International Conference on Antennas and Propagation, vol. 1, pp. 229-232, Exeter, UK, April 2003.

6. Naobumi Michishita and Hiroyuki Arai, "FDTD Analysis of an Active Integrated Antenna with Amplifier," The 5th International Workshop on Computational Electromagnetics in Time Domain, pp. 77-81, Halifax, Canada, June 2003.

7. Naobumi Michishita, Hiroyuki Arai and Yoshio Ebine, "Mutual Coupling Characteristics of Binomial and Chebyshev Arrays using 16 Element Patch Antennas with Choke for Repeater Systems," 2003 IEEE Antennas and Propagation Society International Symposium, vol. 1, pp. 585-588, Columbus, OH, June 2003.

IEICE General Conferences and Society Conferences

1. Naobumi Michishita, Kazuhiro Fujimori and Hiroyuki Arai, "FDTD Analysis for Transient Excitation of Monopole Antennas on Finite Plane, "General Conference, B-1-104, Keio University, Yokohama, March 1999.

2. Naobumi Michishita and Hiroyuki Arai, "FDTD Analysis for Printed Dipole Antenna, "Society Conference, B-1-36, Nihon University, Funabashi, Sept. 1999.

3. Naobumi Michishita, Hiroyuki Arai, Masayuki Nakano, Toshio Satoh, Tohru Matsuoka, "FDTD Analysis for Printed Dipole Antenna with Balun, "General Conference, B-1-48, Hirosima University, Higashi Hiroshima, March 2000.

4. Naobumi Michishita and Hiroyuki Arai, "Built-in Balun Printed Dipole Antenna with Parasitic Elements, "Society Conference, B-1-148, Nagoya Institute of Technology, Nagoya, Sept. 2000.

5. Naobumi Michishita and Hiroyuki Arai, "A Polarization Diverstity Antenna by Printed Dipole and Patch with a Hole, "General Conference, B-1-133, Ritsumeikan University, Kusatsu, March 2001.

6. Naobumi Michishita and Hiroyuki Arai, "The Mutual Coupling in Polarization Diversity Antenna by Printed Dipole and Patch Antenna with a Hole, "Society Conference, B-1-61, The University of Electro-Communications, Chofu, Sept. 2001.

7. Naobumi Michishita, Hiroyuki Arai and Yoshio Ebine, "The Relay Station by Circular Patch Array for Mobile Communication, "General Conference, B-1-180, Waseda University, Shinjuku, March 2002.

8. Naobumi Michishita, Hiroyuki Arai and Yoshio Ebine, "Mutual Coupling Characteristics of Beam Tilted Array Antenna for Repeater, "Society Conference, B-1-90, Miyazaki University, Miyazaki, Sept. 2002.

9. Naobumi Michishita, Hiroyuki Arai and Yoshio Ebine, "Mutual Coupling Characteristics of 16 Elements Patch Array Antenna for Repeater, "General Conference, B-1-78, Tohoku University, Sendai, March 2003.

10. Naobumi Michishita and Hiroyuki Arai, "FDTD Analysis of Active Antenna with Oscillator, "Society Conference, B-1-134, Niigata University, Niigata, Sept. 2003.

IEICE Technical Reports

1. Naobumi Michishita and Hiroyuki Arai, "FDTD Analysis for Monopole and Patch Antenna on Finite Ground Plane, "IEICE Technical Report, AP99-13, pp. 23-28, Tohoku University, Sendai, May 1999.

2. Naobumi Michishita and Hiroyuki Arai, "FDTD Analysis for Monopole Antenna on Finite Ground Plane, "IEICE Technical Report, AP99-112, pp. 45-50, Toyota Central R&D Labs., Inc., Nagakute, Oct. 1999.

3. Naobumi Michishita and Hiroyuki Arai, Koichi Tsunekawa, Masahiro Karikomi, "FDTD Analysis of Dual Frequency Antenna, "IEICE Technical Report, AP2001-187, pp. 63-70, Yamaguchi University, Ube, Jan. 2002.

4. Naobumi Michishita, Kazuyuki Ochia and Hiroyuki Arai, "The Analysis for the Patch Antenna in Consideration of the Coaxial Connector and the Microstrip Line, "IEICE Technical Report, AP2002-12, pp. 7-12, Denkoku no MoriI, Yonezawa, May 2002.

5. Naobumi Michishita and Hiroyuki Arai, "FDTD Analysis of Active Integrated Antenna with Amplifier, "IEICE Technical Report, AP2002-128, pp. 55-60, Kumamoto University, Kumamoto, Jan. 2003.

6. Yuji Yokoo, Naobumi Michishita and Hiroyuki Arai, "FDTD Analysis of Planar Inverted-F Antenna Using CP Method, "IEICE Technical Report, AP2003-12, pp. 69-72, Osaka University, Suita, April 2003.